
Doctoral Dissertations

Student Theses and Dissertations

Spring 2022

Scale formation, properties and de-scaling in steelmaking

Richard Osei

Follow this and additional works at: https://scholarsmine.mst.edu/doctoral_dissertations



Part of the [Metallurgy Commons](#)

Department: **Materials Science and Engineering**

Recommended Citation

Osei, Richard, "Scale formation, properties and de-scaling in steelmaking" (2022). *Doctoral Dissertations*. 3157.

https://scholarsmine.mst.edu/doctoral_dissertations/3157

This thesis is brought to you by Scholars' Mine, a service of the Missouri S&T Library and Learning Resources. This work is protected by U. S. Copyright Law. Unauthorized use including reproduction for redistribution requires the permission of the copyright holder. For more information, please contact scholarsmine@mst.edu.

SCALE FORMATION, PROPERTIES AND DE-SCALING IN STEELMAKING

by

RICHARD OSEI

A DISSERTATION

Presented to the Graduate Faculty of the

MISSOURI UNIVERSITY OF SCIENCE AND TECHNOLOGY

In Partial Fulfillment of the Requirements for the Degree

DOCTOR OF PHILOSOPHY

in

MATERIALS SCIENCE AND ENGINEERING

2022

Approved by:

Dr. Ronald O'Malley, Advisor

Dr. Simon Lekakh

Dr. Laura Bartlett

Dr. Scott Miller

Dr. Obinna Adaba

© 2022

Richard Osei

All Rights Reserved

PUBLICATION DISSERTATION OPTION

This dissertation consists of the following six articles, formatted in the style used by the Missouri University of Science and Technology:

Paper I, pages 14–35, has been published in AISTech Conference Proceedings 2020.

Paper II, pages 36–74, has been published in Metallurgical Transactions B (Met Trans. B)

Paper III, pages 75–102, has been published in Metallurgical Transactions B (Met Trans. B)

Paper IV, pages 103–125, has been published by Association of Iron and Steel Technology (AISTech) 2021.

Paper V: pages 126–156 has been submitted to Oxidation of Metals (Oxide Met.)

Paper VI: pages 157-175 has been submitted to AISTech Conference Proceedings, 2022

ABSTRACT

During continuous castings, reheating, and hot rolling, slab surfaces are exposed to atmospheres containing oxidizing gases which results in scale formation.

Inefficient removal of the formed scale during reheating affects product surface quality. The effect of steel composition and operating parameters on scale formation and scale removal efficiencies were investigated. Experimental investigations were carried out using a thermogravimetric (TGA) apparatus designed to replicate the combustion gas atmosphere and temperature in actual industrial slab reheat furnaces. Report on oxidation kinetics, scale structure and properties, and descaling were conducted on laboratory cast and industrial samples. Different characterization techniques were used to analyze in-depth formed scale structure

Results on scale formation studies showed that sample chemistry, reheating parameters and sample surface condition significantly affected the development of scale structure and its properties particularly in the subsurface scale layer region. The studies showed that major alloying elements (Mn, Si), micro alloying (Al) elements, and impurities (Cu, Ni, Cr) modified the properties of the formed scale and its kinetics mechanism. Complexity of scale formation due to alloying elements and impurities in steel and cast slab surface condition affected its efficient removal using hydraulic descaling. Samples with high alloying elements of *Si* and *Mn* were characterized by strong adhesion and complex root penetrations in the subsurface scale region which decreased descaling efficiency. Descaling hydraulic parameters and surface pretreatment that improved scale removal efficiency were suggested.

ACKNOWLEDGMENTS

I would like to show my gratitude to my advisers, Dr. Ronald J. O'Malley, and Dr. Simon N. Lekakh for their professional mentorship, guidance, support, and directions throughout this 4-year PhD journey.

I would also like to thank my dissertation committee members consisting of Dr. Laura Bartlett, Dr. Scott Miller, and Dr. Obinna Adaba for their time and input.

I would also want to thank the Peaslee Steel Manufacturing Research Center (PSMRC) industrial member companies for funding this project and their technical support for this work.

I appreciate the help received from professors, graduate and undergraduate researchers and staff of the Materials Science and Engineering Department. Special thanks to Denise, Teneke, Brian, Nathan, and Dr. Mario Buchely.

Thanks to Dr. Grace Ofori-Saropong of University of Mines and Technology, Tarkwa Ghana (UMaT) who has been a role model

Dami, Madhuri, Dr. Soumava, Dr. Bose, Dr. Kansake, Dr. Abbey, Abdul, Alice, Asebi and the numerous friend I cannot mention. You have been like family to me, thank you for the friendship and love.

Finally, I would like to thank my family in Ghana, my mom, Ken, Nana, Shirley, Oforiwaa and Agyapomah for their unconditional love for me. This journey would have not been possible without their support. Finally, I God thank for seeing me through this journey. My life has been inspired by the many songs from Bob Marley (One Love!)

TABLE OF CONTENTS

	Page
PUBLICATION DISSERTATION OPTION	iii
ABSTRACT.....	iv
ACKNOWLEDGMENTS	v
LIST OF ILLUSTRATIONS.....	xi
LIST OF TABLES.....	xvii
 SECTION	
1. INTRODUCTION.....	1
1.1. BACKGROUND INFORMATION	1
1.2. SCALE GROWTH MECHANISM.....	5
1.3. SCALE REMOVAL.....	9
1.4. RESEARCH OBJECTIVES.....	12
 PAPER	
I. SCALE FORMATION ON 430 STAINLESS STEEL IN A SIMULATED SLAB COMBUSTION REHEAT FURNACE ATMOSPHERE	14
ABSTRACT.....	14
1. INTRODUCTION.....	15
2. EXPERIMENTAL PROCEDURE.....	16
3. RESULTS.....	20
3.1. INDUSTRIAL SCALE EVOLUTION FROM AS-CAST TO HOT ROLLED CONDITIONS.....	20
3.2. OXIDATION KINETICS IN SIMULATED REHEATING FURNACE.....	22

4. DISCUSSION	24
4.1. EFFECT OF SURFACE CONDITIONS: AS-CAST VS. GROUND	24
4.2. EFFECT OF COMBUSTION ATMOSPHERE.....	28
4.3. EFFECT OF AL.....	30
5. CONCLUSION	32
ACKNOWLEDGEMENTS	33
REFERENCES.....	33
II. EFFECT OF AL ADDITIONS ON SCALE STRUCTURE AND OXIDATION KINETICS OF 430-FERRITIC STAINLESS STEEL REHEATED IN A COMBUSTION ATMOSPHERE.....	36
ABSTRACT.....	36
1. INTRODUCTION.....	37
2. PROCEDURES	41
2.1. STEELS AND OXIDATION PARAMETERS.....	41
2.2. CHARACTERIZATION	43
2.3. THERMODYNAMIC SIMULATION.....	44
3. RESULTS.....	45
3.1. EXPERIMENTAL OXIDATION KINETICS	45
3.2. EFFECT OF STEEL CHEMISTRY ON SCALE STRUCTURE	46
3.3. TRANSMISSION ELECTRON MICROSCOPY (TEM) OF SUBSURFACE SCALE STRUCTURE.....	49
4. DISCUSSION	56
4.1. THERMODYNAMIC ASSESSMENT ON THE EFFECT OF AL ALLOYING OF 430 STAINLESS STEEL ON SCALE STRUCTURE.....	56
4.2. MIXED CONTROL OXIDATION KINETICS MODELLING	58

4.3. EFFECT OF TEMPERATURE ON SCALE STRUCTURE TRANSFORMATION	60
4.4. EFFECT OF AL ALLOYING ON SUBSURFACE SCALE STRUCTURE.....	64
5. CONCLUSION	68
ACKNOWLEDGEMENTS	69
SUPPLEMENTARY MATERIAL.....	70
REFERENCES	71
III. THERMODYNAMIC PREDICTION AND EXPERIMENTAL VERIFICATION OF MULTI-PHASE COMPOSITION OF SCALE FORMED ON REHEATED ALLOY STEELS.....	75
ABSTRACT	75
1. INTRODUCTION.....	76
2. PROCEDURES	79
2.1. STEELS AND OXIDATION	79
2.2. THERMODYNAMIC SIMULATION.....	81
3. RESULTS.....	82
3.1. CARBON STEEL.....	82
3.2. ADVANCED HIGH STRENGTH STEELS (AHSS).....	86
3.3. FERRITIC STAINLESS STEEL.....	88
3.4. AUSTENITIC STEELS.....	92
4. DISCUSSION	94
5. CONCLUSION	98
ACKNOWLEDGEMENTS	99
REFERENCES.....	99

IV. DESCALING OF MEDIUM <i>C</i> AND HIGH <i>SI</i> , <i>MN</i> STEELS	103
ABSTRACT	103
1. INTRODUCTION	103
2. EXPERIMENTAL PROCEDURES	106
3. RESULTS	110
3.1. SCALE FORMED DURING REHEATING	110
3.2. CLASSIFICATION OF DESCALED SURFACE QUALITY	114
3.3. DESCALING EFFICIENCY	114
4. DISCUSSION	121
5. CONCLUSIONS	123
ACKNOWLEDGEMENTS	124
REFERENCES	124
V. EFFECT OF <i>CU</i> ADDITIONS ON SCALE STRUCTURE AND DESCALING EFFICIENCY OF LOW <i>C</i> STEEL REHEATED IN A COMBUSTION GAS ATMOSPHERE	126
ABSTRACT	126
1. INTRODUCTION	127
2. EXPERIMENTAL	130
3. RESULTS AND DISCUSSION	134
3.1. CHARACTERIZATION OF SCALE FORMED DURING REHEATING .	134
3.2. DESCALING EFFICIENCY	143
3.3. COMPARISON OF DESCALING EFFICIENCY IN THE DIFFERENT <i>CU</i> STEELS	149
4. CONCLUSIONS	152

ACKNOWLEDGEMENTS	153
REFERENCES.....	153
VI. EFFECT OF MOLD POWDER RESIDUE ON THIN CAST SLAB SCALE STRUCTURE EVOLUTION DURING REHEATING AND DESCALING.....	157
ABSTRACT	157
1. INTRODUCTION.....	157
2. EXPERIMENTAL PROCEDURES	159
3. RESULTS.....	163
3.1. SCALE FORMED ON AS-CAST SLAB SURFACE	163
3.2. SCALE AFTER REHEATING	165
4. DESCALING EFFICIENCY AND DISCUSSION	169
5. CONCLUSIONS	173
ACKNOWLEDGEMENTS	175
REFERENCES	175
SECTION	
2. CONCLUSIONS AND RECOMMENDATIONS.....	176
2.1. CONCLUSIONS	176
2.2. RECOMMENDATIONS.....	179
BIBLIOGRAPHY	181
VITA.....	185

LIST OF ILLUSTRATIONS

SECTION	Page
Figure 1.1 Effect of water vapor on scale structure, a) oxidation in moist atmosphere and b) oxidation in dry atmosphere [1].....	2
Figure 1.2. Scale structure (a) Mixed [2] and (b) layered structure of scale (Fe ₂ O ₃ - external, Fe ₃ O ₄ intermediate and FeO - inner) [3].	3
Figure 1.3. Effect of temperature on scale composition [18].	3
Figure 1.4. Oxide behaviour under deformation, (a) Load vs displacement of different oxides [3] and (b) scale behavior during hot rolling [4].	4
Figure 1.5. Complexity of oxidation, (a) An overview of the surface and sub-surface processes occurring during reheating and (b) processes have place during oxidation of alloyed steels [1].	4
Figure 1.6. Schematic representation of scale growth: a) oxidation controlled by mass transfer in gas phase and b) oxidation controlled by mass transfer through the scale: parabolic or complex oxidation [35].....	5
Figure 1.7. Linear oxidation growth kinetics at different temperatures [37].....	6
Figure 1.8. Parabolic growth kinetics at different air-fuel ratio (%) [37].....	7
Figure 1.9. Dependence of scale formation rate on combustion gas composition [35].....	9
Figure 1.10. Scale Removal, (a) Schematic of hydraulic descaling [30], (b) Effect of hydraulic parameter on descaling (velocity and impact factor) [37]	10
Figure 1.11. Scale defects, (a) Fluid fayalite-wustite eutectic formed at 12000C (0.8C-1.2Si) [35]; (b) Types of mill scale defects [47].....	11
PAPER I	
Figure 1. TGA experimental setup.....	19
Figure 2. Industrial oxide scale structure of 430 stainless steel as-cast slab: Left: BSE image with outlined layers in scale and Right: EDX analysis chemistry of oxide layers.	21

Figure 3. Raman spectroscopy of 430 stainless steel industrial as-cast scale structure, indicating oxide phases present in the various scale layers.	21
Figure 4. BSE image of scale structure with EDX analysis of industrial scale on transfer bar (reheated, hot rolled, and descaled).	22
Figure 5. Oxidation kinetics of low Al 430 stainless steel (as-cast slabs) measured by TGA isothermal heating: (a) as-cast (condition 1b) vs. pre-machined (condition 1c) surface condition in combustion gas with 3% oxygen and (b) effect of oxygen in combustion atmosphere for ground surface condition (conditions 1c (3% O ₂) and 1d (5% O ₂) from Table 2.....	23
Figure 6. Oxidation rate of 430 stainless steel with different Al in transfer bars (conditions 2b vs 2c, Table 2).	24
Figure 7. Surface structure of low Al 430 stainless steel sample (condition 1c, Table 2).	25
Figure 8. Scale (condition 1c, Table 2) in cross section showing the multi-layer oxide structure.	26
Figure 9. Raman spectroscopy of oxide phases in specimen 1c from Table 2.	26
Figure 10. Scale (condition 1a and 1b, Table 2) in cross section, showing different multi-layer oxide structure in as-cast condition and after re-heating.....	27
Figure 11. Subsurface structure of re-heated low Al steel as-cast steel with as-cast vs surface ground (conditions 1b vs 1c, Table 2)	28
Figure 12. Oxide scale structure of as cast low Al 430 steel oxidized in a combustion gas atmosphere with 3% and 5% oxygen at 1150°C (condition 1c and 1d, Table 2).	29
Figure 13. Oxide scale structure of low and high Al 430 steel oxidized in a combustion atmosphere with 3% oxygen at 1150°C (condition 2b and 52c, Table 2).	30
Figure 14. Thermodynamic simulation (FactSage software) of the sequence of formation of different phases in multi- layered oxide formed in high-Al 430 stainless steel grade.	31

PAPER II

Figure 1. Oxidation kinetics of 430 stainless steel measured by TGA isothermal heating: (left) 1050°C - 1150°C and (right) 1200°C – 1250°C.	46
--	----

Figure 2. Cross-sectional BSE image of scale structure in 430 ferritic steels at 1150°C: left base (a-low magnification) and (b-high magnification) and right Al alloyed (c-low magnification) and (d-high magnification) steels Number indicated formed scale layers: 1 – outer, 2 – intermediate, 3 – inner, and 4 – sublayer joined with metal matrix.....	50
Figure 3. Subsurface location of FIB/TEM extracted specimen (base steel).	51
Figure 4. TEM cross-sectional structure of subsurface oxide scale with multiple oxide zones indicated by red dashed box (a), oxide zone with ring-like structure having different phases (b), elemental map showing distribution of elements in the oxide zone (c), and selected area electron diffraction (SAED) patterns (d).	53
Figure 5. TEM Cross-sectional image of subsurface oxide scale in Al micro-alloyed steel with two zones (a), oxide zone with ring-like structure (b), oxide zone with rod-like structure (c) with elemental map of oxides (d) and phase identification using selected electron diffraction pattern (e).	55
Figure 6. Thermodynamic prediction of stable oxide phases formed during oxidation 430-ferritic stainless steel at different oxygen partial pressures at 1150°C: (a) base and (b) Al alloyed 430 ferritic steels.	57
Figure 7. Oxidation kinetic of base and Al micro-alloyed 430 stainless steels: dashed (modelled) results) and continuous (experimental) curves at 1150oC.....	59
Figure 8. Dependence of rate constant on temperature for oxidation assuming a mixed controll kinetics: (a) base and (b) Al alloyed 430 stainless steels.....	60
Figure 9. Cross-sectional SEM BSE image of scale structure transformation in base 430 ferritic stainless steel at different telepictures during oxidation in combustion gas atmosphere for 2 hours.....	62
Figure 10. Sudden change in oxidation rate resulted scale cracking and spalling at high temperature (base steel, 1200°C).....	63
Figure 11. Temperature dependence of scale growth for base and Al alloyed ferritic steels.....	64
Figure 12. Scanning Transmission Electron Microscopy (STEM) image of cross-sectional subsurface scale structure, a) base steel and b) Al alloyed steel.....	66
Figure 13. Equilibrium of BCC/FCC transformation in Fe-Cr system at 1150°C considering effect of other alloying elements in 430 steel (FACTSAGE software).....	67

Figure 14. Schematic representation of oxidation processes during reheating base and Al microalloyed 430 ferritic steels.	67
--	----

PAPER III

Figure 1. Low (left) and high (right) magnifications BSE image of cross-sectional scale structure in carbon steels: 1a (a) and 1b (b). Number indicated formed layers: 1 – outer, 2 – intermediate, 3 – inner, and 4 – sublayer joined with metal matrix.	84
Figure 2. Thermodynamic prediction of oxide phases formed during reheating carbon steel at different oxygen/steel mass ratio: a) carbon steel 1a with low Mn and Si and elevated Cr and b) carbon steel 1b with elevated Si and Mn and low Cr.....	85
Figure 3. Low (left) and high (right) magnifications BSE image of cross-sectional scale structure in advanced high strength steels: 2a (a) and 2b (b). Number indicated formed layers: 1 – outer, 2 – intermediate, 3 – inner, and 4 – sublayer joined with metal matrix.	87
Figure 4. Thermodynamic prediction of oxide phases present during reheating AHSS at different oxygen/steel mass ratio: left) steel 2a with medium Mn and Si, and right) steel 2b with high Mn and Si.....	88
Figure 5. Low (left) and high (right) magnifications BSE image of cross-sectional scale structure in ferritic steels 3a (a), 3b (b), and 3c (c). Number indicated formed layers: 1 – outer, 2 – intermediate, 3 – inner, and 4 – sublayer joined with metal matrix.	90
Figure 6. Thermodynamic prediction of oxide phases present during reheating studied ferritic steels at different oxygen/steel mass ratio: a) steel 3a with low Al, b) steel 3b with high Al, and c) steel 3c with Ti.	92
Figure 7. Low (left) and high (right) magnifications BSE image of cross-sectional scale structure in austenitic steel (4). Number indicated formed layers: 1 – outer, 2 – intermediate, 3 – inner, and 4 – sublayer joined with metal matrix	93
Figure 8. Thermodynamic prediction of oxide phases present during reheating austenitic steel 4 with high Ni and Cr at different oxygen/steel mass ratio.....	94

PAPER IV

Figure 1. Induction furnace reheating in control atmosphere setup.....	109
--	-----

Figure 2. Descaling setup using a CNC stage.....	109
Figure 3. Cross-sectional BSE image and chemistry of scale structures present in steels reheated at 1200C before descaling.	113
Figure 4. Descaled surface classification.....	114
Figure 5. Surface quality of base steel after descaling at different <i>IF</i>	116
Figure 6. Surface quality of medium <i>C</i> steel after descaling at different <i>IF</i>	117
Figure 7. Surface quality of high <i>Si</i> steel after descaling at different <i>IF</i>	119
Figure 8. Surface quality of High <i>Mn</i> steel after descaling at different <i>IF</i>	120
Figure 9. Effect of <i>IF</i> on descaling efficiency of: (a) base, (b) medium <i>C</i> , (c) high <i>Si</i> , and (d) high <i>Mn</i> steels.....	122
Figure 10. Effect of <i>IF</i> on residual scale thickness after descaling for the different steel grades.	122

PAPER V

Figure 1. Induction furnace reheating steel slab in control atmosphere.	132
Figure 2. Descaling setup using a CNC stage: (a) CNC stage with jet nozzle, (b) variation in impact factor, and (c) footprint of descaled slab.....	133
Figure 3. Cross-sectional BSE image of scale structure for low <i>Cu</i> steel: top-left (low magnification), top-right (medium magnification), bottom-left (high-magnification), and bottom-right (EDX elemental map).	136
Figure 4. Phases identified in scale using Raman spectroscopy: (a) phases in external outer layer, (b) phases in external mid-scale layer, and phases in complex subsurface layer: (c) in point #4, Figure 3, and (d) in point #5, Figure 3.	137
Figure 5. Cross-sectional BSE image of scale structure for medium <i>Cu</i> steel: top-left (low magnification), top-right (medium magnification). Bottom-left and right (high-magnifications) illustrated bonded to the matrix second oxide structure.	141
Figure 6. Cross-sectional BSE image of scale structure for high <i>Cu</i> steel: top-left (low magnification), top-right (medium magnification), bottom-left (high-magnification), and bottom-right (elemental map).	142

Figure 7. Descaled surface quality classification.....	143
Figure 8. Quantified surface quality of low Cu steel after descaling at different IF.	145
Figure 9. Quantified surface quality of medium Cu steel after descaling at different IF	147
Figure 10. Quantified surface quality of high Cu steel after descaling at different <i>IF</i> ...	148
Figure 11. Effect of IF and Cu in steel chemistry on descaling efficiency.....	151
Figure 12. Schematic representation of reheated scale structure of different Cu additions and its structural change during descaling at different impact factors.....	151

PAPER VI

Figure 1. Reheating and descaling setup: (a) sample condition, (b) induction furnace, (c) CNC stage with jet nozzle, (d) footprint of descaled slab, (e) sample from water jet extraction, and (f) hot charge reheating schedule.....	162
Figure 2. BSE images (top) and EDX elemental maps (bottom) of cross-section of scale structure formed on as-cast surface: top left section with mold powder inclusions, and top right section with mixed oxide/mold powder.	165
Figure 3. BSE images (top) and EDX elemental maps (bottom) of scale structure formed on pre-machined surface during reheating.	168
Figure 4. Cross-section BSE of scale structure formed on as-cast surface after reheating: top (low magnification), and bottom (high magnification).....	169
Figure 5. Effect of surface condition on descaling efficiency.	170
Figure 6. Cross-section BSE of residual scale structure after descaling: top-left (pre-machined surface), top-right (as-cast surface), bottom-left (as-cast surface with, higher magnification), and bottom-right (elemental map for as-cast surface).....	172
Figure 7. Schematic representation of scale structure evolution from casting to descaling on different surface conditions.....	173

SECTION

Figure 2.1. Defect formation during high temperature reheating	179
--	-----

LIST OF TABLES

PAPER I	Page
Table 1. Composition of samples used in this work (wt. %).	16
Table 2. Test conditions	19
Table 3. Summary of the oxide phases present in the different scale layers (condition 1c, Table 2).	27
PAPER II	
Table 1. Some reported studies on scale formation on stainless steels.....	39
Table 2. Compositions of 430 steels used in this work (wt. %).	42
Table 3. Industrial reheating conditions simulated in laboratory oxidation.	43
Table 4. Oxidation weight gain and reaction delay time (oxidation nucleation) for two studied 430 stainless steels.	46
Table 5. Thickness of oxide layers in the different steel chemistries oxidized at 1150 ⁰ C.....	49
Table 6. Characterization of scale chemistry and oxide phases in 430 ferritic stainless steels and oxide thickness in the different scale layers.	51
Table 7. EDX chemistry and oxide phases in cross-sectional subsurface scale structure in Base steel (Spectrum zones indicated in Figure 4).	52
Table 8. EDX chemistry and oxide phase of cross-sectional subsurface scale structure of Al alloyed steel (zones from Figure 8).	54
Table 9. Experimental vs. thermodynamic predictions of oxide phases in scale layers. ..	57
Table 10. Oxidation Rate Constants and Activation Energies for a Mixed Control Kinetic Mechanism at Different Temperatures for studied 430 Stainless Steels.	60
PAPER III	
Table 1. Composition of studied steels.	80

Table 2. Industrial reheating conditions simulated in laboratory oxidation.	81
Table 3. Characterization of scale chemistry and oxide phases: carbon steel.	85
Table 4. Characterization of scale chemistry and oxide phases AHSS.	88
Table 5. Characterization of scale chemistry and oxide phases in ferritic stainless steels.	91
Table 6. Characterization of scale chemistry and oxide phases in austenitic stainless steel (4).	94
Table 7. Experimental vs. thermodynamic prediction of oxide phases in studied steel grades.	97

PAPER IV

Table 1. Lab Cast steels used in this work (wt. %).	106
Table 2. Industrial reheating conditions simulated in laboratory oxidation.	108

PAPER V

Table 1. Lab cast steels used in this work (wt. %).	130
Table 2. Reheating industrial conditions, which were simulated in laboratory tests.	131
Table 3. Oxide scale composition of low Cu steel (wt. %). Points are from Figure 3). .	136
Table 4. Oxide scale composition of medium Cu steel (wt. %). Points are from Figure 5.	139
Table 5. Oxide scale composition of high Cu steel (wt. %). Points are from Figure 6. .	140
Table 6. Comparison of scale thickness (μm) and structure of complex internal/subsurface layer.	142

PAPER VI

Table 1. Thin slab cast steel used in this work (wt. %).	160
Table 2. Industrial reheating conditions simulated in laboratory tests.	163

Table 3. Oxide scale composition(wt.%) of as-cast surface scale formed prior to reheating (points from Figure 2).	164
Table 4. Oxide scale formed on pre-machined surface during reheating (wt. %). Points are from Figure 3.....	167
Table 5. Oxide scale composition (wt. %) in reheated steel with as-cast surface. Points are from Figure 4.....	168

1. INTRODUCTION

1.1. BACKGROUND INFORMATION

The complexity of scale formation has been described in many studies over the past years [1-10]. During steelmaking process stages such as continuous casting of molten steel to form slabs, reheating of cast slabs to deformation temperature, and hot rolling to transform slabs into different shape for different applications, the surfaces of the slabs come into contact with atmosphere containing oxidizing gases which promotes scale formation. The formation of oxide scale on the surface of cast slab at various processing stages is influenced by a combination of intrinsic factors (steel grade, microstructure, segregation, grain boundary, surface roughness) and extrinsic factors (gas atmosphere, gas flow, furnace pressure, temperature, exposure time, furnace throughput, and mechanical and thermal stresses) [8-13].

The combination of these factors provides conditions for the formation and evolution of oxide scale layers which may have different chemical, physical, mechanical properties, surface topology, adhesion strength, porosity, and thicknesses. Depending on the combination of the intrinsic and extrinsic factors, the formed oxide scale may be easily removed by high pressure hydraulic descaling, or it may be stick to the steel surface and hard to remove leaving behind a residual scale after a descaling practice. The residual scale that remains after a descaling stage in the steelmaking process interferes with subsequent hot rolling process and affects final product quality [10, 11]. Due to the negative impact of residual scale on final product quality, particularly, steels that have application in the automobile and nuclear industry, surface cleanliness is critical to steel

makers. Hence, the knowledge on the impact of atmosphere conditions and steel chemistry on scale formation and its effective removal is very important to steel makers

Fundamental studies of scale growth on steel were done by Sheasby, Boggs and Turkdogan [1] working at US Steel in 80th last century. They found that the mode of scale growth on steels was affected by the furnace atmosphere and presence of water vapor (Figure 1.1). The structure of scale is a multilayer composition of oxide that could be mixed [16] or layered [17] depending on the type of steel grade and oxidation conditions. These oxide layers have different phase compositions [18] in the scale structure consisting mainly of wustite (FeO), magnetite (Fe₃O₄) and hematite (Fe₂O₃) Figure 1.2. The distribution and formation of the different oxide phase compositions is influenced by temperature and time (Figure 1.3).

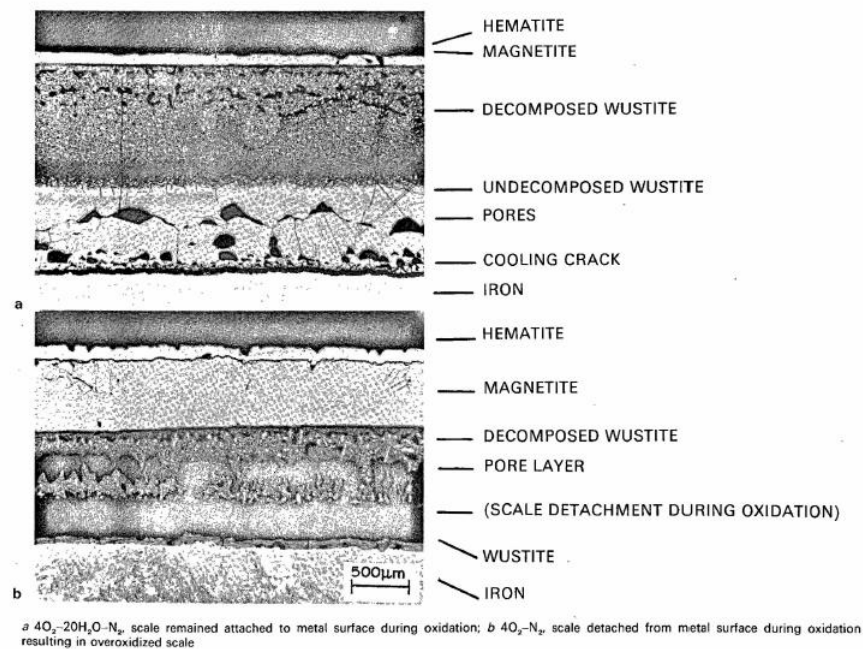


Figure 1.1. Effect of water vapor on scale structure, a) oxidation in moist atmosphere and b) oxidation in dry atmosphere [1].

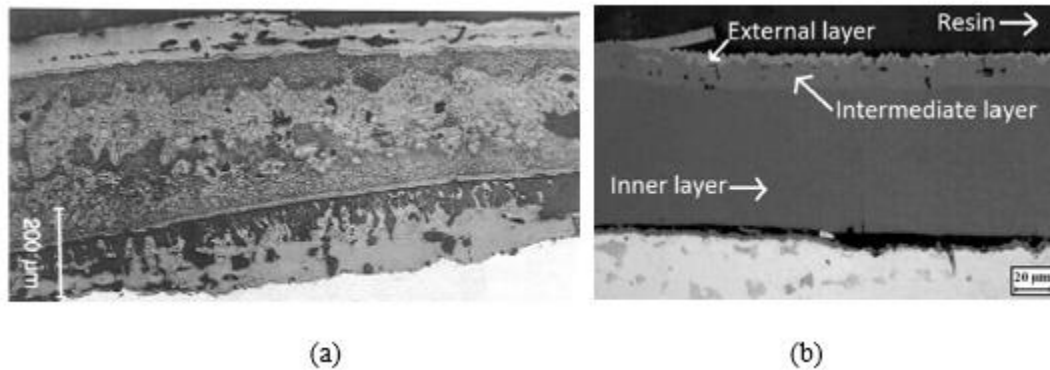


Figure 1.2. Scale structure, (a) Mixed [2] and (b) layered structure of scale (Fe_2O_3 - external, Fe_3O_4 - intermediate and FeO - inner) [3].

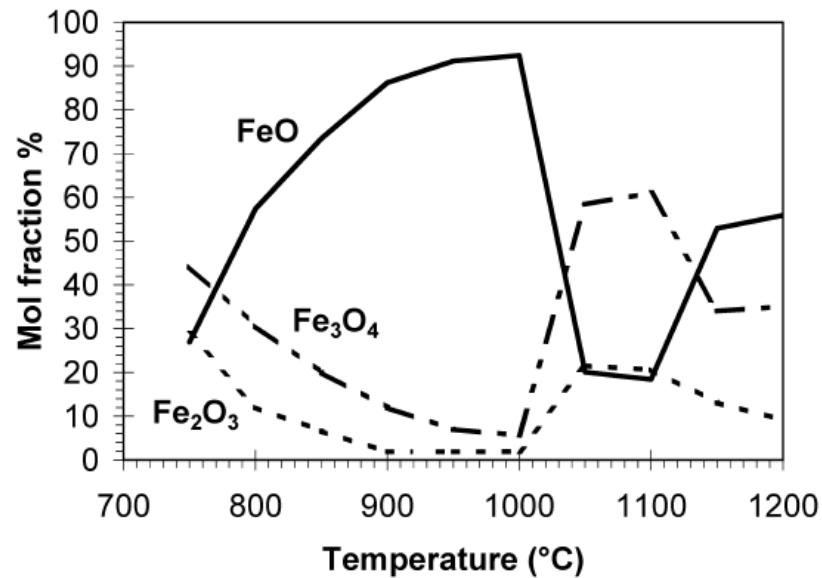


Figure 1.3. Effect of temperature on scale composition [18].

The different oxides phases in a scale structure respond differently to deformation due to the variation in hardness and plasticity [3] (Figure 1.4a) which provide complicated scale behavior during hot rolling slab deformation [8] (Figure 1.4b).

Numerous research into scale formation over the years have reported on how different steel grades affects scale structure formation and formed scale properties. Specific studies

have been focused on low to medium carbon steels [4-7, 10], advanced high strength steel with high *Mn* and *Si* alloying [19], Cr alloyed ferritic [12, 20-27] and *Cr-Ni* alloyed austenitic [11, 28-34] stainless steels. Reports on scale formation studies highlighted on how complex surface and subsurface process [1] (Figure 1.5) affected formed scale structure [35-37].

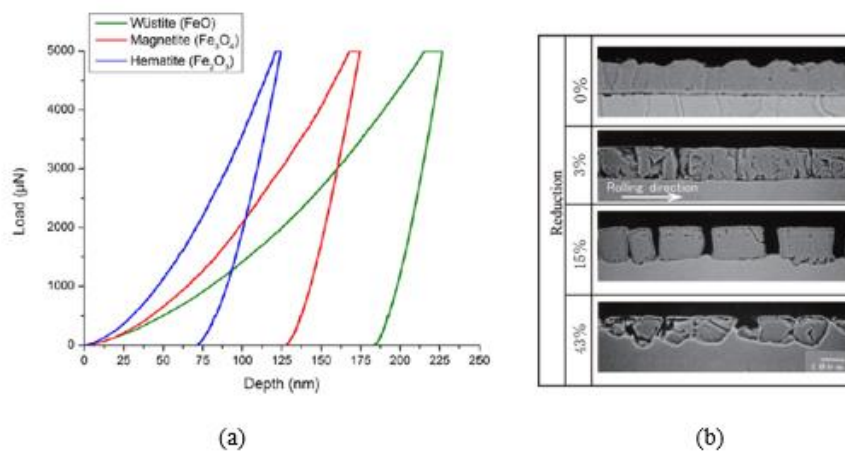


Figure 1.4. Oxide behaviour under deformation, (a) Load vs displacement of different oxides [3] and (b) scale behavior during hot rolling [4].

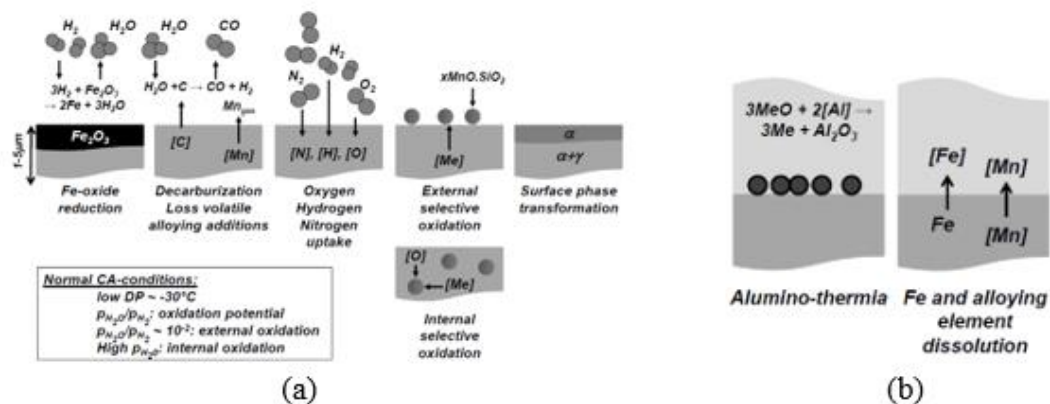


Figure 1.5. Complexity of oxidation, (a) An overview of the surface and sub-surface processes occurring during reheating and (b) processes taking place during oxidation of alloyed steels [1].

1.2. SCALE GROWTH MECHANISM

Two different type of kinetic mechanisms [38,39] have been reported to control the growth of an oxide layer on pure iron or alloyed steel: (i) mass transfer limitation (expressed in equations 1 and 2) and (ii) solid-state diffusion (expressed in equations 3 and 4), with schematic representation of these scale growth mechanism in Figure 1.6.

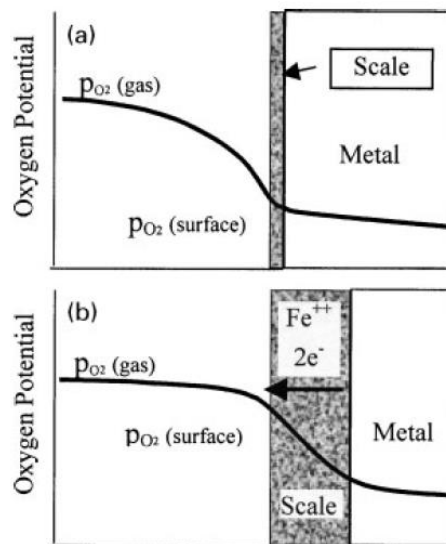


Figure 1.6. Schematic representation of scale growth: a) oxidation controlled by mass transfer in gas phase and b) oxidation controlled by mass transfer through the scale: parabolic or complex oxidation [35]

For a mass transfer control, the rate of oxide growth is controlled by the supply of oxidizing gas to the gas/scale interface and the rate constant depends on gas flow limitation, leading to a linear weight gain *vs* time relationship plot (Figure. 1.7) [37]. The oxide formed is mostly characterized by porosity and flakes which supports a linear relationship expressed as:

$$W = k_1 t \quad (1)$$

where: W is the average weight gain per unit area in grams per square centimeter (g/cm), t is the oxidation time (s), and k_l is the linear rate constant (g/cm² s). For mass transfer control oxidation, the diffusion flux (J_c , mol/cm² s) could be expressed as:

$$J_c = k(c^G - c_s) \quad (2)$$

where: k is the mass-transfer coefficient (cm/s), c^G and c_s (mol/cm³) are the concentrations of oxidant at the gas phase and at the gas/scale interface. Mass transfer limited scale growth are characterized by lower activation energies [37]

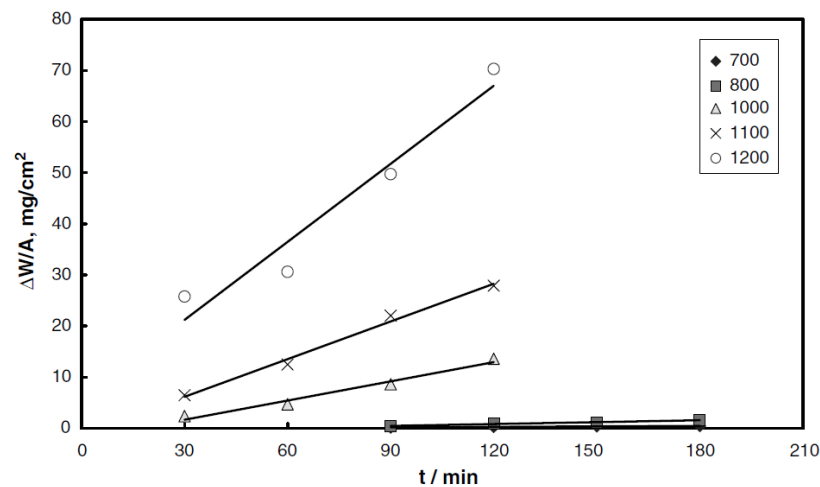


Figure 1.7. Linear oxidation growth kinetics at different temperatures [37]

In the case of solid-state diffusion-controlled mechanism, the oxide growth is limited by resistance from the growing oxide layer thickness and over time, leads to a parabolic weight gain vs time relationship [37]. The solid-state diffusion-controlled mechanism for oxide growth is predominant in oxides that form dense protective films which have been described by the Pilling-Bedworth ratio [40] which measures oxide/metal densities for forming a protective layer.

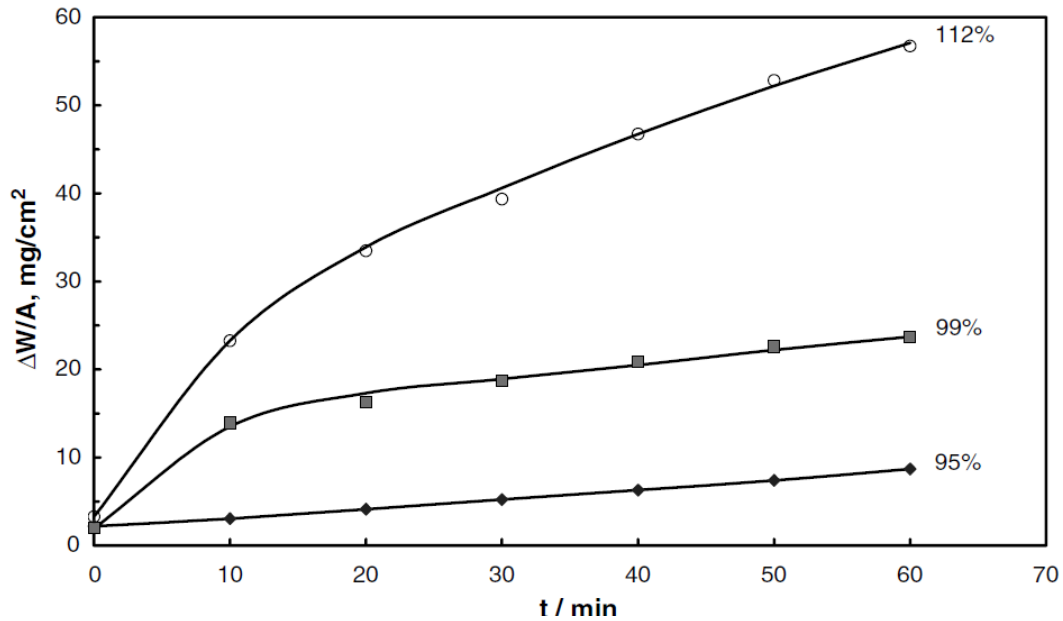


Figure 1.8. Parabolic growth kinetics at different air-fuel ratio (%) [37]

The parabolic rate equation for a growing oxide can be described as:

$$W = k_p t^{\frac{1}{2}} \quad (3)$$

where: the average weight gain per unit area (W , g/cm^2) is proportional to the square root of time (t , s) and k_p is the parabolic rate constant in ($\text{g}^2/\text{cm}^4\text{s}$). For a parabolic rate, the growth of the oxide is influenced by the mobility of species through the oxide layer, which is also influenced by chemical potential gradients, diffusivity of ions, vacancies, and also impurities associated with the metal substrate. For a solid-state diffusion, the flux (J , $\text{cm}^3 \cdot \text{STP} \cdot \text{s}^{-1} \cdot \text{cm}^{-2}$) can be expressed in terms of permeability of the gas species according to Sieverts law (concentration related to oxygen partial pressure) expressed in Eq. 4 as,

$$J = \frac{\rho^*}{\delta} \left(P_o^{1/2} - P_i^{1/2} \right) \quad (4)$$

where: ρ^* is the permeability (at 1 atm) , δ is the length of the boundary layer (cm), P_o and P_i are the partial pressures of the gas at the oxide/gas interface and the oxide/metal interface accordingly (atm).

Both linear and diffusion-controlled scale growth mechanism are predominant in oxidation mostly conducted in air. In the case of real-world kinetics in a reheat furnace containing complex combustion gas atmosphere (CO_2 , H_2O , N_2 , O_2), the rate of scale growth may change during oxidation. The oxidation rate usually starts with an initial linear rate at the onset of oxidation, assumes of a parabolic relationship in the middle of the oxidation period and finally end with a non-linear rate. In most cases, real-world scale formation would be a mixture of both parabolic and linear oxidation relationship.

Formation of multilayered scale structure and the development of internal defects such as cracks and porosities are predominant in real world oxidation kinetics [35-37]. These changes in the growing oxide structure due to defect formations impact on the oxidation mechanism [35, 41] making it difficult to mathematically model scale growth. The changes have been reported to be initiated by detachment of the growing oxide structure from the metal substrate due to density difference and volume expansion caused by internal stress in different oxide phases which promotes crack propagation in complex gas atmospheres [35,42]. The propagations of crack in a growing oxide layer disrupt classical diffusion-controlled mechanism by short-circuiting the diffusion path, breaking boundary layer condition of solid-state diffusion and providing channels through which oxidants from the gas phase permeate to the oxide/metal interface through the thickness of the growing oxide [35].

In combustion gas atmosphere containing water vapor, porosities may develop at the oxide/metal interface due to vacancies defects which adds to the complexity of the rate controlling mechanism [43]. The composition of combustion gas atmosphere has seen significant dependence of scale formation rate (Figure 1.9), with oxygen been the most predominant oxidant during scale formation [35].

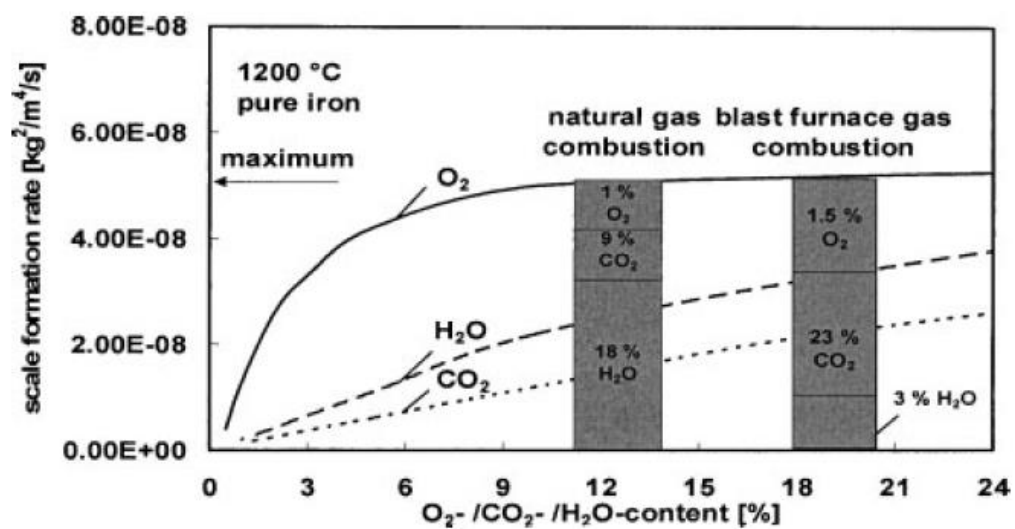


Figure 1.9. Dependence of scale formation rate on combustion gas composition [35]

1.3. SCALE REMOVAL

Scale removal is an importance practice in the steelmaking process. The efficiency of scale removal impacts significantly on the final product quality and subsequent rolling process [44,45]. Scale removal practices are achieved through hydraulic descaling (Figure 1.10a) [46] which normally occurs after slab reheating prior to hot rolling (primary descaling). However, depending on the intensity of scale formation, the descaling step could be incorporated with the hot rolling step, up to 3

passes (secondary descaling). The efficiency of descaling is highly affected by the formed scale characteristics [3, 35, 47] and descaling process parameters including nozzle design [48-51], hydraulic parameters [46,52] and process mechanical design, (Figure 1.10b).

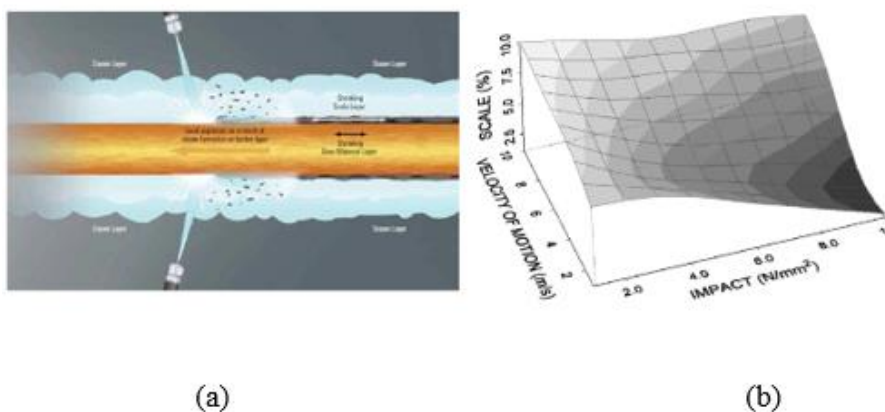


Figure 1.10. Scale Removal, (a) Schematic of hydraulic descaling [30], (b) Effect of hydraulic parameter on descaling (velocity and impact factor) [37]

A well known property of scale characteristics that affects scale removability is strong adhesion of formed scale. Steels containing high *Si*-levels have been known to have strong adhesion at the oxide/metal interface [35]. The challenge with removing scale formed on *Si*-steel grades have been linked to the formation of $FeO-SiO_2$ oxide eutectic during reheating at high oxidation temperature above 1200°C (Figure 1.11a). The eutectic phase has high wettability at the oxide/steel interface which penetrates the metal matrix to form a strong adhesion bond which is difficult to remove. Incomplete removal of adherent oxide phases leads to the formation of multiple mill defects [47] which affects product quality (Figure 1.11b). Impurities (high Ni levels) in steel chemistries have also

been reported to reduce scale removability due to the formation of uneven oxide/metal interface [53].

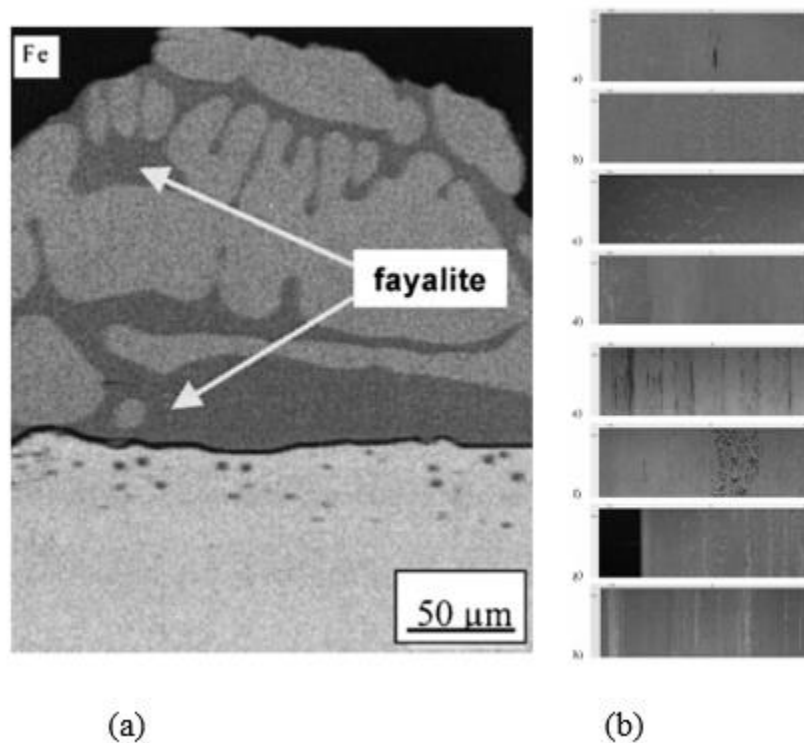


Figure 1.11. Scale defects, (a) Fluid fayalite-wustite eutectic formed at 1200°C (0.8C-1.2Si) [35]; (b) Types of mill scale defects [47]

The characteristics of the formed oxide scale is highly influenced by steel chemistry, temperature, and furnace atmosphere conditions. Multiple factor interference during reheating leads to complex scale formation and affects its removal, the steel industry needs urgent comprehensive analysis on how specific factors affect scale formation, the impact these factors have on scale removal and how scale removal efficiencies can be improved in different steels

1.4. RESEARCH OBJECTIVES

Complexity of scale formation relating to many unknown combinations of intrinsic and extrinsic factors makes it difficult to control quality of descaled surfaces. The major objectives of this research are to investigate, document and evaluate the effect of steel composition and operating parameters on scale formation and scale removal efficiencies.

Specific research objectives are:

1. Simulate industrial oxidation kinetics in laboratory conditions
 - a. Design experimental TGA setup with controlled atmosphere to mimic industrial reheating condition
 - b. Investigate oxidation kinetics of different types of steels (carbon, high strength and stainless)
 - c. Investigate effect of alloying element on scale structure and morphology
 - d. Investigate effect of furnace reheating conditions (temperature, atmosphere)
 - e. Investigate effect of initial surface conditions (as-cast vs milled)
2. Characterize scale formation in different steels (3D optical profiling, SEM/EDX, XRD and Raman spectroscopy, TEM)
3. Develop a kinetic model that will help explain scale formation mechanisms in complex combustion gas atmosphere
4. Use thermodynamic approach to predict scale formation in different steels
5. Design a descaling apparatus for scale removal studies with specific tasks to,

- a. compare descaling in of different steel (industrial and laboratory cast steel grades)
- b. investigate into parameters that would improve scale removal efficiencies in different steel grades

PAPER**I. SCALE FORMATION ON 430 STAINLESS STEEL IN A SIMULATED SLAB COMBUSTION REHEAT FURNACE ATMOSPHERE**

Richard Osei¹, Simon Lekakh¹, Ronald O'Malley¹

¹Peaslee Steel Manufacturing Research Center, Department of Materials Science and Engineering, Missouri University of Science and Technology, Rolla, MO, USA, 65409

ABSTRACT

Scale formed during slab reheating can be difficult to remove by high-pressure descaling, having a negative impact on hot roll surface quality. A large-capacity thermogravimetric apparatus that replicates the combustion atmosphere and temperature in a slab reheat furnace was used to investigate scale formation on 430 stainless steel. Effects of reheating parameters (temperature, time, and atmosphere) on oxidation kinetics were investigated. Oxidized samples were characterized by scanning electron microscopy, Raman spectroscopy and x-ray diffraction to document the microstructure and morphology of scale. Mechanisms for the formation of multi-layered oxide structures that complicate oxidation kinetics and scale removal are discussed.

Keywords: transfer bar, oxidation kinetics, scale structure, oxide phases

1. INTRODUCTION

During continuous castings, reheating, and hot rolling, slab surfaces are exposed to atmospheres containing oxidizing gases, which results in scale formation. The scale formation is affected by a combination of intrinsic (steel grade, microstructure, segregation, grain boundary, surface roughness) and extrinsic (gas atmosphere, temperature, exposure time, mechanical and thermal stress) factors. The combination of these factors provides conditions for the formation and evolution of oxide multilayers with different chemical, physical, mechanical properties, surface topology, adhesion strength, porosity, and thicknesses. Depending on the combination of these factors, the scale that is formed can be adherent to slab surface and difficult to remove or easily removed during descaling [1-2]. In some cases, intermediate slab surface grinding and/or water jet descaling are used to obtain a clean hot rolled product surface.

Scale formation during oxidation is a complex phenomenon which has still not been fully characterized even after numerous studies in the last decades [3-8]. Scale formation in steelmaking begins during continuous casting but it is predominant in the reheat furnace prior to hot rolling. The structures and properties of scale formed in the reheat furnace have been reported to have a significant dependence on the furnace atmosphere [3, 8]. In the case of stainless steel, several studies have been conducted on the type of scale formed on both ferritic [9-13] and austenitic [14-16] steels. Ferritic steels which have high Cr content have been reported to exhibit resistance to oxidation due to the formation of a Cr_2O_3 protective film [14-16]. The effect of temperature and

atmosphere on scale formation on a ferritic stainless-steel grade has been reported [15] to influence the formation of complex scale structures consisting of multiple oxide layers.

The objective of the current research is to study scale formation on 430 ferritic stainless steel under laboratory simulated industrial reheating conditions.

2. EXPERIMENTAL PROCEDURE

Samples used for this work were 430 stainless steel supplied by industry (Table 1).

The two steel chemistries varied in *Al* content (high and low).

Table 1. Composition of samples used in this work (wt. %).

	<i>Cr</i>	<i>Al</i>	<i>C</i>	<i>Si</i>	<i>Cu</i>	<i>Ni</i>	<i>Mn</i>
High Al	16	0.210	0.04	0.5	0.25	0.2	0.4
Low Al	16	0.005	0.04	0.4	0.25	0.2	0.4

The samples were supplied in the form of as-cast slabs (Condition 1) and transfer bars (Condition 2). Initial scale characterization was conducted on the as-cast slab (Condition 1a) to analyze the scale structure formed during continuous casting and on transfer bar after hot roughing (Conditions 2a) to analyze the scale which remained on the reheated slab and hot rolled transfer bar after descaling. Specifically, the transfer bar used in this study was industrially reheated at 1150°C for 2 hours in the soaking zone of a walking beam furnace prior to hot rolling. This bar was subjected to primary and secondary descaling during reversing hot rolling to the transfer bar thickness. The goal of the initial characterization was to document the evolution of industrial scale formation

after casting, hot rolling, and descaling. Specimens for this study, 50x20x3.5 mm, were carefully machined from the near-surface region of the as-cast slab and transfer bar. The initial scale was studied in cross sections (Condition 1a and 2a). To preserve oxidized layer, specimens were coated by epoxy before cutting.

To simulate industrial scale formation in the laboratory, the second set of specimens with the same dimensions was prepared from the as-cast slab. The sample 1b had one as-cast surface and one pre-machined surface, while samples 1c and 1d were machined on both surfaces. The samples 2b and 2c that were taken from transfer bar all had machined surfaces. The pre-machined surfaces of these specimens were milled to the depth of 2-5 mm below the oxidized layer and the specimens were ground with a 60-grit silicon carbide wheel to obtain smooth surfaces. To prevent rusting prior to testing, surfaces were preserved by immersion in ethanol.

To study the oxidation kinetics, thermo-gravimetric oxidation experiments were performed using a vertical $MoSi_2$ resistance-heating tube furnace (Model D900438 ATS Inc.). A high-purity alumina tube with an internal diameter of 53 mm and the tube base sealed with gas-tight cap was used as the reaction chamber (Figure 1). The top of the reaction tube was insulated with a 52 mm diameter high temperature ceramic fiber tube cap, with a center opening of 10 mm diameter just large enough to enable a 1 mm diameter wire to pass through it without touching the walls. This configuration was sufficient with the gas flowrates employed to prevent air ingress. A +/-1 microgram precision microbalance with a bottom hook which allowed specimens to be suspended in the furnace reaction chamber on a nichrome wire was used to monitor the specimen weight. The specimen was suspended inside a catch basket to collect any spalled scale

during oxidation. The atmosphere of the industrial reheating furnace was simulated in the lab by mixing gases in proportions that reproduced the natural gas combustion atmosphere in an industrial furnace at a partner company. The composition gas mixture was controlled using a multi-channel mass flow control system and a controlled temperature water saturation system. Excess oxygen levels of 3 and 5 vol. % were chosen for the testing based on observed industrial reheat furnace operating conditions. The incoming gas stream and actual specimen temperature were controlled based on parameters optimized in preliminary calibration and verification experiments.

Industrial reheating temperature and atmosphere conditions were simulated in these experiments. The lab furnace was preheated and stabilized at the desired test temperature (1150°C). The gas mixture was allowed to run through the preheated furnace for 30 minutes at a flow rate of 500 ml/min prior to the actual oxidation experiment to equilibrate the furnace atmosphere. Weight gain of the specimen was continuously recorded during the oxidation experiment which typically lasted for 2 hours. Upon completion of the oxidation experiment, the specimen was cooled to room temperature in a continuously flowing argon atmosphere to prevent further oxidation. Sample weights were recorded after oxidation, including the weight of any spalled scale in the catch basket. The test conditions are described in Table 2.

A 3D optical profiler (Nanovea, Model PS50 Micro Photonic Inc.) was used to characterize topology and roughness of the as-formed scale surfaces. The samples were then mounted in epoxy, sectioned, ground using silicon carbide abrasive papers to 1200 grit and mechanically polished with 0.1 μm diamond paste for metallographic analysis. The morphology, thickness, microstructure, and chemistry of the oxide layers were

analyzed with a scanning electron microscopy (SEM) using an ASPEX-PIXA 1020 system equipped energy dispersive spectroscopy (EDS). Raman spectroscopy and XRD analysis was also used to identify the oxide phases that were present.

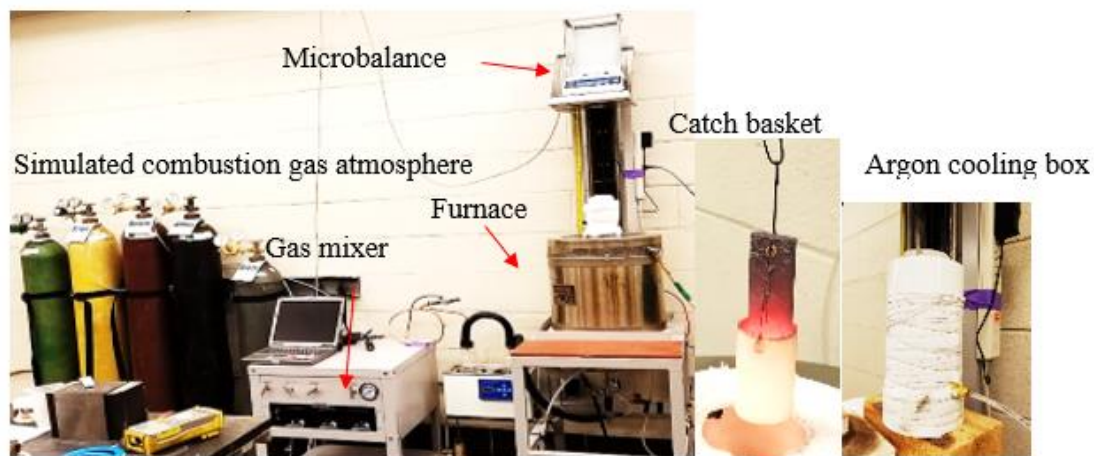


Figure 1. TGA experimental setup.

Table 2. Test conditions

Condition	Chemistry description	Surface condition	Atmosphere	Combustions gas vol. %	Temperature, °C
1a-cast slab	Low Al	as-cast	No-reheating		1150
1b-cast slab	Low Al	as-cast	3% O ₂	8CO ₂ , 73N ₂ , 16 H ₂ O, 3O ₂	
1c-cast slab	Low Al	ground	3% O ₂	8CO ₂ , 73N ₂ , 16 H ₂ O, 3O ₂	
1d-cast slab	Low Al	ground	5% O ₂	7CO ₂ , 73N ₂ , 14 H ₂ O, 5O ₂	
2a-transfer bar	Low Al	as supplied	No-reheating		
2b-transfer bar	High Al	ground	3% O ₂	8CO ₂ , 73N ₂ , 16 H ₂ O, 3O ₂	
2c-transfer bar	Low Al	ground	3% O ₂	8CO ₂ , 73N ₂ , 16 H ₂ O, 3O ₂	

3. RESULTS

3.1. INDUSTRIAL SCALE EVOLUTION FROM AS-CAST TO HOT ROLLED CONDITIONS

The sample used for the as-cast industrial scale characterization (condition 1a) was a low in Al 430 ferritic stainless steel. The overall thickness of the scale layer on the as-cast sample was around 80 μm . Figure 2a highlights the structure and Figure 2b illustrates the chemistry of the scale formed on the as-cast slab prior to industrial reheating. A complicated scale structure with 4 different layers was observed. This scale structure was strongly attached to the metal substrate and only a few internal cracks between the layers were observed. The outermost scale had a thick external layer, A, which had a high Ca content, which could be an indication of mold powder residue. Ca was also observed in the deep inner layer, C, and was also detected in the subsurface layer D. The chemistry of the outer layer, A, had traces of iron oxide with high Si and Ca, the next layer B was iron oxide with some Cr, and near substrate layers C and D were a mixture of iron oxide with high Cr and traces of Ca and Si. Raman spectroscopy on the scale structure revealed Fe_2O_3 , Fe_3O_4 , and Fe_2SiO_4 as oxide phases in layer A, Fe_3O_4 in layer B, and Fe_2SiO_4 and FeCr_2O_4 in layers C and D (Figure 3).

The scale on the industrial hot rolled and descaled transfer bar (condition 2a) was significantly different from the scale observed on the as-cast slab. The average scale thickness on the transfer bar sample was 60 μm . Figure 4 illustrates the structure and chemistry of the scale formed after reheating that survived on the transfer bar after descaling. The scale had a fine dense grain structure in the outer layer, larger grains in the intermediate layer, and fine compacted grains in the subsurface. The scale which

remained after descaling was strongly attached to the metal substrate. Oxide phases present in the scale structure were identified to be Fe_3O_4 , Fe_2SiO_4 and $FeCr_2O_4$.

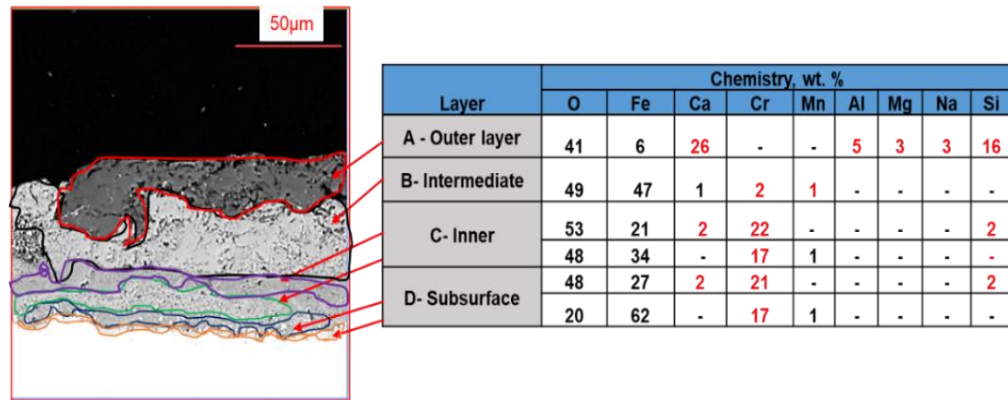


Figure 2. Industrial oxide scale structure of 430 stainless steel as-cast slab: Left: BSE image with outlined layers in scale and Right: EDX analysis chemistry of oxide layers.

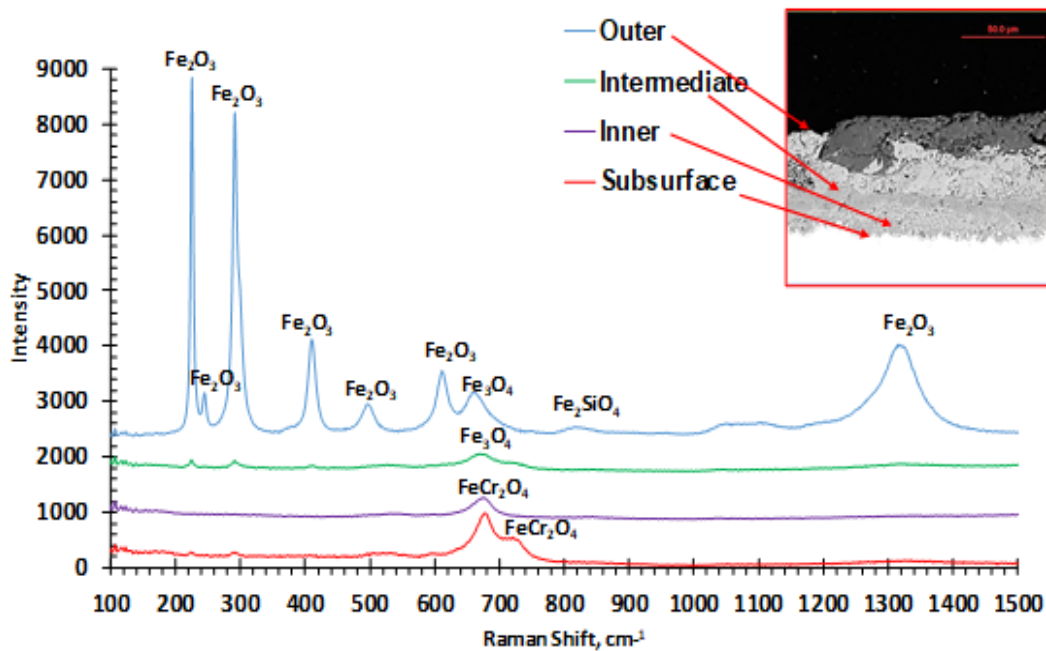


Figure 3. Raman spectroscopy of 430 stainless steel industrial as-cast scale structure, indicating oxide phases present in the various scale layers.

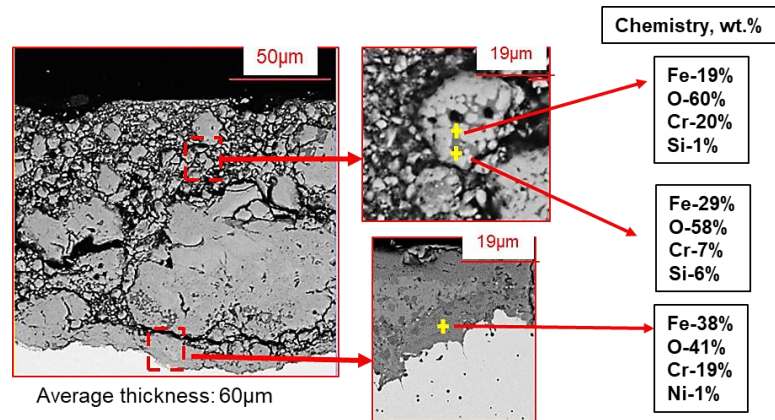


Figure 4. BSE image of scale structure with EDX analysis of industrial scale on transfer bar (reheated, hot rolled, and descaled).

3.2. OXIDATION KINETICS IN SIMULATED REHEATING FURNACE

To better understand the observed evolution of scale from as-cast slab to transfer bar, laboratory tests were performed under controlled oxidation conditions (Table 2). These tests were performed for 2 hours at 1150°C in a combustion gas atmosphere with two different excess oxygen levels. Figure 5 and Figure 6 show the oxidation weight gains vs. time for the oxidation conditions listed in Table 2. The oxidation behavior for the as-cast vs. mechanically ground surfaces of low *Al* 430 stainless steel in a 3% oxygen combustion gas atmosphere are compared in Figure 5a (conditions 1b vs 1c). The oxidation rate was higher for the as-cast surface and the weight gain curve exhibited a nonlinear shape compared to a closely linear shape for the ground surface condition.

The effect of different combustion atmospheres (3% vs. 5% oxygen, conditions 1c vs 1d) is shown in Figure 5b. The oxygen content did not affect the initial growth rate of oxidation. However, the specimen tested at the higher oxygen level displayed a lower oxidation rate at longer times. The higher oxygen level promoted a more nonlinear oxidation behavior, while atmosphere with less oxygen promoted a more linear oxidation

rate trend towards the end of the oxidation period. The observed oxygen level dependence is unexpected, and mechanisms responsible for the observed oxidation behavior will be discussed in the following section of this paper.

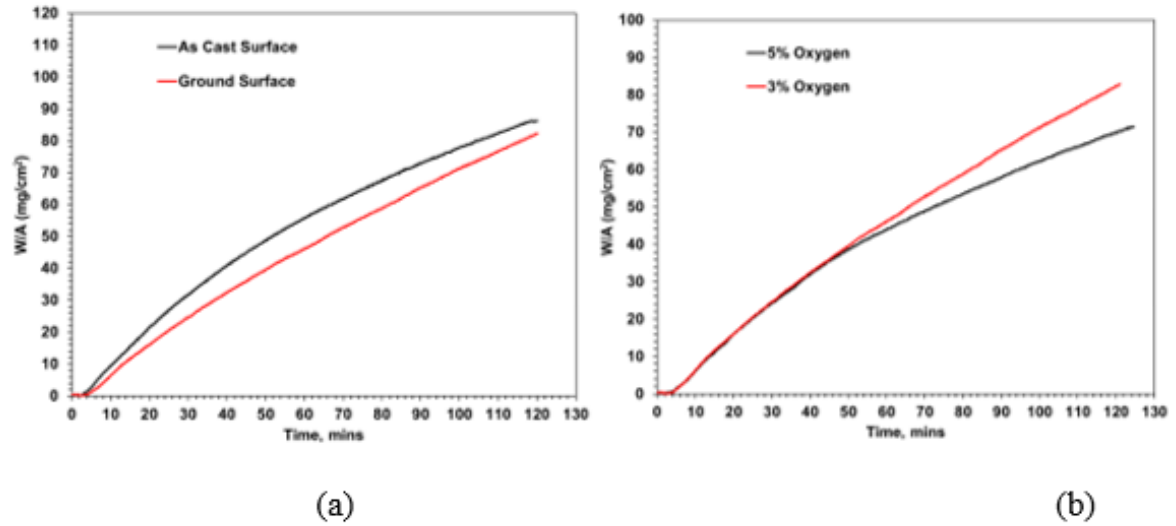


Figure 5. Oxidation kinetics of low Al 430 stainless steel (as-cast slabs) measured by TGA isothermal heating: (a) as-cast (condition 1b) vs. pre-machined (condition 1c) surface condition in combustion gas with 3% oxygen and (b) effect of oxygen in combustion atmosphere for ground surface condition (conditions 1c (3% O₂) and 1d (5% O₂) from Table 2.

To study the effects of high vs. low Al steel chemistry on its oxidation behavior of 430 stainless, machined specimens were taken from the transfer bars (condition 2b and 2c, Table 2). These tests were performed with a 3% excess oxygen atmosphere. The overall oxidation rate was observed to be higher for the low Al specimen. A nonlinear oxidation rate was observed in both steels (Figure 6). The weight change vs. time did not follow simple linear, parabolic, or combined growth laws. The high Al specimen also exhibited longer initial delay before the onset of oxidation.

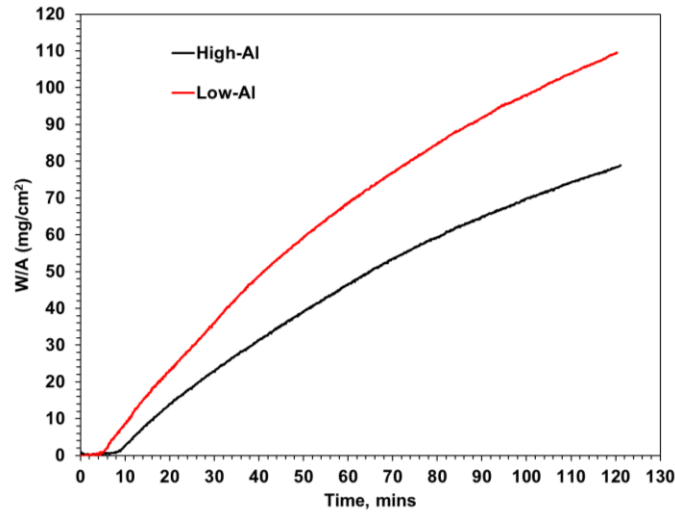


Figure 6. Oxidation rate of 430 stainless steel with different Al in transfer bars (conditions 2b vs 2c, Table 2).

4. DISCUSSION

4.1. EFFECT OF SURFACE CONDITIONS: AS-CAST VS. GROUND

Optical microscopy, SEM and optical surface profiling were employed initially to examine and document the scale structure. Figure 7 shows a typical analysis for the as-cast low Al 430 stainless steel specimen - condition 1c from Table 2. This specimen exhibited significant scale detachment from the substrate during the test. Two different scale layers were observed: one identified as the outer detached (top pictures in Figure 7) and one as the intermediate attached (bottom pictures) oxide layer. The external layer exhibited a coarse dense grain structure with a surface roughness depth of +/- 200 μm , while the intermediate layer had a fine surface structure with roughness depth of +/- 125 μm .

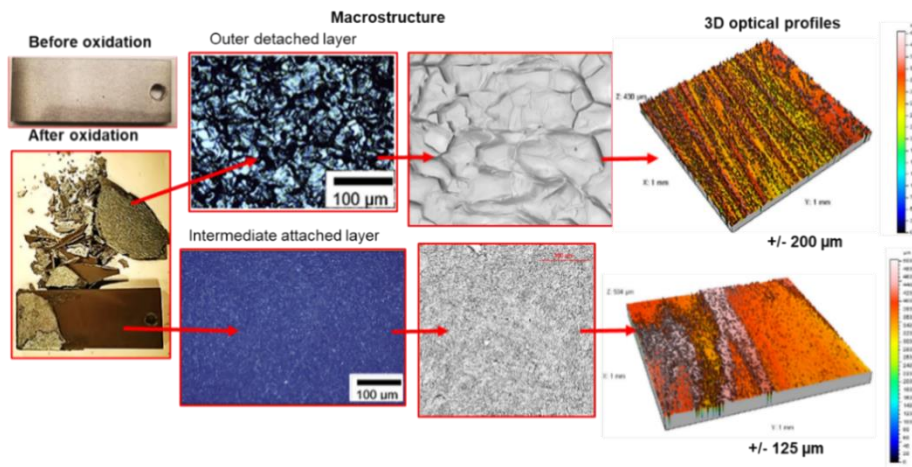


Figure 7. Surface structure of low Al 430 stainless steel sample (condition 1c, Table 2).

Examination of this specimen in cross-section revealed a complex scale structure which exhibited distinct outer, intermediate, inner, and subsurface layers. The average thickness of the oxide layer was measured to be 850 μm , with the outer, intermediate and inner layers representing up to 95% of the scale thickness (815 μm). The subsurface layer was only 20-40 μm thick. These layers contained different chemistries and oxide phases (Figure 8). The outer, intermediate, and partially inner scale layers were detached from the subsurface scale layer that was attached to the steel. The outer layer structure was characterized by dense scale layer with chemistry containing iron oxide with traces of *Mn* and *Cr*. The intermediate layer had round shaped porosity coupled with elongated micro-cracks. The chemistry and oxide phases in the intermediate layer were predominantly chromite, while the inner layer contained a chromite phase with impurities of *Ni* and *Cu*, and a fayalite phase that was rich in *Si*. The subsurface layer was strongly attached to the metal substrate and had a mixture of oxide grains in the metal matrix. Two different chromite layers were observed in the subsurface, high *Cr* with traces of *Si* and low *Cr*

with high *Si* content. Raman spectroscopy analysis of oxides presents in the different multi-scale layers are presented in Figure 9 and Table 3.

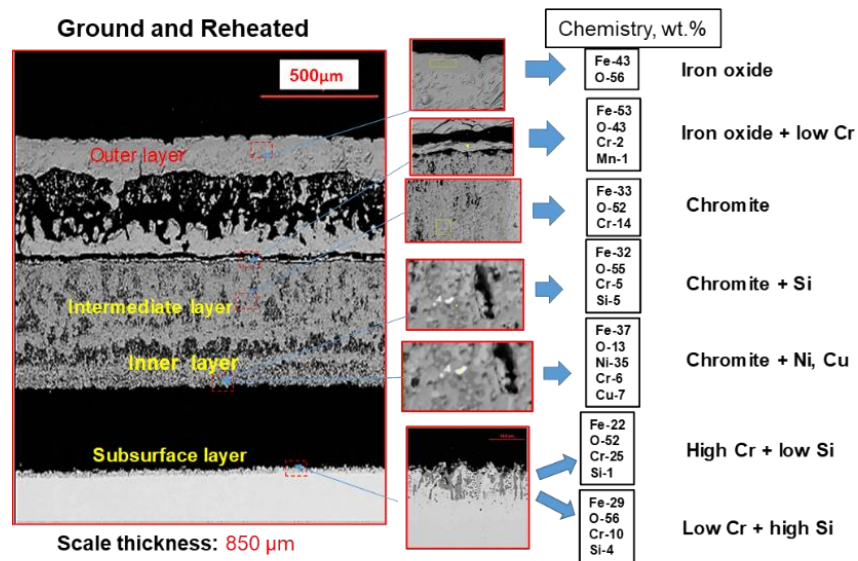


Figure 8. Scale (condition 1c, Table 2) in cross section showing the multi-layer oxide structure.

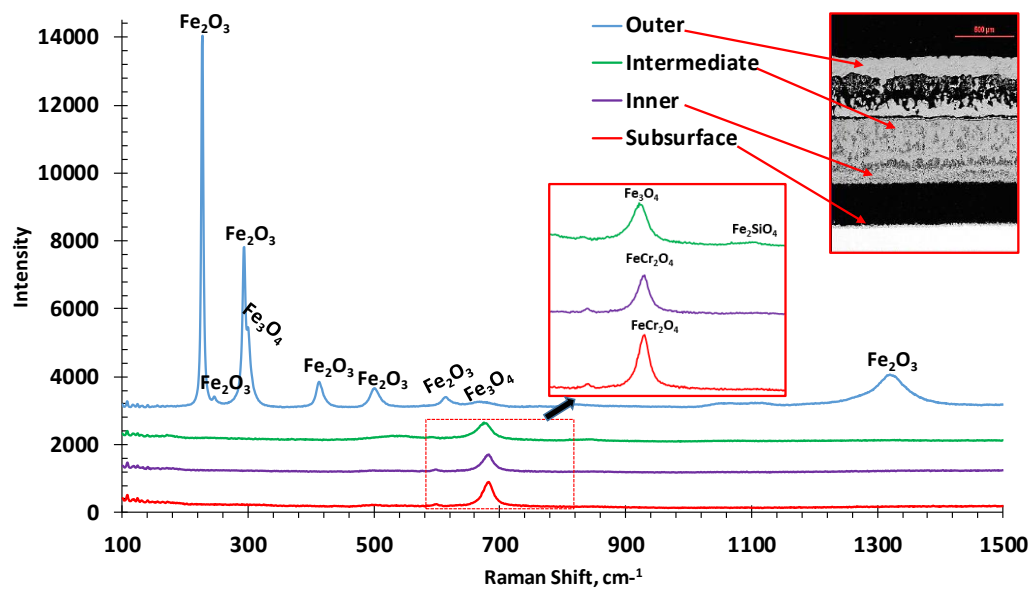


Figure 9. Raman spectroscopy of oxide phases in specimen 1c from Table 2.

Table 3. Summary of the oxide phases present in the different scale layers (condition 1c, Table 2).

Oxide layer	Oxide phases
Outer layer	Fe_2O_3 , Fe_3O_4
Intermediate	Fe_3O_4 , FeCr_2O_4 , Fe_2SiO_4
Inner	Fe_2SiO_4 + FeCr_2O_4
Subsurface	Fe_3O_4 , FeCr_2O_4 , Fe_2SiO_4

Figure 10 presents the scale structure for the low *Al* steel reheated with the as-cast surface and Figure 11 compares subsurface structure for reheated as-cast and ground surface. Comparing the subsurface layers for the two different oxidation conditions (1b vs 1c) revealed different chemistries in the subsurface area. Sample condition 1c (ground surface) contained chromite with two different *Si* levels while condition 1b (surface with as-cast scale) revealed the presence of *Ca* in the sublayer. The subsurface chemistry of condition 1b implies that mold flux interacted with the subsurface layer early in the oxidation process, possibly while it was still in the caster or at early times in the reheat furnace. There was a significant change in the thickness of the subsurface layer for these two conditions. The steel with as-cast surface (1b condition) had a subsurface thickness between 80-110 μm which was 3 times thicker than that of ground surface layer thickness, 1c (20-40 μm).

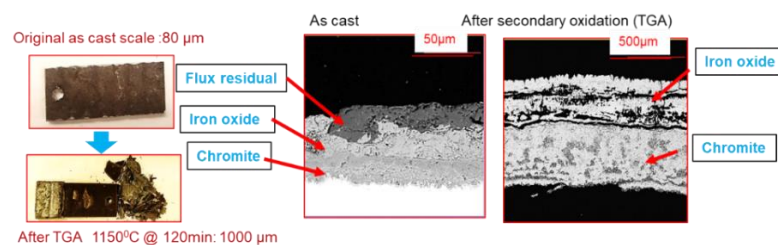


Figure 10. Scale (condition 1a and 1b, Table 2) in cross section, showing different multi-layer oxide structure in as-cast condition and after re-heating.

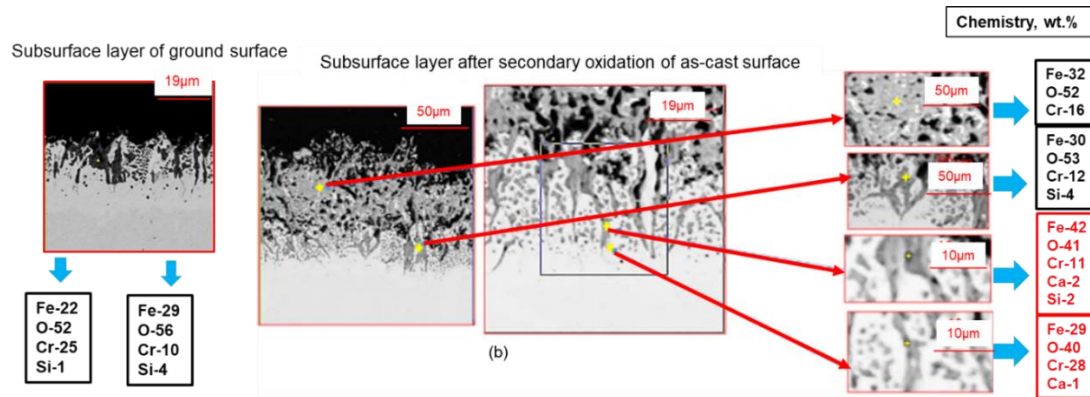


Figure 11. Subsurface structure of re-heated low Al steel as-cast steel with as-cast vs surface ground (conditions 1b vs 1c, Table 2)

4.2. EFFECT OF COMBUSTION ATMOSPHERE

Samples used in this comparison were taken from surface ground as-cast slabs (condition 1c with 3% excess oxygen and condition 1d with 5% excess oxygen, Figure 12). These conditions showed a significant difference in oxidation behavior. Surprisingly, the sample oxidized with 3% excess oxygen exhibited a higher oxidation rate than the sample oxidized with 5% excess oxygen. Two entirely different scale structures were observed in these samples. The scale structure formed in atmosphere with 3% oxygen was highly delaminated and exhibited significant detachment near the metal-oxide interface. This scale detachment may have resulted from internal stress or void formation from differences in the density between the growing oxide layers or from void formation during diffusion controlled growth of the scale layer. Scale delamination and detachment can accelerate scale growth by allowing gas phase diffusion or mass transport to the oxide/metal interface as opposed to solid state diffusion through a dense scale layer. In contrast, no or little detachment was observed near the scale-metal interface in steel oxidized in 5% oxygen atmosphere. This scale in this region had a dense structure

that likely acts as a solid state diffusion barrier to control the scale growth, resulting in the slower growth rate observed in this experiment. The different scale structures can result in different rate controlling mechanisms for scale growth. In particular, a solid state or gas phase diffusion controlled mechanism would lead to the more parabolic-like growth (Figure 5b) observed at higher oxygen potential, whereas gas phase convective mass transfer may dominate the scale growth when oxide detachment occurs, resulting in a linear growth rate. Some kinetics mechanisms responsible for this behavior have been discussed in review articles by Chen, et.al.[17-18]. The reasons why the 3% excess oxygen condition results in scale separation at the oxide metal interface and the 5% excess oxygen condition does not is still not clear at this time.

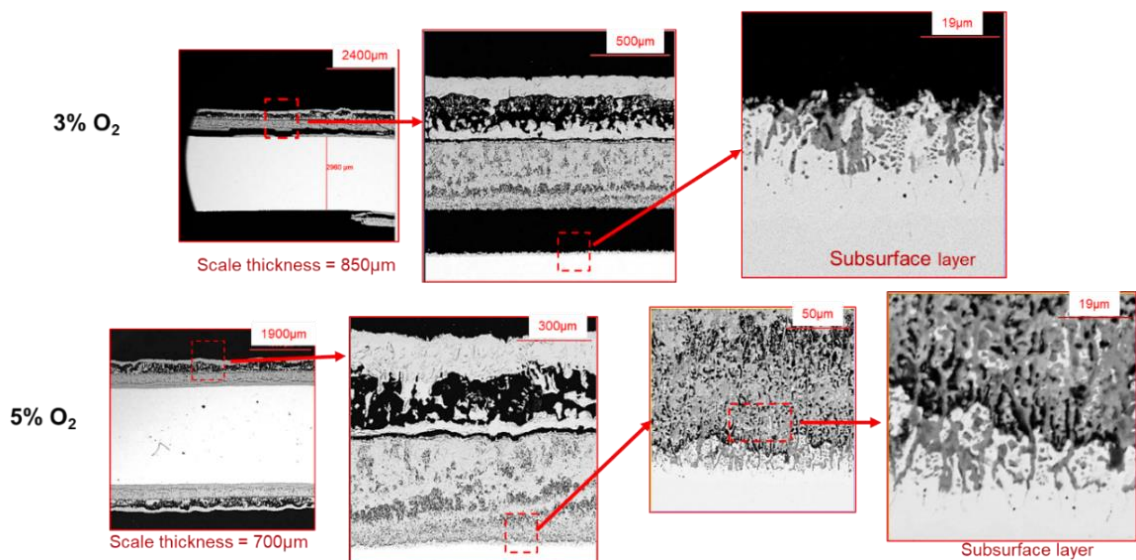


Figure 12. Oxide scale structure of as cast low Al 430 steel oxidized in a combustion gas atmosphere with 3% and 5% oxygen at 1150°C (condition 1c and 1d, Table 2).

4.3. EFFECT OF AL

Samples used in this test were taken from transfer bars having two different *Al* levels (low and high, Table 1) using samples with machined surfaces (condition 2b and 2c). Tests were performed in a simulated combustion atmosphere with 3% excess oxygen. TGA analysis showed a higher oxidation rate in low *Al* steel (Figure 6). A 1 mm thickness oxide layer was developed on the low *Al* steel with its subsurface layer chemistry consisting of Fe_3O_4 , $FeCr_2O_4$, Fe_2SiO_4 (Figure 13). The scale thickness was less than that observed for the high *Al* steel and the presence of *Al* was observed in the subsurface layer chemistry. The presence of alumina in the subsurface could possibly provide an additional barrier to oxidation [16]. This could explain the lower oxidation rate observed for the high *Al* 430 stainless steel.

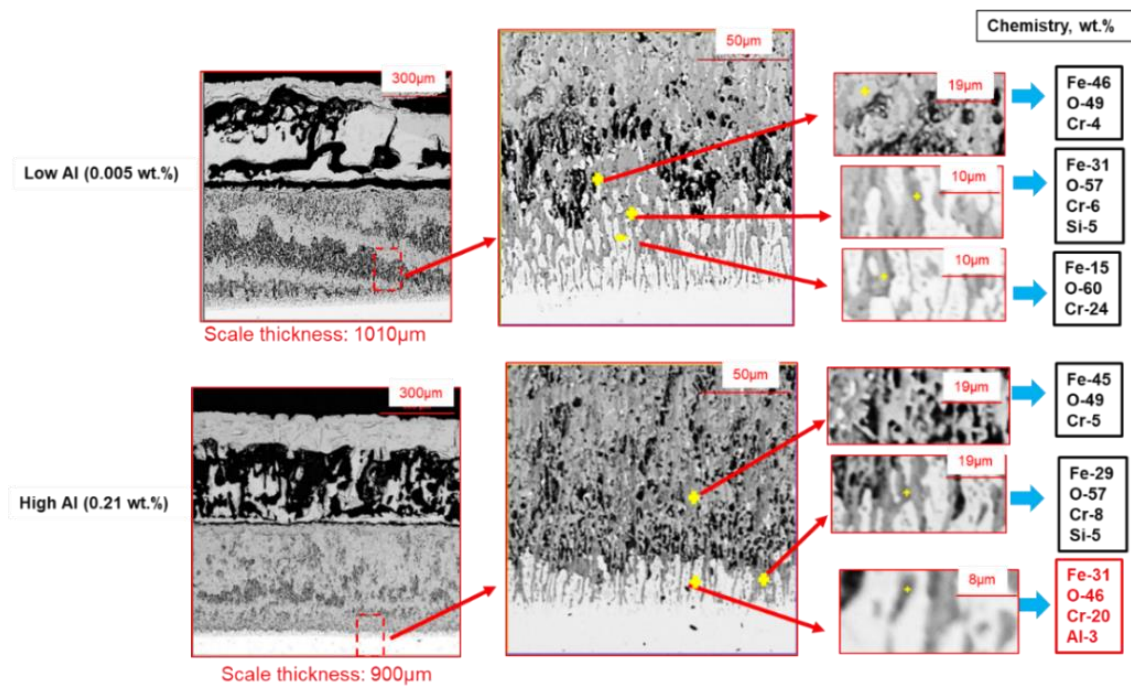


Figure 13. Oxide scale structure of low and high Al 430 steel oxidized in a combustion atmosphere with 3% oxygen at 1150°C (condition 2b and 52c, Table 2).

A theoretical investigation of scale formation on reheated multi-component 430 class stainless steel is planned in future work, considering equilibrium thermodynamic conditions at different oxide layers coupled with diffusion kinetics. Complicated oxide morphologies (detachment, cracks, porosity, different densities of formed phases) make it difficult to accurately predict the overall oxidation rate. However, simulations of thermodynamic equilibrium conditions at different incremental oxygen potentials can be used to predict the expected oxide phases through the thickness of a multi-layered scale structure. This process was simulated by adding progressively increasing amount of oxygen into the gas-steel system using FactSage v7.2 software (Figure 14).

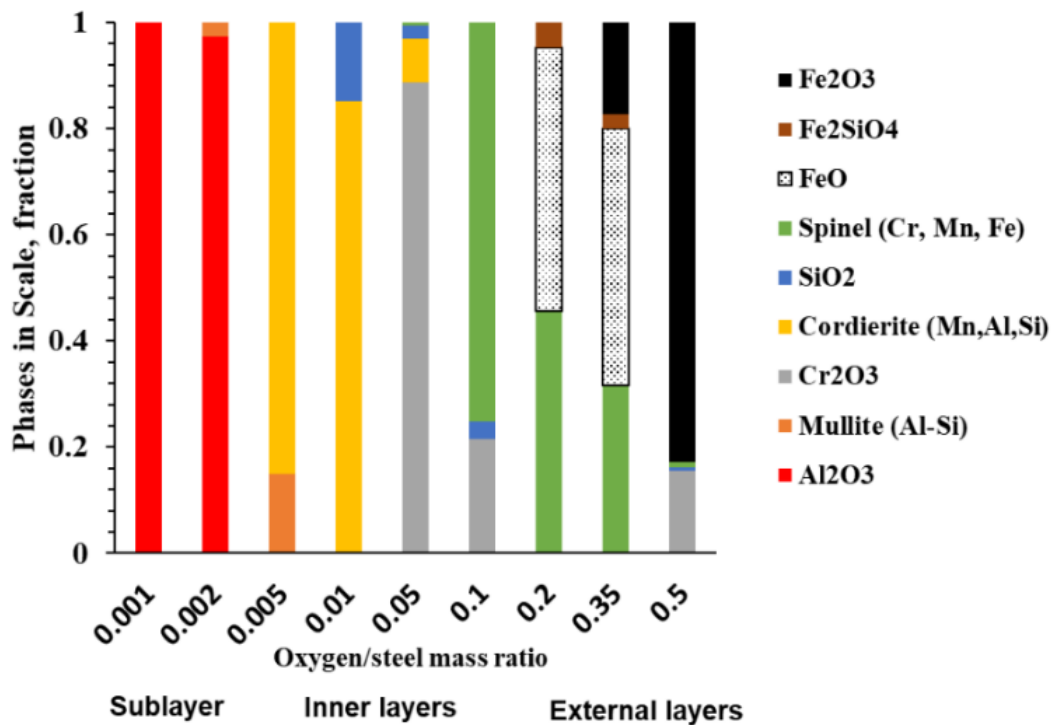


Figure 14. Thermodynamic simulation (FactSage software) of the sequence of formation of different phases in multi-layered oxide formed in high-Al 430 stainless steel grade.

Assuming equilibrium conditions at each incremental level of oxygen potential, the equilibrium oxide phases that were predicted to form at each step were identified. In the high Al 430 steel at 1150⁰C aluminum containing oxides (alumina and mullite) were predicted to be stable in the subsurface layer at low oxygen levels. The intermediate layers at higher oxygen levels were predicted to contain Cr and Si oxides with Mn (complex spinel and chromite), and finally outer layer was predicted to consist of a mixture of different Fe oxides. These predictions compare favorably with compositional analysis of the scales observed in this study.

5. CONCLUSION

Scale formation on 430 stainless steel in a simulated combustion gas atmosphere and on as-supplied industrial slab and transfer bar samples have been characterized. The scale contained multiple layers with different chemistries and oxide phases. Characterization of industrial formed scale revealed the presence of mold flux residue on scale observed on as-cast slabs prior to reheating, having a thickness of about 80 μm, while the scale observed on transfer bars which had been subjected to hot rolling and descaling had a scale thickness of about 60 μm. The surface condition of the 430 stainless steel samples used in the laboratory oxidation experiment was observed to have a significant effect on the thickness of the scale formed, particularly in the subsurface region near the scale-oxide interface. In this work, it was observed that changes in excess oxygen level and 430 steel chemistry both have a significant effect on scale formation in the reheat furnace. When the excess oxygen level in the combustion gas was varied, a

change in the oxidation rate, scale structure, and scale growth behavior was observed. The addition of Al to 430 stainless steel resulted in a decreased oxidation rate and a change in subsurface oxide layer chemistry. Thermodynamic simulations were used to predict the phases formed in the multilayered scale structure. These predictions were in reasonable agreement with experimental observations.

ACKNOWLEDGEMENTS

The authors gratefully acknowledges the support and guidance from the industry advisory committee of Peaslee Steel Manufacturing Research Center.

REFERENCES

1. Stainless Steel Producers, (1984), *cleaning and descaling stainless steel*, 36 pp.
2. Lechwar, S., Rauch, L. and Pietrzyk, M. (2015). Use of artificial intelligence in classification of mill defects. *Steel Research Int.* Vol. 86, No. 3, pp. 266-277.
3. Sheasby, J.S., Boggs W.E. & Turkdogan E.T. (1984). Scale growth on steel at 1200°C: rationale of rate and morphology. *Met. Sci.* 18, 127-136.
4. Sun. W. (2005). A study on the characteristics of oxide scale in hot rolling of steel, PhD thesis, School of Mechanical, *Materials and Mechatronic Engineering*, University of Wollongong.
5. Zambrano, O. A., Coronado, J.J. & Rodriguez. S. A (2015). Mechanical properties and phases determination of low carbon steel oxide scales formed at 1200 °C in air, *Surface and coating technology*, Vol. 282, pp. 155-162
6. Abuluwefa, H.T., Guthrie, R.I.L. and Ajersch, F., (1996). The effect of oxygen concentration on the oxidation of low-carbon steel in the temperature range 1000 to 1250°C, *Oxidation of Metals*, 46, 423-440.

7. Boggs, W. E., (1973). The role of structural and compositional factors in the oxidation of iron and iron-based alloys in high temperature gas-metal reactions in mixed environments, *Metallurgical society of AIME*, 84-128.
8. Abuluwefa, H.T., Guthrie, R.I.L. and Ajersch, F., (1997). Oxidation of low carbon steel in multi-component gases: Part 1. Reaction mechanisms during isothermal oxidation, *Metallurgical and Materials Transactions series A*, 28, A, 1633-1641.
9. Brady, M.P., Yamamoto Y, Lu, Z.P., Liu, C.T., Maziasz, P.J. and Pint B.A. (2007). Oxidation resistant, high creep strength austenitic stainless steel, *United States Patent Disclosure*.
10. Brady, M.P., Yamamoto Y, Santella M. L., and Pint B.A. (2007). Effects of minor alloy additions and oxidation temperature on protective alumina scale formation in creep-resistant austenitic stainless steels, *Scripta Materialia*, 57, pp. 1117-1120.
11. Otsuka, N., Nishiyama, Y. and T. Kudo., (2004). Breakaway oxidation of TP310S stainless-steel foil initiated by Cr depletion of the entire specimen in a simulated flue-gas atmosphere, *Oxidation of Metals*, vol. 62, no. 1-2, pp. 121–139.
12. Asteman, H., Svensson, J.-E. and Johansson, L.-G., (2002). Evidence for chromium evaporation influencing the oxidation of 304L: the effect of temperature and flow rate, *Oxidation of Metals*, vol. 57, no. 3-4, pp. 193–216.
13. Laukka, A., Heikkinen, E-P. and Fabritius, T., (2018). In-depth oxide scale growth analysis of B and Ti micro alloyed AISI 304 in oxygen-containing furnace atmosphere and CH₄ burn-simulation furnace atmospheres, *Steel Research Int.* 11 pp.
14. Zhang, Y., Shi, A., Liang, P., Wang, J., Meng, H., Zhang, C., Zhang, Z. and Han, P. (2018). High-temperature initial oxidation behavior in LDX 2101, *Steel Research Int.* Vol. 89, 7 pp.
15. Cheng, X., Jiang, Z., Wei, D., Zhao, J., Monaghan, B. J., Longbottom, R. J. & Jiang, L. (2014). Characteristics of oxide scale formed on ferritic stainless steels in simulated reheating atmosphere. *Surface and Coatings Technology*, 258 257-267.
16. Bavay, J. C. and Bourgain, P. (1987). Effect of Aluminum and Silicon on the Oxidation Resistance of 13% Cr-Ti Ferritic Stainless Steel. *Materials Science and Engineering*, 87, pp. 137-143.

17. Chen, R. Y. and Yuen, W. Y. D. (2010). Short-time oxidation behavior of low-carbon, low silicon steel in air at 850-1180°C: II linear to parabolic transition determined using existing gas-phase transport and solid-phase diffusion theories. *Oxid Met*, Vol. 73, pp. 353-373.
18. Chen, R. Y. and Yuen, W. Y. D. (2003). Review of the high-temperature oxidation of iron and carbon steel in air or oxygen, *Oxidation of Metals*, Vol. 59, No. 5/6 pp. 433-468.

II. EFFECT OF AL ADDITIONS ON SCALE STRUCTURE AND OXIDATION KINETICS OF 430-FERRITIC STAINLESS STEEL REHEATED IN A COMBUSTION ATMOSPHERE

Richard Osei¹, Simon Lekakh¹, Ronald O'Malley¹

¹Peaslee Steel Manufacturing Research Center, Department of Materials Science and Engineering, Missouri University of Science and Technology, Rolla, MO, USA, 65409

ABSTRACT

Al is sometimes added to ferritic 430 type stainless steel to improve the surface appearance of cold rolled bright annealed products. High surface quality is required for such applications. However, during continuous casting, slab reheating, and hot rolling, complex oxides can penetrate deep into the matrix and form highly adherent subsurface scale layers that resist removal using high pressure water descaling. Therefore, an understanding of the oxidation phenomena during reheating in the combustion atmosphere of the slab reheating process is critically important for control and elimination of potential scale related surface defects on the product. In this article, the kinetic aspects of oxidation and scale formation on a standard and an *Al* alloyed 430 ferritic stainless steel were investigated using several experimental and modeling methods. Experiments were performed in a TGA apparatus that replicates the combustion gas atmosphere and temperature in an industrial slab reheat furnace. Oxidized samples were characterized using optical microscopy, scanning electron microscopy (SEM), and

Raman spectroscopy to document the specific changes in the scale morphology and microstructure in the base and *Al* alloyed 430 ferritic stainless steels.

Focused ion beam (FIB) sectioning of the scale layer, followed by high resolution transmission electron microscopy (TEM), revealed details of the phase, composition and structure of the oxides formed in the subsurface region of the ferritic matrix.

Thermodynamic simulations were used to predict phases in the multilayer scale structure. Differences in oxidation kinetics, phase, composition, topology, and microstructure of the multi-layered scale formed during re-heating of the investigated alloys are discussed.

Keywords: ferritic steel, 430 stainless, *Al* alloying, oxidation kinetics, scale structure, oxide phases

1. INTRODUCTION

Scale formed in the steel making process is a result of sequential oxidation of the cast slab during continuous casting on air, furnace reheating in a combustion reheat atmosphere, and exposure of the hot transfer bar to air and water during hot rolling [1-6]. Prior studies on scale formation have identified the effects of different steel grades on the structure and properties of the formed scale. The major focus has been on commonly produced steel grades such as low to medium carbon steels [6], advanced high strength steel with high *Mn* and *Si* [7], as well as *Cr* alloyed ferritic [8-13] and *Cr-Ni* alloyed austenitic [14-16] stainless steels.

Extensive research has been conducted on the effect of extrinsic factors, such as temperature and furnace atmosphere on the type of scale structures formed [4, 6]. In the

case of stainless steels, understanding of scale formation is necessary for achievement of good surface quality for products which are employed in the nuclear industries, for solid oxide fuel cells, and welded automobile components [17] where surface quality is critical. Hence, surface cleanliness of stainless-steel using water jet descaling is very critical to achieving a quality surface for such applications. In some industrial processes, costly intermediate surface conditioning is used when the traditional high-pressure water descaling method does not adequately remove the scale layer.

From an industrial point of view, oxidation in reheating furnaces with combustion gas atmospheres could be the main problem since during this process, steel is exposed to extremely high temperature for relatively long times in a reactive oxidizing atmosphere containing water vapor. During reheating, the steel slab is held at temperatures of up to 1250-1300°C. Therefore, even high alloyed by *Cr* steel show intensive scale formation. A formed gradient of oxygen partial pressure results in multiphase scale structure. These complicated complex phenomena deviate real process oxidation kinetics from a classical described parabolic law according to Wagner theory [18].

Control of the oxide scale structure that forms on stainless steels in reheating furnaces having a combustion gas atmosphere is critical prior to descaling. . The characteristic of formed scale impacts its removal efficiency by water jet descaling. Residual scale may carry over into the subsequent hot rolling process. The studies listed in Table 1 revealed the effects of temperature, atmospheric conditions, and steel chemistries on scale formation on *Cr* and *Cr-Ni* alloyed stainless steels. Typical scale formed during reheating of ferritic steel consisted of four layers including an outer, intermediate, inner, and internal subsurface layer [19].

Additional alloying element, such as *Mn* and *Al* have been reported to have significant effect on the oxidation kinetics and scale structure in ferritic stainless steel. For example, it was shown that 1% *Mn* addition to a 19% *Cr-Nb* ferritic steel impairs the oxidation resistance of ferritic steel due to fast diffusion kinetics along grain boundaries that formed very fine Cr_2O_3 scale [20]. On the other hand, *Al* alloying of 13% *Cr Ti* stabilized ferritic stainless steels has been reported to improve its oxidation resistance due to the formation of internal Al_2O_3 thin film oxides which serve as a diffusion barrier during oxidation [21]. Alloying by *Al* is a very promising way to improve oxidation resistance of ferritic steels. However, most studies have focused on *Al* concentrations above 0.5 wt.%. Such *Al* concentrations are typically needed for the formation of a continuous Al_2O_3 protection film [22, 23].

Unfortunately, there were no specific investigations on how *Al* alloying affects scale formation on non-stabilized ferritic stainless steels during metallurgical processing. However, the authors [19] indicated that there is a potential that *Al* alloying could also significantly affect scale formation in ferritic stainless steels and such study could be interesting for industrial practice.

Table 1. Some reported studies on scale formation on stainless steels.

Study	Steel	Conditions	Publication
Oxidation kinetic mechanism	ferritic	1000 – 1150 ⁰ C, air	[24]
Scale formation	ferritic	1150 ⁰ C, water vapor	[19]
Effect of alloying elements	ferritic	800 – 1000 ⁰ C, air	[20-22, 25]
Effect of environment	ferritic and austenitic	1000 – 1150 ⁰ C, water vapor	[19, 26, 27]

The studies referred in Table 1 indicated that oxidation kinetics in *Cr*-alloyed ferritic steel deviated from typically observed kinetics during reheating carbon steels. The growth of an oxide film on pure iron and low alloyed steels during oxidation in reheating furnaces may be controlled by two main mechanisms: (i) mass transfer limited in starved gas atmosphere when oxidation is controlled by supply of gas, leading to a linear weight gain vs time relationship or (ii) controlled by solid state diffusion in the dense growing oxide layer, leading to a parabolic relationship. For a solid-state diffusion-controlled mechanism, the growth rate becomes limited by the diffusion resistance of growing oxide thickness with time and this mechanism provides a parabolic behavior. This behavior is predominant in oxides that form dense protective films and the required ratio of oxide/metal densities for forming a protective layer has been described as the Pilling-Bedworth ratio [28]. However, for real kinetics in a reheat furnace combustion atmosphere, the rate of scale growth may change during oxidation due to the formation of a multilayered scale structure and the development of internal defects (crack and lamination).

Changes in the oxidation mechanism may be initiated by detachment of the growing oxide structure from the metal substrate due to density difference and volume expansion caused by internal stress in the different forming oxide phases which promotes crack propagation. Crack propagation tends to short-circuit the diffusion path and breaks boundary layer for solid-state diffusion. Also, porosities due to vacancies defects at oxide/metal interface adds to the complexity of the rate controlling mechanism [29]. There have been reports on how the oxidation mechanism changes with gap formation during the oxidation of steels [30]; therefore, minor alloying elements could have

significant effect on oxidation of ferritic steel by influencing the formation of specific phases near metal/scale boundary. For these complicated kinetic conditions, a thermodynamic tool, which utilizes Gibbs free energy minimization, could be helpful to define the stability of formed oxide phases as a function of oxygen partial pressure [31,32] through the scale layer. The application of a thermodynamic tool utilizing the free energy minimization approach has been used in various steelmaking process with experimental reports supporting its reliability [32-39]. Such an approach was used to predict and experimentally verify the presence of phases such as Fe_2O_3 , Cr_2O_3 , and Fe_2SiO_4 in a ferritic stainless steel oxidized in a combustion gas atmosphere [40] and will be used in this study as supporting experimental method.

In this article, an experimental study of the oxidation kinetics under conditions which mimic industrial reheating processes was performed using a base and *Al alloyed* high *Cr* 430 ferritic stainless steel. Thermodynamic simulations and high-resolution metallographic techniques were used to bring to light the processes responsible for formation of difficult to remove oxides with deep penetration into the underlying metal matrix.

2. PROCEDURES

2.1. STEELS AND OXIDATION PARAMETERS

The composition of the industrially produced 430 ferritic alloyed by 16% *Cr* steels used for this work is described in Table 2. The samples were supplied by industrial sponsor in the form of transfer bars which had been subjected to primary and secondary

descaling during reverse hot rolling to the transfer bar thickness. The two steel chemistries which varied in *Al* content and were indicated as base and *Al* alloyed. Specimens for this study, 50 mm x 20 mm x 3.5 mm, were carefully machined from the near-surface region to the depth of 2-5 mm below the surface of the transfer bar to preserve surface microstructure. Machined samples were finished using wet grinding with 60 grit silicon carbide, the surface quality of the ground sample was measured to have Ra of 0.271 μm using 3D optical profiler (Nanovea, Model PS50 Micro Photonic Inc.). To prevent rusting prior to testing, sample surfaces were preserved by immersion in ethanol and air dried.

Table 2. Compositions of 430 steels used in this work (wt. %).

	<i>Cr</i>	<i>Al</i>	<i>C</i>	<i>Si</i>	<i>Cu</i>	<i>N</i>	<i>Ni</i>	<i>Mn</i>
Base	16	0.005	0.04	0.4	0.25	0.033	0.2	0.4
<i>Al</i> alloyed	16	0.210	0.04	0.5	0.25	0.024	0.2	0.4

To study the oxidation kinetics, thermo-gravimetric oxidation experiments were performed using a vertical $MoSi_2$ resistance-heating tube furnace (Model D900438 ATS Inc.). A high-purity external alumina tube with an internal diameter of 53 mm sealed from the bottom was used as reactor chamber. The top of the reaction tube was partially insulated with high temperature ceramic fiber tube cap leaving a center opening of 5 mm diameter just large enough to enable a 1 mm diameter wire to pass through it without touching the walls. This configuration was sufficient with the gas flowrates employed to prevent air ingress, refer to supplementary material. A +/-1 mg precision microbalance with a bottom hook which allowed specimens to be suspended in the furnace reaction

chamber on a nichrome wire was used to monitor the specimen weight. The specimen was suspended inside a catch basket to collect any spalled scale during oxidation. The atmosphere of the industrial reheating furnace was simulated in the lab by mixing gases in proportions that reproduced the natural gas combustion atmosphere in an industrial furnace (Table 3). The composition of gas mixture was controlled using a multi-channel mass flow control system and a controlled temperature of water vapor saturation system. Excess oxygen levels of 3% was chosen for the testing based on observed industrial reheat furnace operating conditions. Applied gas flow rate was 500 ml/min which provided 2 cm/sec gas velocity in reaction zone. Preliminary calculation showed absence of gas starvation in reaction zone. Oxidation temperature was monitored using a programmable furnace temperature controller which showed stability and at different setpoint from preliminary investigations. Upon completion of the oxidation experiment, the specimen was fast cooled to room temperature outside hot zone in a continuously flowing argon atmosphere to prevent further oxidation. Sample weights were recorded after oxidation, including the weight of any spalled scale in the catch basket.

Table 3. Industrial reheating conditions simulated in laboratory oxidation.

Combustion gas, vol. %	Temperature, °C	Time, min
8 CO_2 , 17 H_2O , 3 O_2 , N_2 bal.	1050, 1100, 1150, 1200, 1250	120

2.2. CHARACTERIZATION

A 3D optical profiler (Nanovea, Model PS50 Micro Photonic Inc.) was used to characterize topology and roughness of the as-formed scale surfaces. The samples were then mounted in epoxy, sectioned, ground using silicon carbide abrasive papers to 1200

grit and mechanically polished with 0.1 μm diamond paste applying controlling low pressure to prevent scale breakage as much as possible. The morphology, thickness, microstructure, and chemistry of the oxide layers were analyzed with a scanning electron microscope (SEM) using an TESCAN-ASCAT system equipped with Bruker energy dispersive spectroscopy (EDX). HORIBA Jobin-Yvon Raman spectroscopy (LabRam ARAMIS) was also used to identify the oxide phases that were present and compared to reported phases in RRUFF database [41].

For high resolution observation of the boundary between the subsurface scale layer and metal matrix, an area in the subsurface for the steel oxidized at 1150⁰C was selected and cut perpendicularly to oxide layer using the focused ion beam technique (SEM/FIB, Helios NanoLab 600, Thermo Fisher Scientific) and analyzed using transmission electron microscopy (TEM), operated at an acceleration voltage of 200 kV TEM (Tecnai F20, Thermo Fisher Scientific). Oxide phase present in the subsurface were identified using selected electron diffraction pattern analysis.

2.3. THERMODYNAMIC SIMULATION

FactSage 7.2 thermodynamic software [42] was used to simulate steel oxidation under the local equilibrium conditions. The data bases used included FSsteel, FToxid and FascaPS. The local equilibrium condition was examined by making stepwise oxygen additions into the simulated streams from previous step assuming irreversible reactions. This method allows us to predict different phases that form at low (inner layer) and high (outer layer) oxygen partial pressure levels. The thermodynamic simulations were performed assuming that the local equilibrium conditions were reached between gas

components, the formed oxide phases, and the steel. Preliminary simulations showed that for the studied thermodynamic conditions, oxygen was the predominant oxidant in the combustion gas. Using different oxygen/steel mass ratio, different oxide phases which form under the local equilibrium conditions during oxidation were predicted from low to high oxygen partial pressure levels and compared to the oxide phases reported from the experimental oxide phase identification. The temperatures used in the thermodynamic simulation was selected based on those used in the laboratory oxidation experiments.

3. RESULTS

3.1. EXPERIMENTAL OXIDATION KINETICS

Isothermal oxidation experiments were performed in a temperature range of 1050⁰C to 1250⁰C with 50⁰C step in a combustion gas atmosphere at 3% O_2 . Weight gain curves obtained from the isothermal heating which mimicked industrial furnace reheating conditions presented in Figure 1. The observed oxidation curves for both steels can be divided into three periods: (i) a nucleation stage where oxidation rate was very slow, (ii) period when increased weight gain has linear trend and, in some cases, (iii) followed by a period when oxidation switched to a parabolic rate. Significant dependence of nucleation time from test temperature was observed for both steel chemistries between 1050⁰C to 1150⁰C as shown in the Table 4. The overall oxidation rate was observed to be closely linear at the lowest temperature of 1050⁰C during whole oxidation time, nonlinear for 1100⁰C and 1150⁰C and approaching again a near linear behavior for 1200⁰C and 1250⁰C. The steel chemistry effect on studied oxidation parameters was observed in

different ways. The nucleation period was delayed in *Al* alloyed steel, while the base steel had an overall higher oxide growth rate in a temperature range of 1100°C - 1150°C (Figure 1).

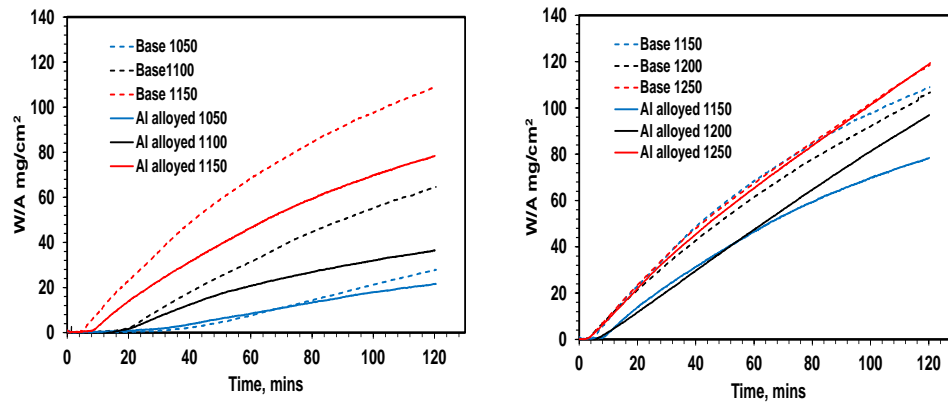


Figure 1. Oxidation kinetics of 430 stainless steel measured by TGA isothermal heating: (left) 1050°C – 1150°C and (right) 1200°C – 1250°C.

Table 4. Oxidation weight gain and reaction delay time (oxidation nucleation) for two studied 430 stainless steels.

Temperature, °C	Weight Gain (mg/cm ²)		Nucleation time (min)	
	Base	<i>Al</i> alloyed	Base	<i>Al</i> alloyed
1050	27.90	21.50	30	35
1100	64.61	36.50	18	21
1150	109.02	78.32	5	9
1200	106.67	96.80	3	7
1250	118.62	119.30	3	2

3.2. EFFECT OF STEEL CHEMISTRY ON SCALE STRUCTURE

The structure of the scale formed at different temperatures was examined in cross section. Experiments were performed at different temperatures between 1050°C and 1250°C. However, for brevity, only the effects of steel chemistry on structure and scale

composition at 1150⁰C for 2 hours of isothermal heating are reported here. The general scale structure consisted of four different scale layers which were observed in cross section for both steels: outer, intermediate, inner, and sublayer joined with metal matrix (Figure 2). The outer layer was characterized by a continuous structure with random micro and macro cracks and voids defect, the intermediate layer formed as a continuous structure just beneath the outer layer and the inner layer consisted on a mixed dense and porous scale structure. The subsurface layer which is of particular interest, consisted of fingerlike structures weaving down from the inner layer into to the metal matrix with micro porosity and voids at the metal/oxide boundary.

The measured scale thicknesses is reported in Table 5 for the various scale layers corresponding to the structural differences observed in both steels. The external scale layer of the base steel measured 465 μm , which was 15 μm less than that of the *Al* alloyed steel (450 μm). The intermediate/inner scale layer of the *Al* alloyed steel was 50 μm thinner than that of the base steel. The subsurface scale thickness of the base steel was almost twice (80 μm) that of the *Al* micro- alloyed steel (45 μm). Overall, the total scale thickness in the base steel measured 1015 μm while that of 915 μm in the *Al* alloyed steel. The differences observed in scale thickness were in accordance with the differences observed in the oxidation kinetics for the two steels.

Some other important differences were observed in the scale microstructure for the base and *Al* alloyed steels. The base steel exhibited high levels of porosity within the intermediate and inner scale layers. The porosity was predominant within the fingerlike scale structures that linked the intermediate to the inner scale layers. Also, porosity was observed between the inner scale layer and the subsurface layer which had a

superimposed fingerlike structured scale network on the metal matrix. The level of the porosity within the internal layer was reduced in the *Al* alloyed steel. Most importantly, from stand point of descaling efficiency, high porosity was seen near the subsurface of the base steel and this area was significantly more dense in the *Al* alloyed steel.

Similarities in chemistry and oxide phase composition were observed in external scale formed in both steels. However, there were detectable differences in their sublayer structure (Figure 2). The similar oxide phases identified by Raman spectroscopy in the outer and intermediate scale layers in the two steels (Table 6) consisted predominantly of hematite (Fe_2O_3) and chromia (Cr_2O_3). At the same time, these layers showed a decrease in *Cr* concentration from the intermediate to outer layer. The chemistry of the inner oxide layer for the *Al* alloyed steel showed a complex mixture of *Cr*-based oxide phases with trace of impurities of *Cu* and *Ni* as well as traces of *Al*. The oxide phases were identified as hematite (Fe_2O_3) and chromia (Cr_2O_3) while that for the base steel was predominantly chromia (Cr_2O_3).

Significant differences were observed in the chemistry of the subsurface layer in both steels using the SEM/EDX method. The subsurface oxide chemistry in the base steel showed a mixture of *Cr*, *Si* and *Fe*-based oxide with traces of *Al oxide*. The identified oxide phases in this scale layer were predominantly Cr_2O_3 , SiO_2 and $FeCr_2O_4$. In the *Al* alloyed steel, on the other hand, a strong presence of *Al* was detected in the subsurface scale, which consisted mainly of a *Cr*, *Si* and *Fe*-based oxide mixture. The presence of *AlN* inclusions was also observed just below the subsurface scale layer of the *Al* alloyed steel. These inclusions were detected in dark spots of internal oxide pocket growths at the ends of the fingerlike subsurface scale structures that extended into the metal matrix.

These fingers, which originated from interface shown in Figure 2, had a twisted geometry that masked some connections in the random 2D section. The oxide fingers were randomly scattered and separated from each other with some appearing to have been merged together during their formation. There was a significant difference in the thickness of this sublayer in the two alloys studied (Table. 5). The *Al* alloyed steel had a dense and shorted length of the subsurface finger structure (Figure 2b vs Figure 2d). However, the SEM resolution was insufficient to indentify phases in this fine submicron structure. Therefore, a high resolution TEM studies were performed on the two steels oxidized at 1150°C.

Table 5. Thickness of oxide layers in the different steel chemistries oxidized at 1150°C.

Layer	Scale thickness, μm	
	Base	<i>Al</i> alloyed
Outer	465	450
Intermediate/Inner	470	420
Subsurface	80	45
Total	1015	915

3.3. TRANSMISSION ELECTRON MICROSCOPY (TEM) OF SUBSURFACE SCALE STRUCTURE

The detailed structure of the subsurface layer was further investigated using the FIB/TEM technique on samples extracted directly from the subsurface region (near roots) of the fingerlike scale structure (Figure3). FIB sections were performed in a transverse plane parallel to oxidation front. Details of the technique are illustrated on Figure 3 and described in the methodology part of this article. A transverse cut of dimension 8 μm x 3 μm x 5 μm was performed at the tracked location. Prior to sectioning, a *Pt* coating was

sputtered onto the sample area to protect the oxide surface. The section was lifted out and mounted on to a transmission electron microscope (TEM) sample holder after which it was milled down from 3000 nm to less 200 nm by blasting the specimen surface with *Ga* ions for TEM analysis.

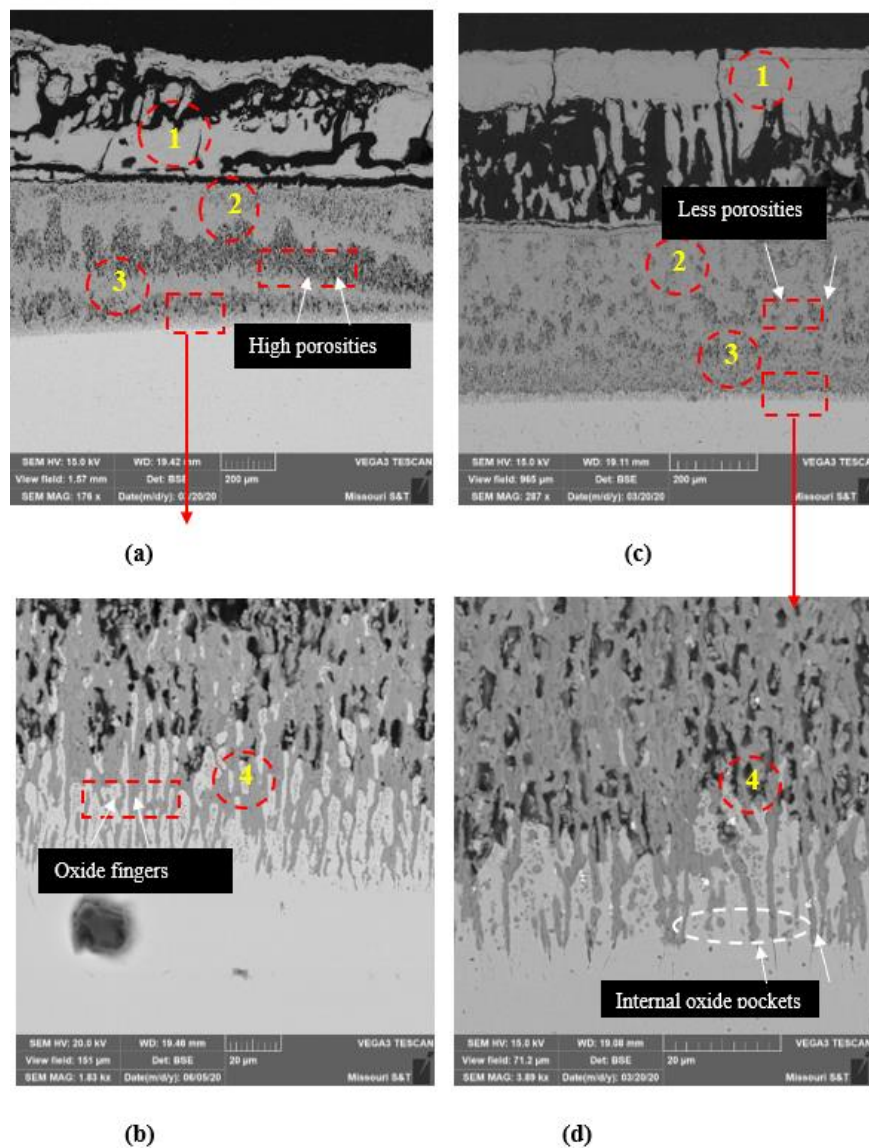


Figure 2. Cross-sectional BSE image of scale structure in 430 ferritic steels at 1150°C: left base (a-low magnification) and (b-high magnification) and right Al alloyed (c-low magnification) and (d-high magnification) steels. Number indicated formed scale layers: 1 – outer, 2 – intermediate, 3 – inner, and 4 – sublayer joined with metal matrix.

Table 6. Characterization of scale chemistry and oxide phases in 430 ferritic stainless steels and oxide thickness in the different scale layers.

Steel	Layer	Oxide Phases									(From Raman)
		<i>Fe</i>	<i>O</i>	<i>Si</i>	<i>Cr</i>	<i>N</i>	<i>Nb</i>	<i>Cu</i>	<i>Ni</i>	<i>Al</i>	
Base	Outer	76	24	-	-	-				-	Fe_2O_3
	Intermediate	78	20	-	2	-	-	-	-	-	Fe_2O_3, Cr_2O_3
		58	21	-	21	-	-	-	-	-	
		46	23	-	29	-	1	-	-	-	
	Inner	62	22	-	14	-	2	-	-	-	$Cr_2O_3,$
		77	19	-	4	-	-	-	-	-	
	Subsurface	39	22	1	38	-	-	-	-	-	$Cr_2O_3, SiO_2,$ $FeCr_2O_4$
		76	7	8	7	-	1	-	-	1	
		31	22	1	45	-	1	-	-	-	
		32	23	8	36	-	1	-	-	-	
56		25	13	6	-	-	-	-	-		
39	22	1	38	-	-	-	-	-			
Al low-alloyed	Outer	78	22	-		-	-	-	-	-	Fe_2O_3
	Intermediate	48	18	-	33	-	1	-	-	-	Fe_2O_3, Cr_2O_3
		79	17	-	4	-	-	-	-	-	
	Inner	84	4	5	5	-	-	2	-	-	Fe_2O_3, Cr_2O_3
		49	18	-	28	-	-	1	3	1	
		33	22	-	45	-	-	-	-	-	
		55	18	-	26	-	-	-	-	1	
	Subsurface	53	28	12	7	-	-	-	-	-	$FeCr_2O_4,$ Cr_2O_3, Fe_2SiO_4
		71	8	1	7	-	-	1	-	12	
		17	29	2	51	-	-	-	-	1	
48		23	17	8	-	-	-	-	4		
13		7	-	7	27	-	-	-	46		

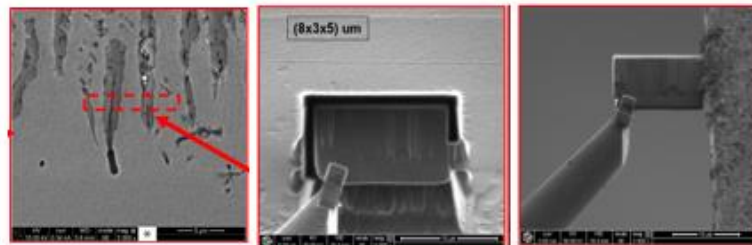


Figure 3. Subsurface location of FIB/TEM extracted specimen (base steel).

Analysis of the FIB extracted sample (base steel) in high resolution TEM revealed a system of oxide rings indicating internal structure of the oxide fingers penetrated into a metal matrix from scale/metal interface (Figure 4a). EDX analysis together with selected area electron diffraction (SAED) revealed different oxide phases present in this fingerlike structure (Figure 4 and Table 7). The oxide ring zone had 3-layer structure (S2, S3 and S4) distributed in *Fe-Cr* matrix (S1).

The phases in these zones were identified as: amorphous or nano-crystalline silica with small amount of *Al* in solution (core zone S4), crystalline chromia (Cr_2O_3) next to core in zone S3, and external chromite ($FeCr_2O_4$) ring (zone S2). layer, scanning transmission electron microscopy annular dark field imaging (STEM-ADF) with EDX were used to map out the elemental distribution of the various identified elements in the oxides phases and showed that impurity of *Nb* was also present in the $FeCr_2O_4$ layer (S2).

Table 7. EDX chemistry and oxide phases in cross-sectional subsurface scale structure in Base steel (Spectrum zones indicated in Figure 4).

Spectrum	Composition from EDX analysis, wt. %					Phases from electron diffraction
	<i>Fe</i>	<i>O</i>	<i>Cr</i>	<i>Si</i>	<i>Al</i>	
S1	96	-	4	-	-	Fe-Cr Matrix
S2	22	45	33	-	-	Chromite
S3	-	42	58	-	-	Chromia
S4	-	75	-	23	2	Silica + Al

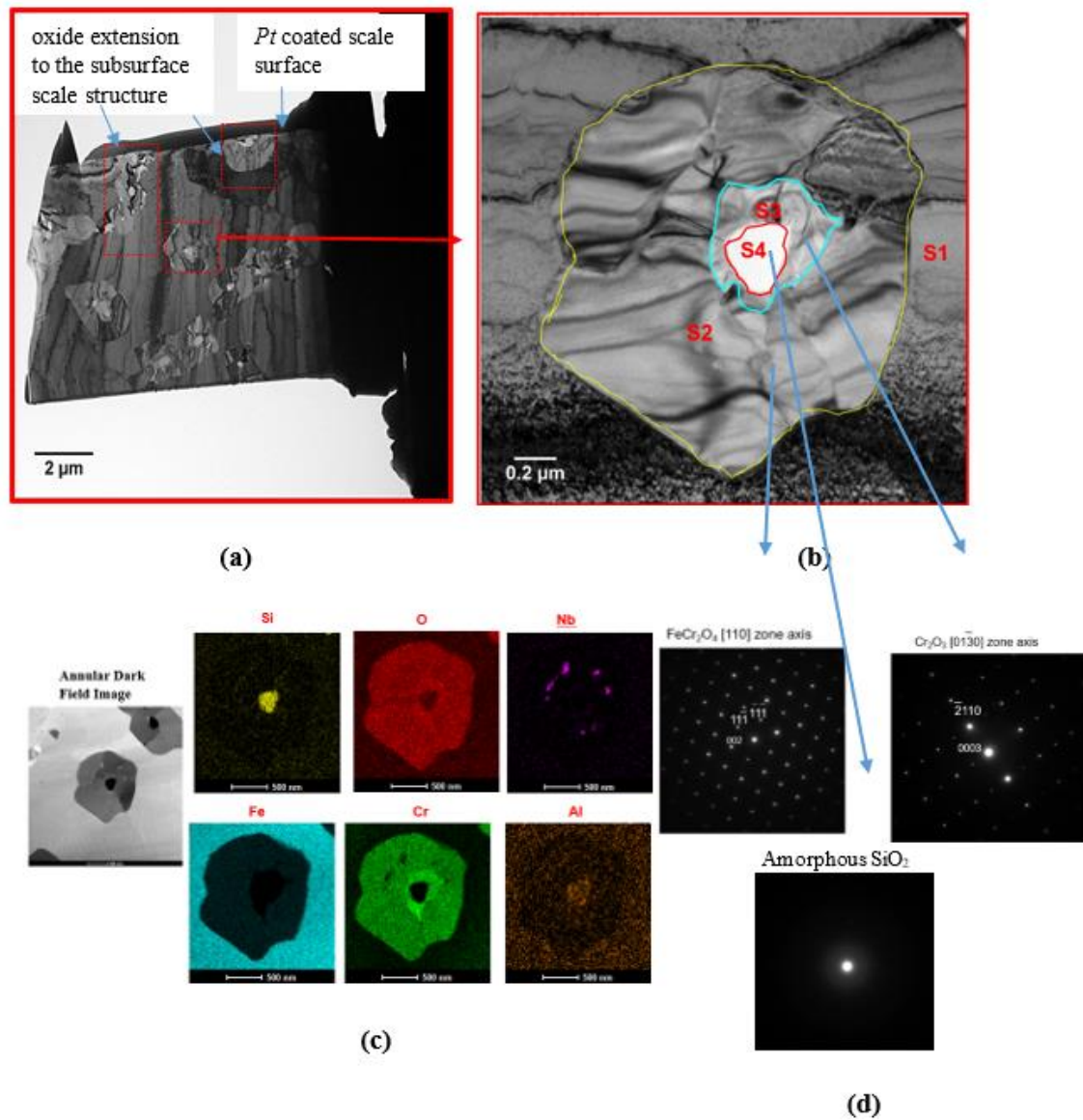


Figure 4. TEM cross-sectional structure of subsurface oxide scale with multiple oxide zones indicated by red dashed box (a), oxide zone with ring-like structure having different phases (b), elemental map showing distribution of elements in the oxide zone (c), and selected area electron diffraction (SAED) patterns (d).

The morphology of the oxide zones in the metal matrix of *Al* alloyed steel differed from the morphology observed in the base steel and consisted mostly of merged oxides with elongated core roots and some spots showing a perfect ring-type morphology

(Figure 5). Two oxide zones with different morphologies were selected for analysis (Figure 5b and Figure 5c). Some oxide zones exhibited multiple silica cores (Figure 5c). These oxide zones were identified from EDX chemistry analysis and TEM electron diffraction (Table 8). The silica cores (S2 in Figure 5b and S6 in Figure 5c) had amorphous structure with presence *Al* in solution. The next layer around elongated core (zones S7, S8 and S10 in Figure 5c) was chromia (Cr_2O_3) alloyed by *Mn* or chromite next to round core (zones S1, S3 and S5 in Figure 5b). The outer layer in all observed fingers was a chromite ($FeCr_2O_4$) without any trace of *Mn*. Elemental mapping of oxide zone revealed the distribution of the various elements (Figure 5d).

Table 8. EDX chemistry and oxide phase of cross-sectional subsurface scale structure of *Al* alloyed steel (zones from Figure 8).

Spectrum	Composition from EDX analysis, wt. %						Phases from electron diffraction
	<i>Fe</i>	<i>O</i>	<i>Cr</i>	<i>Si</i>	<i>Al</i>	<i>Mn</i>	
S1	24	41	33	-	-	2	Chromite+ <i>Mn</i>
S2	4	72	-	21	3	-	Silica + <i>Al</i>
S3, S5	23	44	33	-	-	-	Chromite
S4	100	-	-	-	-	-	<i>Fe</i> -BCC
S6	-	75	-	25	-	-	Silica
S7, S10	-	46	54	-	-	-	Chromia
S8	22	44	33	-	-	1	Chromia + <i>Mn</i>
S9	99	-	1	-	-	-	<i>Fe</i> -BCC
S11	23	47	30	-	-	-	Chromite

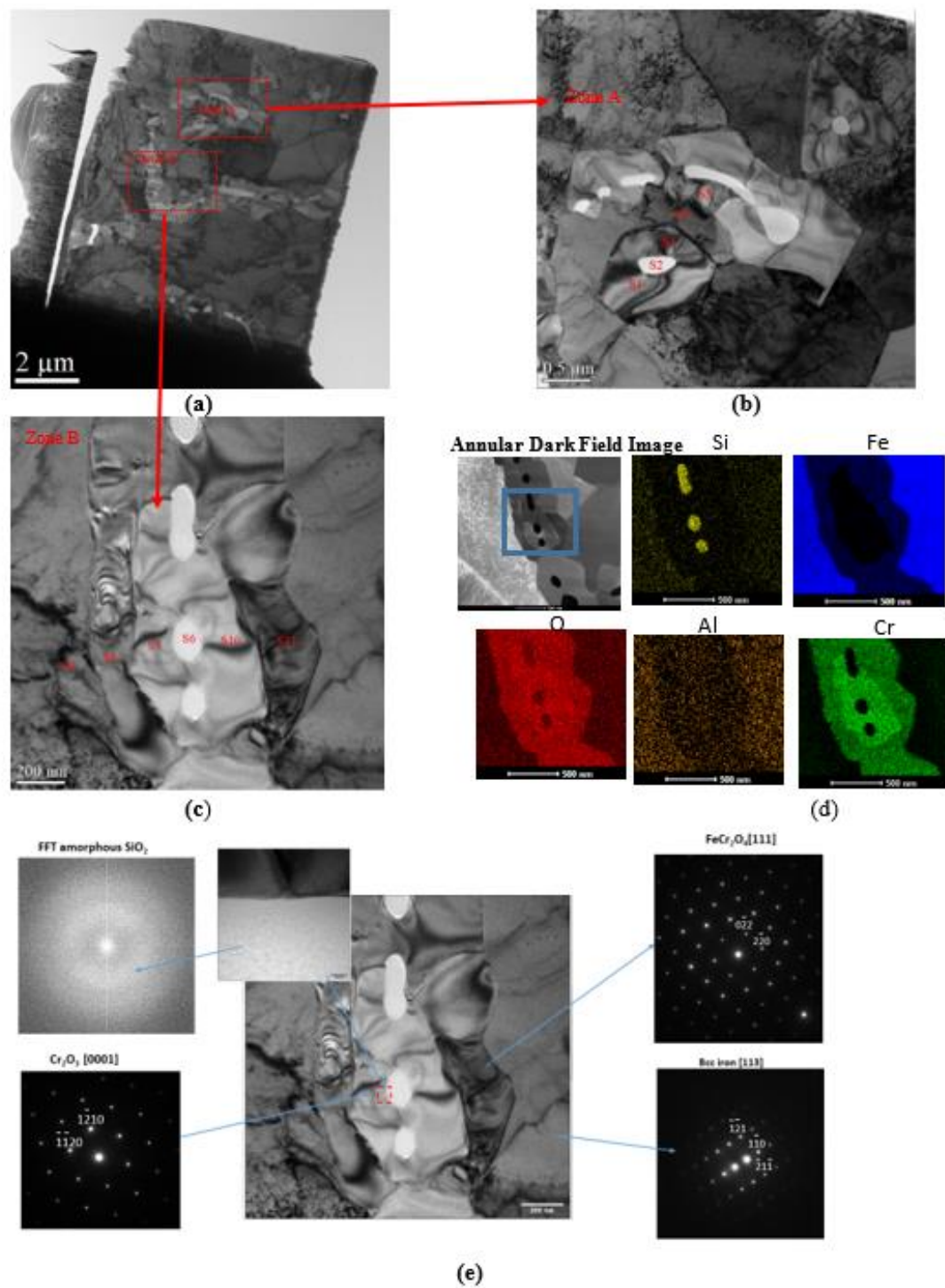


Figure 5. TEM Cross-sectional image of subsurface oxide scale in Al micro-alloyed steel with two zones (a), oxide zone with ring-like structure (b), oxide zone with rod-like structure (c) with elemental map of oxides (d) and phase identification using selected electron diffraction pattern (e).

4. DISCUSSION

4.1. THERMODYNAMIC ASSESSMENT ON THE EFFECT OF AL ALLOYING OF 430 STAINLESS STEEL ON SCALE STRUCTURE

Thermodynamics employing Gibbs free energy minimization under local equilibrium conditions was used to qualitatively predict oxide phases formed during combustion gas oxidation for 430 stainless steel. The thermodynamic approach used predicted oxide phases formed at low to high oxygen partial pressures which mimic experimental condition of local oxygen equilibrium between different scale layers. Simulations were performed for the base (Figure 6a) and *Al* alloyed (Figure 6b) 430 ferritic steel at 1150°C. Thermodynamic simulations predicted similarity of phases which could be formed in outer, intermediate, and inner layers in scale in both studied alloys at different temperatures. These layers for the effect of chemistry, thermodynamic prediction of oxide phases was similar for oxide layers in the outer, intermediate, and inner phases, predicting the formation of Fe_2O_3 , Cr_2O_3 , SiO_2 , Fe_2SiO_4 and $Mn_2Al_4Si_5O_{18}$. Chromium depletion between these layers promoted formation of mixture of pure iron oxides with chromium oxides in outer layer and richer in *Cr* as well as *Si-Mn-Cr* oxides in underlying intermediate and inner layers. Predicted oxide phases in scale were in good agreement with experimental oxide phase distribution (Table 9). However, thermodynamic simulations predicted significant difference in oxide phases formed in the sub-surfaces of the two steels at low oxygen partial pressures. In the case of *Al* alloyed steel, AlN , Al_2O_3 and SiO_2 were predicted in the subsurface at relatively lower partial pressures of oxygen compared to the base steel, having predominantly complex *Mn-Al-Si* oxides and pure SiO_2 and Cr_2O_3 oxides. The thermodynamic simulations generally agreed

well with the observed effects of steel chemistry and temperature on multi-layered scale structure. However, some differences were observed between the predicted thermodynamic oxide phase formation and the experimental results (Table 9), which may be due to the assumptions used in the thermodynamic simulation.

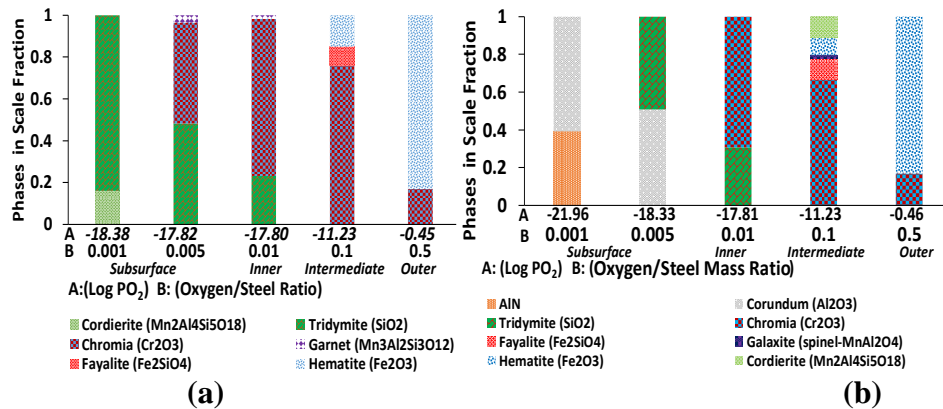


Figure 6. Thermodynamic prediction of stable oxide phases formed during oxidation 430-ferritic stainless steel at different oxygen partial pressures at 1150°C: (a) base and (b) Al alloyed 430 ferritic steels.

Table 9. Experimental vs. thermodynamic predictions of oxide phases in scale layers.

Steel	Phases present in oxide scale layers				
	Condition	Outer	Intermediate	Inner	Subsurface
Base	Experimental at 1150°C	Fe_2O_3	Cr_2O_3 , Fe_2O_3	Cr_2O_3	Cr_2O_3 , SiO_2 , $FeCr_2O_4$
	Simulated 1150°C	Fe_2O_3 , Cr_2O_3	Fe_2O_3 , Cr_2O_3 , Fe_2SiO_4	SiO_2 , $Mn_3Al_2Si_3O_{12}$, Cr_2O_3	$Mn_2Al_4Si_5O_{18}$, SiO_2 , $Mn_3Al_2Si_3O_{12}$, Cr_2O_3
Al micro-alloyed	Experimental at 1150°C	Fe_2O_3	Cr_2O_3 , Fe_2O_3	Cr_2O_3 , Fe_2O_3	$FeCr_2O_4$, Cr_2O_3 , Fe_2SiO_4
	Simulated 1150°C	Fe_2O_3 , Cr_2O_3	Fe_2O_3 , Cr_2O_3 , Fe_2SiO_4 , $MnAl_2O_4$, $Mn_2Al_4Si_5O_{18}$	SiO_2 , Cr_2O_3	SiO_2 , Al_2O_3 , AlN

***Bold phase: differences observed between base and Al micro-alloyed steel**

4.2. MIXED CONTROL OXIDATION KINETICS MODELLING

The non-uniform shape of kinetic curves observed in the experimental weight gain plots indicates that the kinetics of oxidation may be under mixed control. Therefore, a model with linear and parabolic terms was used to determine the best fit for the rate constants using the least squares error minimization tool in Excel:

$$W = k_l(t-a) + k_p(t-a)^n \quad (1)$$

where: W is the weight gain per area (mg/cm^2), k_l is the linear rate constant ($\text{mg}/\text{cm}^2\text{min}$), k_p is the parabolic rate constant ($\text{mg}/\text{cm}^2\text{min}^{0.5}$), n is the exponential factor ($n = 0.5$ for parabolic rate), t is the oxidation time in minutes, and a is the incubation time for the onset of oxidation.

The weight gain curves were fitted to the experimental TGA results (Figure 7). Table 10 shows the calculated rate constants (linear and parabolic) extracted from the kinetic model using Eq. (1). The results obtained for the various rates were comparable to values reported in literature for the similar steels oxidized under similar atmosphere and temperature ranges [6]. Using the extracted parabolic rate constants, the temperature dependence of the linear and parabolic rate constants was plotted using the Arrhenius Eq. 2 and the activation energies were extracted for the two studied steels (Figure 8).

$$\ln(k) = \ln(k_0) - Q/RT \quad (2)$$

where: k is the oxidation rate constant, k_0 is a constant having same dimension as the oxidation rate constant, Q is the activation energy of the oxidation reaction, R is the universal gas constant and T is the absolute temperature.

For solid state diffusion control, the rate constants were assessed for both steels. The value of activation energy was different for the two studied steels. The base steel

exhibited activation energies of 87 kJ/mol and 317 kJ/mol, for the linear and parabolic rate constants, respectively. The *Al* alloyed steel exhibited higher value for both the linear (103 kJ/mol) and parabolic (416 kJ/mol) rate constants. The low activation energy for the linear rate constant is consistent with that of gas phase mass transport or gas phase diffusion control, while the higher activation energies for the parabolic rate constant are consistent with values for solid state diffusion through an oxide layer, close to values, reported for anion (O) [43,44] and bulk [45] diffusion in Cr_2O_3 . The presented activation energy was calculated for a temperature range between (1050°C to 1150°C) because kinetic constants at the upper temperature ranges above 1200°C showed unrealistic values. This may be related to a change from diffusion-controlled oxidation kinetics to a more complicated mechanism related to defect formation in the scale or possible chromium vaporization in combustion gas containing water vapor [46].

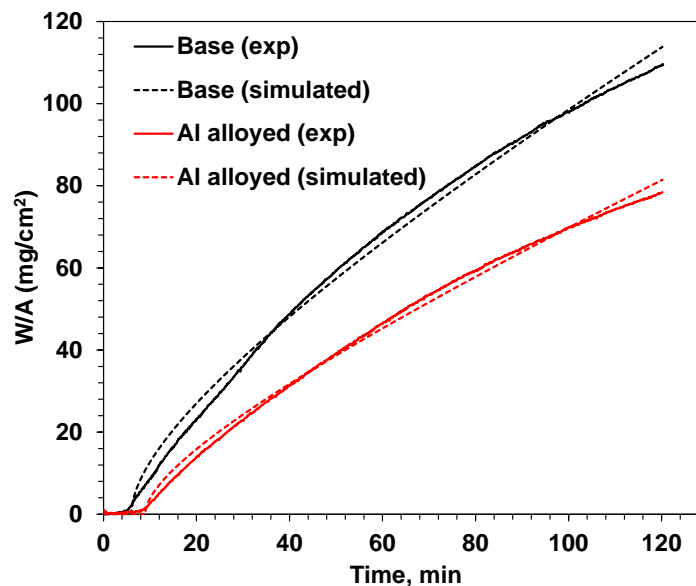


Figure 7. Oxidation kinetic of base and *Al* micro-alloyed 430 stainless steels: dashed (modelled) results) and continuous (experimental) curves at 1150°C.

Table 10. Oxidation Rate Constants and Activation Energies for a Mixed Control Kinetic Mechanism at Different Temperatures for studied 430 Stainless Steels.

Temperature, °C	Base		Al micro-alloyed	
	k_l ($g\ cm^{-2}\ s^{-1}$)	k_p ($g^2\ cm^{-4}\ s^{-1}$)	k_l ($g\ cm^{-2}\ s^{-1}$)	k_p ($g^2\ cm^{-4}\ s^{-1}$)
1050	4.95×10^{-6}	*	3.50×10^{-6}	4.05×10^{-6}
1100	7.90×10^{-6}	3.14×10^{-5}	3.60×10^{-6}	2.58×10^{-5}
1150	8.60×10^{-6}	8.90×10^{-5}	6.80×10^{-6}	5.72×10^{-5}
1200	1.00×10^{-5}	5.55×10^{-5}	1.30×10^{-5}	1.26×10^{-5}
1250	1.20×10^{-5}	5.99×10^{-5}	1.40×10^{-5}	3.50×10^{-5}
Q (kJ mol ⁻¹) 1050°C – 1150°C	87	388	103	416

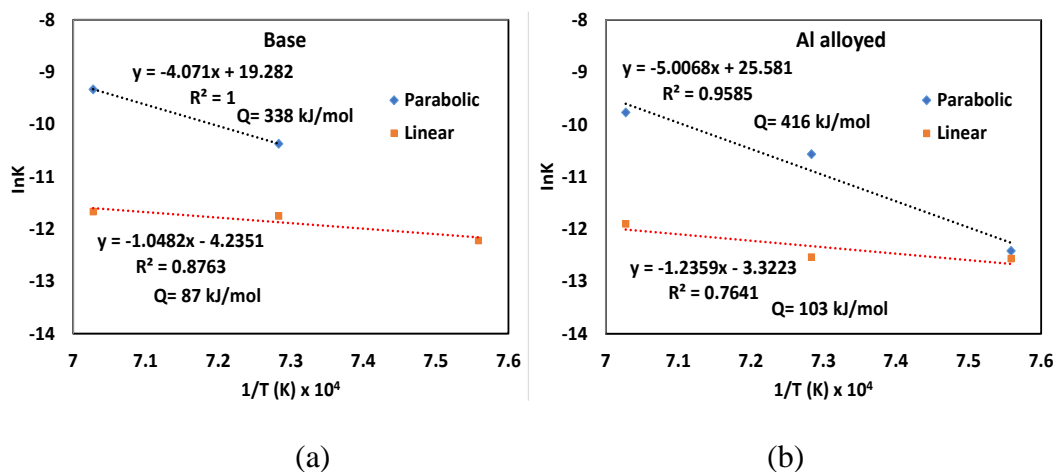


Figure 8. Dependence of rate constant on temperature for oxidation assuming a mixed control kinetics: (a) base and (b) *Al alloyed* 430 stainless steels.

4.3. EFFECT OF TEMPERATURE ON SCALE STRUCTURE TRANSFORMATION

The oxidation kinetics suggest several possible rate controlling mechanisms for oxidation during reheating 430 *Cr*-alloyed ferritic stainless steel a change in mechanisms with temperature (1050°C to 1250°C) for two hours oxidation that could be related to changes in formed scale structure. The experimentally observed scale structure exhibited different layers which were classified into outer, intermediate, inner, and subsurface

layers as illustrated on Figure 2 for a typical industrial reheating temperature of 1150 °C. However, changes in the oxidation conditions from low (1050°C) to medium (1150°C) and high (1250°C) temperatures resulted in significant transformations in the scale structure (Figure 9). At the lower temperature studied, a continuous Cr_2O_3 layer of about 10 μm was formed on the metal surface together with periodic oxide nodules. This continuous layer with fine grains formed by internal oxidation tend to passivate the metal substrate to suppress rapid scale growth which is typical for high *Cr*-alloyed steels at moderate oxidation conditions. However, atmospheres containing steam or water vapor having higher solubility of oxygen in the alloy tend to see accelerated internal oxidation leading to a disruption of Cr_2O_3 layer, a phenomenon known as breakaway oxidation due to water vapor effect on the solubility of the oxygen in the alloy [9]. Localized oxide scale nodule growth, above 300 μm in thickness, were observed periodically. These fast-growing scale nodules were formed due to fractures in the continuous oxide film which occurs as a result of the depletion of *Cr* at these sites. Water vapor in the oxidizing atmosphere has been reported to accelerate fracturing of the continuous oxide protection layer at relatively low oxidation temperatures [9]. Therefore, such changes in scale topology could affect oxidation rate: slow rate at initial period and acceleration when this protection layer is broken, and nodules starts to develop.

At intermediate temperatures (1100°C and 1150°C), the continuous dense chromia protection film transformed into various oxide layers (Figure 9). The external, intermediate, and inner layers were characterized by voids and lateral cracks at a direction parallel to the metal matrix boundary. The mechanism of porosity and micro-crack formation was attributed to internal tensile stresses generated in the forming oxide

layer [6,47] and possible chrome oxide and hydroxide vaporization [9]. Higher magnification examinations of the internal scale layer revealed a high level of porosity with macroscopic and microscopic cracks in the scale structure, which is known to allow gas phase diffusion to occur through such micro-defects.

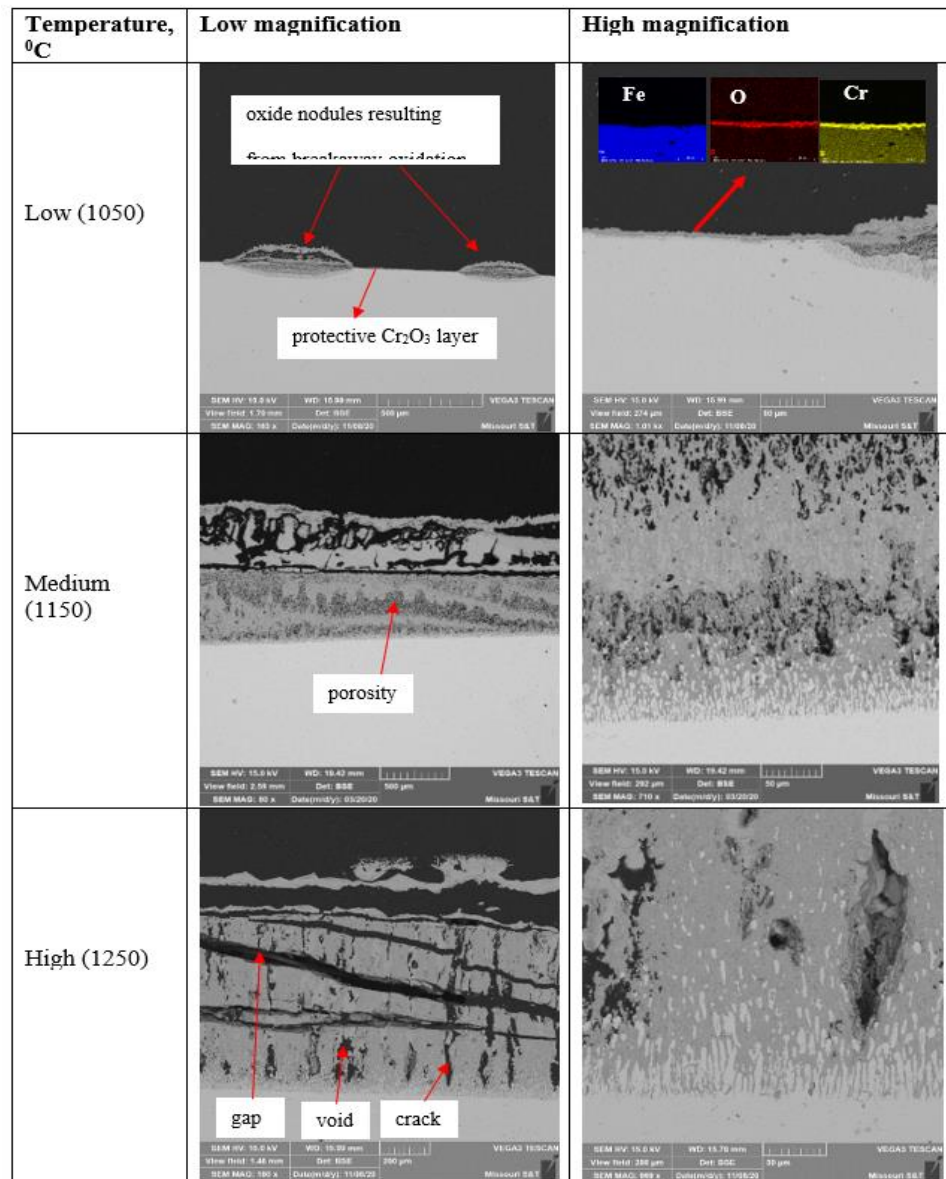


Figure 9. Cross-sectional SEM BSE image of scale structure transformation in base 430 ferritic stainless steel at different telepictures during oxidation in combustion gas atmosphere for 2 hours.

At high temperatures (1200°C to 1250°C), there was a significant development of macro-defects in scale. Extensive detachment of scale from the matrix was observed during experiment with transverse cracks, large voids and gaps formed throughout the entire scale structure (Figure 9). A higher magnification examination of the internal surface layer indicated high levels of porosity, and microscopic and macroscopic cracks. The formation of gaps and vertical cracks in the scale structure favors and accelerates gas and solid phase mass transport mechanism as oxidizing species transport faster through the defects formed in the growing oxide layer leading to short-circuits of diffusion path (Figure 10). Also, scale detachment created sudden changes in the oxidation rate. Such a scale detachment mechanism was observed during experimental investigation in the form of a spike in oxidation curve related to drop mass of scale in basket followed by the exposure of barrel surface (Figure 10). This behavior increases the oxidation rate shown in this figure by the dashed lines. It is interesting to note that the previously described temperature dependence of the oxidation rates showed a somewhat lower activation energy for the base steel, and that also the spikes on TGA curves were observed mostly on the base steel at higher test temperatures.

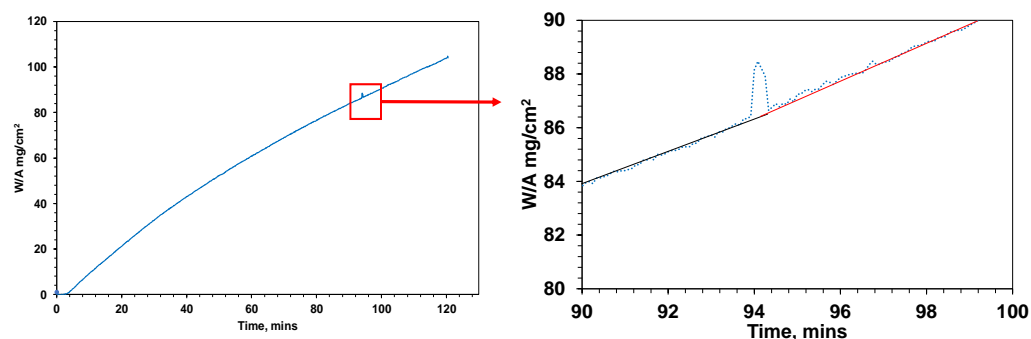


Figure 10. Sudden change in oxidation rate resulted scale cracking and spalling at high temperature (base steel, 1200°C).

4.4. EFFECT OF AL ALLOYING ON SUBSURFACE SCALE STRUCTURE

Oxidation weights gain kinetic plots (Figure 1) indicated that *Al* alloyed steel exhibited lower overall scale growth rate with longer incubation time at the onset of oxidation when compared to the base steel. This effect is more prominent at lower and medium oxidation temperature (Figure 11). Structural analysis of the *Al* alloyed steel indicated that a much dense internal scale layer near steel surface was developed. This effect was more significant at low and medium test temperatures. However, most significant changes were observed in structure and phases of formed sublayer with penetration into metal matrix. These changes were also predicted by thermodynamic simulations (Figure 6 and Table 9).

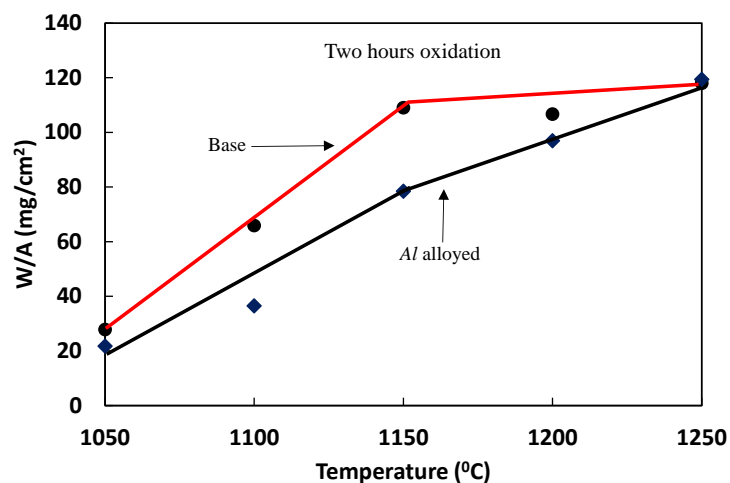


Figure 11. Temperature dependence of scale growth for base and *Al* alloyed ferritic steels.

The *Al* alloy steel exhibited a complex *Al* containing amorphous silica core inside of the chrome oxide fingers with deep penetration into the metal matrix. It is well documented that presence of high *Al* levels in stainless steel have a significant effect on

its oxidation resistance through the formation of a protective Al_2O_3 layer on metal/scale interface [21]. However, the Al levels in the alloyed 430 discussed here is not high enough to develop such continuous protection level. The TEM studies presented here suggest that the slowing of the oxidation rate in low Al alloyed 430 stainless steel takes place due to changes in the structure of subsurface layer during high temperature preheating in the presence of Al . This subsurface layer is typically not observed at lower temperature (below 1050°C); however, it plays significant role during higher industrial reheating temperatures. A significant difference in oxide morphology of the subsurface scale of the two studied steels were observed under TEM.

In both cases, fingerlike oxides were penetrated into metal matrix (Figure 2). These fingers had cores with amorphous structure covered by crystalline chromia. It appears that the penetration of these fingers into a ferrite matrix are related to fine grain boundaries developed during oxidation. Figure 12 illustrates 1-2 micron-sized fine ferrite grains surrounding oxides fingers. This mechanism of subsurface grain refinement could be related to recrystallization during the BCC to FCC transformation, resulting in local Cr depletion. Figure 4 and Table 7 indicate that the Cr concentration in the matrix surrounding oxide fingers decreased significantly and this change in Cr will promote BCC to FCC transformation at reheating temperature in near surface region (Figure 13).

Analysis of the cores in fingerlike structure revealed the presence of Al which had doped the amorphous silica core and Al alloying showed a higher doping level (Table 7 and 8). Studies have been conducted on the doping of silica with Al in ceramic systems and have revealed that small levels in Al doping decreased oxygen permeability by up to two orders of magnitude by inhibiting interstitial and network diffusion of oxygen [48].

With the subsurface oxide phases formed at very low oxygen partial pressures and the first layers to form during oxidation, the presence of *Al* could have decreased the permeability of oxygen through the more permeable amorphous silica when compared to the other oxides formed in scale. This *Al* effect might lead to a deceleration of growth kinetics. Experimental observation showed (Table 5) nearly a 2X thinner subsurface layer formed in *Al* alloyed steel.

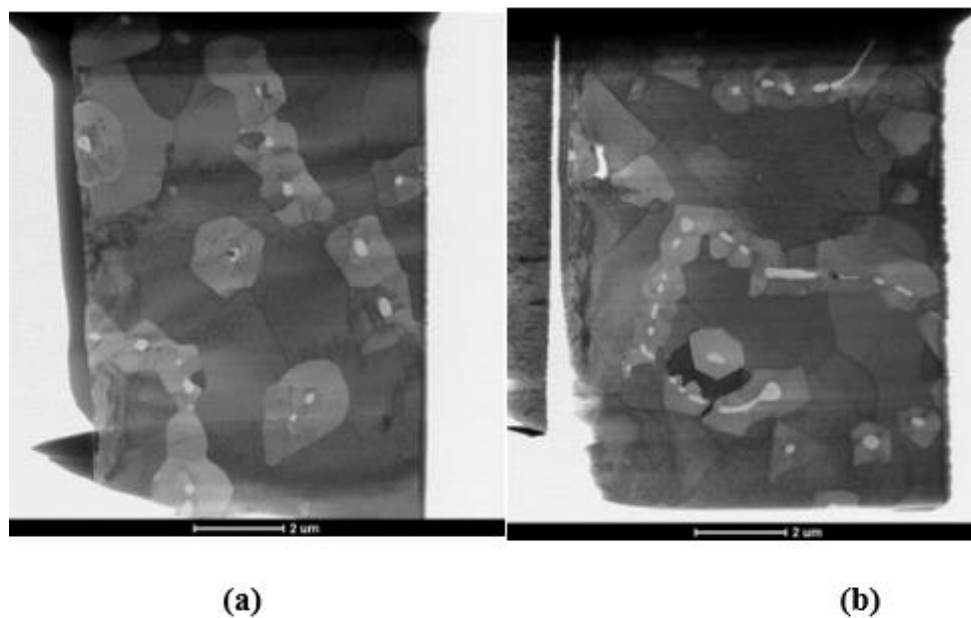


Figure 12. Scanning Transmission Electron Microscopy (STEM) image of cross-sectional subsurface scale structure, a) base steel and b) *Al* alloyed steel.

Finally, all observations and proposed mechanisms discussed in this article on the influence of *Al* alloying on oxidation processes in reheated 430 ferritic steel are depicted schematically in Figure 14. It is evident that, at the various temperatures, the external scale (outer and intermediate) structures formed did not exhibit significant difference for

both the base and the *Al* alloyed steel since these layers both contained similar defects. However, the subsurface scale layers exhibited a significance difference in structure and defects formation. The *Al* alloyed steel saw less defects and thinner scale layer at 1150°C with the difference almost similar at extreme temperature (1250°C).

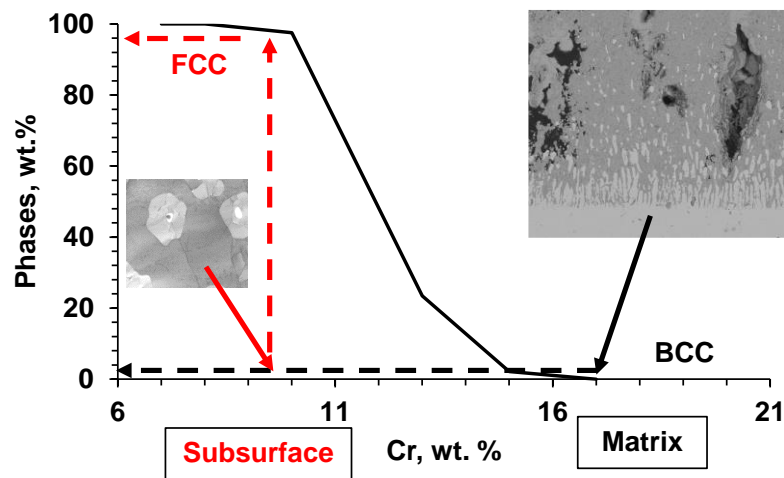


Figure 13. Equilibrium of BCC/FCC transformation in *Fe-Cr* system at 1150°C considering effect of other alloying elements in 430 steel (FACTSAGE software).

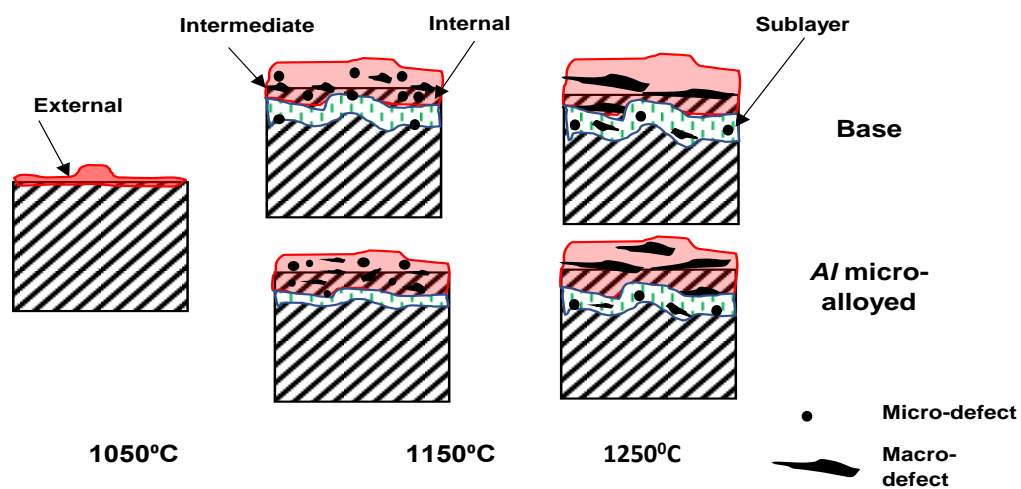


Figure 14. Schematic representation of oxidation processes during reheating base and *Al* microalloyed 430 ferritic steels.

5. CONCLUSION

The effect of *Al* alloying on oxidation kinetics and scale formation on 430 ferritic stainless steel were investigated. The kinetic assessment of the two steels studies indicated a mixed controlled mechanism for the oxidation kinetics with evidence of changing kinetics throughout the oxidation time period. The *Al* alloyed steel exhibited a longer incubation period at the onset of oxidation which was reflected in its lower oxidation rate with higher activation energy compared to the base steel indicating possible growth limitations in the *Al* alloyed steel. The kinetic difference in oxidation rate observed was reflected in the structural morphology, oxide phases and chemistry differences in the two steels, particularly in the subsurface layer which had fingerlike structures with deep penetration into the metal matrix. The *Al* alloyed steel exhibited a reduced subsurface oxide layer thickness of 45 micron, which was about half of that observed in the base steel (80 micron), with a complex chemistry and oxide phases of mixed *Fe-Cr-Al* based oxides. Thermodynamic modeling predicted the possible formation of *AlN* and oxidation resistant Al_2O_3 at low oxygen partial pressure during nucleation stage of oxidation even though the *Al* alloyed steel did not have sufficient *Al* for the formation of an oxidation resistant layer.

Further investigation into the penetrating subsurface layer of the two steels using high resolution TEM studies revealed other possible mechanisms for the low oxidation rate and limited scale growth in the *Al* alloyed steel. TEM results identified a ring-type oxide morphology with amorphous silica core in the penetrating subsurface layer for the base steel with mixed morphology of elongated core root and ring-type oxide structure

embedded in the metal matrix for the Al alloyed steel. The mechanism suggests that doping of the amorphous silica core by Al decreased oxygen permeability by inhibiting interstitial and network diffusion of oxygen, leading to a deceleration in growth kinetics observed in the Al alloyed steel due to its higher doping in the subsurface nanostructure.

ACKNOWLEDGEMENTS

This study is supported by Kent Peaslee Steel Manufacturing Research Center, and the authors express their appreciation to partner industrial members of this project for supplying material for this study. The authors wish to gratefully acknowledge the help of Dr. Wei Ting of Materials Research and Characterization Department, Missouri S&T for his help with TEM studies and phase identification of crystal structures.

SUPPLEMENTARY MATERIAL

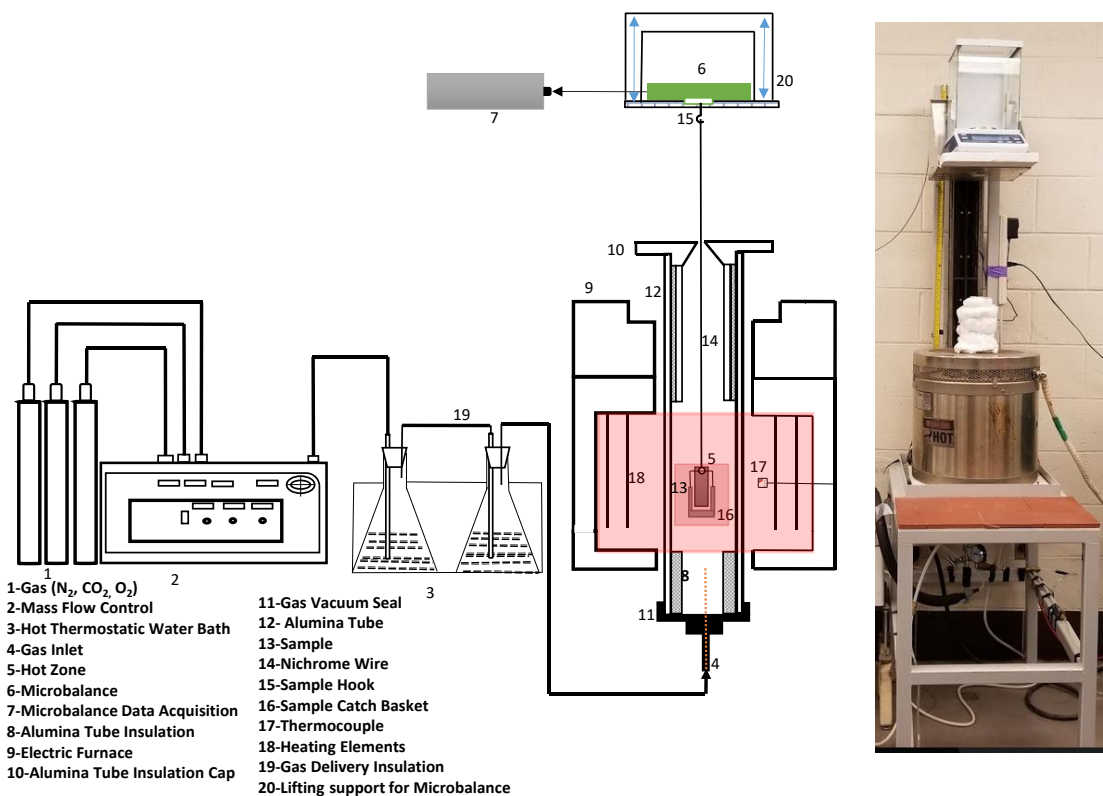


Figure S-.1 Schematics of TGA setup showing gas flow direction and reaction tube top insulation.

REFERENCES

- [1] J.S. Sheasby, W.E. Boggs and E.T. Turkdogan: *Met. Sci.*, 1984 Vol. 18, pp. 127-136.
- [2] W. Sun: *PhD thesis*, 2005, School of Mechanical, Materials and Mechatronic Engineering, University of Wollongong.
- [3] O. A. Zambrano, J.J. Coronado, and S. A. Rodriguez: *Surface and coating technology*, 2015, Vol. 282, pp. 155-162
- [4] H.T. Abuluwefa, R.L.L. Guthrie and F. Ajersch: *Oxidation of Metals*, 1996, Vol. 46, pp. 423-440.
- [5] W. E. Boggs: *Metallurgical society of AIME*, 1973, pp. 84-128.
- [6] H.T. Abuluwefa, R.L.L Guthrie and F Ajersch: *Met Trans A*, 1997, Vol. 28A, pp. 1633-1641
- [7] R. Sohn, J-S. Kim, and S. Sridhar: *ISIJ International*, 2015, Vol. 55, No. 9, pp. 2008-2017
- [8] H. Asteman, J.-E Svensson and L. -G Johansson, *Oxidation of Metals*, 2002, Vol. 57, No. 3-4, pp. 193-216
- [9] E. Essuman, G.H. Meier, J. Zurek, M. Hansel, L. Singheiser and W. J. Quadackers, *Scripta Materialia*, Vol. 57, pp. 845-848
- [10] M.P. Brady, Y. Yamamoto, M. L. Santella and B.A. Pint: *Scripta Materialia*, 2007, Vol. 57, pp. 1117-1120.
- [11] H. Laukka, E-P. Heikkinen and T. Fabritius, *Steel Research Int.*, 2018, 11p.
- [12] N. Otsuka, Y. Nishiyama and T. Kudo, *Oxidation of Metals*, 2004, Vol. 62, No. 1-2, pp. 121-139
- [13] J.C. Bavay and P. Bourgain, *Materials Science and Engineering*, 1987, Vol. 89, pp. 137-143
- [14] M. P. Brady, Y. Yamamoto, Z.P. Lu, C.T. Liu, P.J. Maziasz and B.A. Pint, *United States Patent Disclosure*, 2010, 12 pp.
- [15] Y. Zhang, A. Shi, P. Liang, J. Meng, H. Zhang, C. Zhang, Z. Zhang, and P. Han, *Steel Research Int.*, 2018, Vol. 89, 7 pp.

- [16] X. Cheng, Z. Jiang, D. Wei, J. Zhao, B.J. Monaghan, R.J. Longtottom and L. Jiang, *Surface, and Coatings Technology*, 2014, Vol. 258, pp. 257-267
- [17] Z. Oksuita, P. Olier, Y. de Carlan and N. Baluc, *Journal of Nuclear Material*, 2009, Vol. 393, pp. 114-119
- [18] C. Wagner, *J. Electrochem. Soc.*, 1952, Vol. 99, pp. 369-380
- [19] R. Osei, S. N. Lekakh, and R. J. O'Malley, *AISTech Proceedings*, 2020, pp. 1126-1137
- [20] Y. Inoue, N. Hiraide, A. Hayashi, and K Ushioda, *ISIJ International*, 2018, Vol. 58, No. 10, pp. 1850-1859
- [21] P. Becquerelle, M. Hubert, B. Savage, J.C. Bavay, and P. Bourgain, *Materials Science and Engineering*, 1987, Vol. 87, pp.137-143
- [22] Z.G. Zhang, F. Gesmundo, P. Y. Hou, and . Nui, *Corrosion Science*, 2006, Vol. 48, pp. 741-765
- [23] G. Wang, D.L. Douglass, and F. Gesmundo, *Oxidation of Metals*, 1991, Vol. 35, Nos. 3/4 , pp. 279-294
- [24] H. E. Evans, A. T. Donaldson, and T. C. Gilmour, *Oxid Met*, 1999, Vol. 52, No. 516, pp. 379-402
- [25] V. Badin, E. Diamanti, P. Foret, and E. Darque-Ceretti, *Procedia Materials Science*, 2015 Vol. 9. pp. 48-53
- [26] V. Badin, E. Diamanti, P. Foret, and E. Darque-Ceretti, *Oxid Met*, 2014, Vol 82, pp. 347-357
- [27] X. Cheng, Z. Jiang, D. Wei, J. Zhao, B. J. Monaghan, R. J. Longbottom, and L. Jiang, *Surface coating Technology*, 2014, Vol. 258, pp. 257-267
- [28] C. Xu and W. Gao, *Material Research Innovations*, 2000, Vol. 3, pp. 231-253
- [29] W. Kast, and C.-R. Hohenthanner, *Int. J. Heat Mass Transfer*, 2000, Vol. 43. Pp. 807-823
- [30] H. F. Marston, P. H Bolt, G. Leprince, M. Roder, R. Klima, J. Niska and M. Jarl, *Iron and steel making*, 2004, Vol. 31, No. 1, pp. 57-65
- [31] J. Shan, X. Guo, and Y. Nui, *Oxid Met*, 2019, Vol. 92, pp. 195-225

- [32] J. M. Alinger, H. Cao and S. V. Dheeradhada: *Journal of Power Sources*, 2011, Vol. 196, pp. 1975-1982.
- [33] I.-H Jung: Overview of the applications of thermodynamic databases to steelmaking processes: *Calphad*, Vol. 34, is. 3, pg. 332-362, 2010.
- [34] S. N. Lekakh, J. Ge, V. Richards, R. O'Malley, and R. J. Terbush: *Met Trans B*, 2017, Vol. 48B, pp. 406-417.
- [35] C.W. Bale, E. Bélisle, P. Chartrand, S.A. Degterov, G. Eriksson, A.E. Gheribi, K. Hack, I.-H. Jung, Y.-B. Kang, J. Melançon, A.D. Pelton, S. Petersen, C. Robelin, J. Sangster, P. Spencer, and M.-A. Van Ende: *Calphad*, 2016, Vol. 54, pp. 35-53.
- [36] K. Young-Bae, D.K Sazol, H. Taekwon and J In-Ho: *Acta Materialia*: 2014, Vol. 71, pp. 164-175.
- [37] L. Holappa, H. Hamalainen, N. Liukkonen and M. Lind: *Iron and Steelmaking*: 2003, Vol. 30, pp. 111-115.
- [38] P. Joo-Hyun, L. Sang-Beom and R.G Henri: *Met Trans B*, 2008, Vol. 39B, pp. 853-861.
- [39] P.C Pistorius, Y. Ren, and L. Zhang: *Met Trans B*, 2017, Vol. 48B, pp. 2281-2292.
- [40] R. Osei, S. N. Lekakh, and R. J. O'Malley: *Met Trans B*, 2021, Vol. 52, pp. 393-404
- [41] RRUFF spectral database, <https://rruff.info/>
- [42] C.W. Bale, R. Chartrand, S.A. Degterov, G. Eriksson, K. Hack, R. Ben Mahfoud, J. Melancon, A.D. Pelton and S. Petersen: *Calphad*, 2002, Vol. 26, pp. 189-228
- [43] W.C. Hagel, *Journal of the American Ceramic Society*, 1965, Vol. 48. No. 2, pp. 70-75
- [44] M. Auinger, R. Naraparaju, H.-J. Christ and M. Rohwerder, *Oxid Met*, 2011, Vol. 76, pp. 247-258
- [45] A.C.S. Sabioni, A.M. Huntz, J. Philibert and B. Lesage, *Journal of Materials Science*, 1992, Vol. 27, pp. 4782-4790
- [46] H. Asteman, J.-E. Svensson, L.-G. Johansson and M. Norell, *Oxide Met*, 1999, Vol. 52, No. ½, pp. 95-111

- [47] H.F. Marston, P.H. Bolt, G. Leprince, M. Order, R. Klima, J. Niska and M. Jarl, *Iron and Steelmaking*, 2004, Vol. 31. No.1 pp. 57-65
- [48] Y. Wang, Y. Sohn, Y. Fan, L. Zhang, and L. An, *Journal of Phase Equilibria and Diffusion*, 2006, Vol. 27, No. 6, pp. 671-675

III. THERMODYNAMIC PREDICTION AND EXPERIMENTAL VERIFICATION OF MULTI-PHASE COMPOSITION OF SCALE FORMED ON REHEATED ALLOY STEELS

Richard Osei¹, Simon Lekakh¹, Ronald O'Malley¹

¹Peaslee Steel Manufacturing Research Center, Department of Materials Science and Engineering, Missouri University of Science and Technology, Rolla, MO, USA, 65409

ABSTRACT

The structure, phase and composition of scale formed on a continuously cast steel slab during reheating depends on intrinsic factors (steel chemistry, microstructure, and as-cast surface condition) and extrinsic parameters (temperature, time, composition, and velocity of combustion gas atmosphere). The scale that forms on a slab normally has several layers with differing compositions and phases and knowledge of this scale structure is important in subsequent de-scaling and hot rolling processing steps.

Formation of multi-phase scale structures on steel during high temperature oxidation in reheat furnace proceeds according to a local thermodynamic equilibrium, while thickness of layers depends on kinetic conditions (mostly by diffusion). In this study, the local thermodynamic equilibrium conditions through the scale layer were simulated using different oxygen/steel ratios, which mimicked the conditions for scale formation at the external, internal and sublayer oxide region at metal/scale boundary.

Experiments were performed in a simulated combustion atmosphere using typical industrial reheat time/temperature conditions. The phases that developed in layered scale

structure were documented using SEM/EDX and Raman spectroscopy. The predicted scale compositions and phases were in good agreement with the experimental results for studies with *Mn* and *Si* alloyed carbon steel, *Cr* alloyed ferritic, and *Cr, Ni* alloyed austenitic steels.

Keywords: oxidation, scale structure, oxide phases

1. INTRODUCTION

Scale formation in a typical steel processing plant begins during the continuous casting of a slab and continues through slab reheating and hot rolling of the steel. Scale formation during reheating is a complex phenomenon which has been described in numerous studies conducted over the past several decades [1-6]. The formation of oxide scale on steel at various processing stages is affected by a combination of intrinsic factors (steel grade, microstructure, segregation, grain boundary, surface roughness) and extrinsic factors (gas atmosphere, gas flow, furnace pressure, temperature, exposure time, furnace throughput, and mechanical and thermal stresses) [4-9]. With a combination of these factors, the formed oxide scale might be easily removed by water jet descaling, or it may be sticky and hard to remove from the steel surface, leaving a residual scale after descaling that interferes with subsequent processes such as hot rolling [10, 11]. To promote surface cleanliness of the steel, water jet descaling [12, 13] is most commonly conducted in multiple stages to improve the efficiency of scale removal using both primary and secondary descaling steps. This descaling normally occurs after slab reheating and prior to the final hot rolling pass. In some cases, depending on the severity

of the scale formed on the as-cast slab, descaling is carried out at the exit of the caster to remove scale and mold flux residues, or the slab is scarfed or surface ground in cases of extreme scale formation. This slab surface conditioning is sometimes performed to minimize the development of complex scale structures at scale/metal boundary during slab reheating in a combustion gas atmosphere.

Due to the demand for steels with improved properties for various applications in the automotive, manufacturing, construction and other industry sectors, steel producers have adjusted steel chemistry with increasing levels of alloying elements (*Si, Mn, Ti, Cr*) and have increasing restricted impurity levels (*Cu, S, P*) to meet modern demands for improved steel properties. Reheating of such steels in furnaces with combustion atmospheres (CO_2, O_2, H_2O, N_2) promotes the formation of multi-layered scale structures with strong adhesion to steel surface, particularly in the case of high *Si* and *Al* steels [14], which interferes with water jet descaling and leads to inefficient scale removal. The complexity of such scale structures has been reported for different steel compositions, such as low to medium carbon steels [4, 6, 15-18], ferritic stainless steels [19-21] and austenitic stainless steels [22-26]. These high temperature oxidation studies were performed to document the scale growth kinetics and the mechanisms of scale formation. Characterization of the scale was performed using scanning electron microscopy coupled with energy dispersive X-ray (SEM/EDX), Raman spectroscopy, transmission electron microscopy (TEM) and X-ray diffraction to document microstructure, chemistry, and oxide phases present in the scale layers for the different steels.

The rate of scale formation for the different steel grades during oxidation is controlled by kinetics [27, 28], while phases that form are defined by the local

thermodynamic conditions. The transport mechanisms responsible for oxidation rate is often driven by solid state or gas pore diffusion; however, the total mass transfer can also be limited by a chemical reaction step or convective mass transport and/or starvation of oxygen in the gas atmosphere near the slab surface. These mechanisms depend on oxidation time and temperature, atmosphere composition, gas flow rates, as well as steel chemistry which promotes the formation of complex structures. Unlike kinetics, thermodynamic approach to study oxidation utilizes the initial and final macroscopic states assuming global or local equilibrium conditions [29] without considering mass transfer. Irrespective the kinetics, thermodynamics is a powerful tool that can be used to predict the feasibility of an oxidation reaction and to qualitatively identify the possible oxide phases that can form during oxidation [29].

Thermodynamic software utilizing the fundamental principle of Gibbs free energy minimization has been used for analyzing various steelmaking processes and experimental reports support its reliability [30-37]. Common areas in steelmaking that have employed thermodynamic studies include refining and non-metallic inclusion formation in the melt, as well as precipitate formation in the solid. The feasibility of thermodynamic studies for a large volume of processed liquid steel relates to: (i) intensive mixing during sufficient time and (ii) high melt temperature, both factors that allow the chemical reactions to proceed close to equilibrium. In contrast, precipitate formation in the solid state typically occurs without mixing and at lower temperatures. However, micro-scale distances also allow the use of thermodynamic tools to predict equilibrium precipitate formation when assuming fast diffusion.

Considering the case of steel oxidation during reheating, gas/solid oxidation reactions occur at high temperatures over a time frame of several hours, but the substantial thickness of the oxide that forms provide sufficient kinetic resistance which prevents the achievement of a global thermodynamic equilibrium, preventing access of oxidant to the whole metal volume. However, the actual process of multi-phase scale formation occurs according to a local thermodynamic equilibrium at each reaction boundary. Therefore, thermodynamic methods can be employed to predict the phases that form at different distances from external metal/gas boundary without reference to the actual thickness of the formed layers. This approach has been used in several studies of alloy oxidation and has been found to be useful to predict the sequence of phases that form in scale during steel reheating [38].

In this study, FACTSAGE thermodynamic software [39] was used to simulate the local equilibrium conditions for scale formation for different steel grades to predict multi-phase composition and these results were compared to experimentally observed scale structures.

2. PROCEDURES

2.1. STEELS AND OXIDATION

A variety of industrially produced steels were used in this study (Table 1). The steels studied included: carbon steels (Class 1) with varying alloying elements (*Si*, *Mn*, *Cr*, and *Ni*), advanced high strength steels (Class 2) with high alloying elements (*Si* and *Mn*), ferritic stainless steels (Class 3) with varying *Cr*, *Al* and *Ti* contents, and high *Ni*

and Cr austenitic stainless steel (Class 4). These cast steels were supplied by industrial sponsors. Samples used for the oxidation test were machined to 50x20x3.5 mm and finished using wet machine grinding with 60 grit silicon carbide, the surface quality of the ground sample was measured to have Ra of 0.271 μm using 3D optical profiler (Nanovea, Model PS50 Micro Photonic Inc.)

Oxidation testing was carried out using a laboratory thermo-gravimetric setup in a vertical $MoSi_2$ resistance-heating tube furnace (Model D900438 ATS Inc.). The oxidation tests were conducted in a combustion gas atmosphere by mixing gases in proportions that reproduced the reacted natural gas + air combustion atmosphere used in an industrial furnace (Table 2). Thermal conditions (temperature and time) and combustion atmosphere were designed to mimic a typical industrial re-heating used these grades before hot rolling.

Table 1. Composition of studied steels.

Steel Class	Code	Composition, wt. %							
		<i>C</i>	<i>Mn</i>	<i>Si</i>	<i>Cr</i>	<i>Cu</i>	<i>Ni</i>	<i>Ti</i>	<i>Al</i>
Carbon	1a	0.17	0.84	0.06	0.14	0.26	0.13	-	0.03
	1b	0.06	1.30	0.33	0.07	0.34	0.10	-	0.04
Advanced High Strength	2a	0.19	2.51	0.99	0.04	0.02	0.02	-	0.04
	2b	0.19	2.97	2.52	0.04	0.02	0.02	-	0.04
Ferritic	3a	0.04	0.43	0.39	16.19	0.25	0.19	-	0.01
	3b	0.04	0.41	0.53	16.02	0.25	0.18	-	0.20
	3c	0.01	0.30	0.32	11.03	0.18	0.13	0.19	0.02
Austenitic	4	0.02	7.10	0.56	15.94	0.80	4.57	-	-

Samples after oxidation were mounted in epoxy to protect scale layer, carefully cross sectioned using wet cutting and mechanically polished using diamond paste. The morphology, thickness, microstructure, and chemistry of the oxide layers were analyzed using a scanning electron microscopy (SEM) with an ASPEX-PIXA 1020 system equipped energy dispersive spectroscopy (EDS). EDS analysis was performed using several points in each scale layer. HORIBA Jobin-Yvon Raman spectroscopy (LabRam ARAMIS) was also used to identify the oxide phases that were present and compared to reported phases in RRUFF database [40].

Table 2. Industrial reheating conditions simulated in laboratory oxidation.

Steel code	Combustion gas, vol. %	Temperature, °C	Time, min
1,2	8 CO_2 , 17 H_2O , 2 O_2 , N_2 bal.	1230	60
3a,b	8 CO_2 , 17 H_2O , 3 O_2 , N_2 bal.	1150	120
3c	8 CO_2 , 17 H_2O , 1 O_2 , N_2 bal.	1205	60
4	8 CO_2 , 17 H_2O , 2 O_2 , N_2 bal.	1260	60

2.2. THERMODYNAMIC SIMULATION

FactSage 7.2 thermodynamic software [39] was used to simulate steel oxidation under the local equilibrium conditions. The data bases used included FSsteel, FToxid and FasctPS. The local equilibrium condition was examined by making stepwise oxygen additions into the simulated streams from previous step assuming irreversible reactions. The predicted stable oxide phases were identified at each calculation step. This method allows one to predict different phases that form at low (inner layer) and high (outer layer) added oxygen levels.

The thermodynamic simulations were performed assuming that the local equilibrium conditions were reached between gas component, the formed oxide phases, and the steel. Preliminary simulations showed that for the studied thermodynamic conditions, oxygen was the predominant oxidant in the combustion gas. Using different oxygen/steel mass ratio, different oxide phases which form under the local equilibrium condition during oxidation were traced from low to high added oxygen levels and compared to the oxide phases reported from the experiments. The equilibrium oxygen partial pressure after formation of the various oxides phases was also reported for each oxygen/steel ratio. The temperatures used in the thermodynamic simulations were similar to those used in laboratory experimental oxidation.

3. RESULTS

3.1. CARBON STEEL

Figure 1 shows the cross-section microstructure of the scale that formed after 60 minutes at 1230⁰C in a laboratory simulated combustion gas atmosphere (Table 2) for two carbon steels having different alloying elements (Table 1). Average scale thickness on these steels was between 500 μm and 700 μm for steel 1a and 1b, respectively. The scale structure was stratified into 4 different layers (1 – outer, 2 – intermediate, 3 – inner, and 4 – subsurface). Each layer was completely (Figure 1a) or partially (Figure 1b) separated from the other. Both the outer and intermediate layers had dense structures with mainly iron oxide as the predominant oxide phase. The inner scale layer had voids and porosity and also included entrapped droplets of unoxidized metal. This layer was

formed next to scale/metal boundary and had isolated islands composed of different oxides of *Mn* and *Si* (Table 3). In steel 1b, which had higher *Si* and *Mn* when compared to low alloyed steel 1a, *Si* and *Mn* oxide, droplets of entrapped metal (*Fe-Ni-Mn*) and porosity in the scale structure increased toward the subsurface layer which had an uneven boundary at the scale/metal interface. A randomly scattered dotted oxide structure was formed in subsurface area below scale/metal interface in the steel 1b. In this case, the subsurface oxidized layer in the metal substrate had a depth ranging between 15 – 50 μm .

Table 3 reports the composition of the oxide scale layers formed in the two studied carbon steels. In both steels, precipitates of alloying element oxides were observed to be more frequent in the inner layer and subsurface layer compared to the outer and intermediate layers. The compositions of the oxides were obtained using EDX point analysis to report chemistry differences in the various scale layers, and the oxide phases were identified by Raman spectroscopy analysis. Fayalite (Fe_2SiO_4) and tephroite (Mn_2SiO_4) were the predominant phases in the inner and subsurface scale layers. The alloying elements in the steels affected the oxide phases formed in subsurface layers, with the higher alloy steel (1b) exhibiting an increased presence of *Si* containing fayalite and *Mn* and *Si* containing tephroite phases.

Thermodynamic simulations of the local equilibrium at different positions through the multi-phase oxide layers were performed by varying the amount of oxygen available to react using different oxygen/steel mass ratios, as shown in (Figure 2). Approximately four different phases were predicted at low oxygen/steel ratios that mimicked the local equilibrium conditions for oxide phase formation in the subsurface and inner scale layer. The oxide phases predicted at this low ratio showed strong presence

of oxides of alloying elements (*Mn* and *Si*) as well as impurities (*Al*). Complexity of the oxide phases decreased toward the external (intermediate and outer) scale layers having higher oxygen/steel ratio with the predicted oxide phase being predominantly hematite (Fe_2O_3) with some traces of tephroite (Mn_2SiO_4).

Thermodynamics predicted the formation of different oxides in the inner scale layers (subsurface and inner) but similar oxides in the external layers (intermediate and outer) for the two alloy steels. In the steel 1b with an elevated concentration of alloying elements, simulations predicted formation of complex *Mn* and *Si* oxides in the form of $MnSiO_3$ and $Mn_3Al_2Si_3O_{12}$ in the inner scale layer; while mono oxides MnO and Cr_2O_3 , and also spinel- $MnAl_2O_4$ was predicted in the lower alloy steel 1a

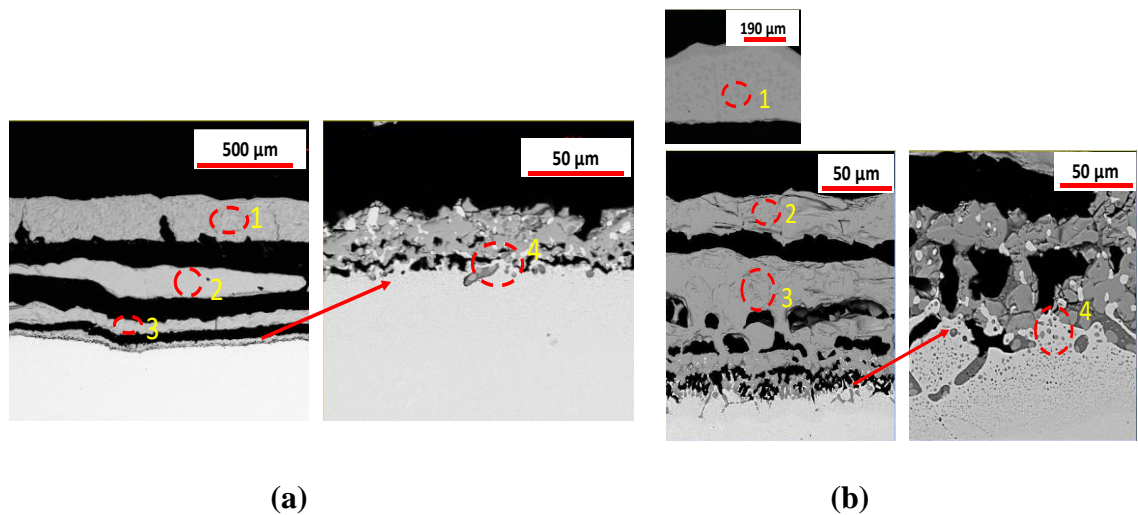


Figure 1. Low (left) and high (right) magnifications BSE image of cross-sectional scale structure in carbon steels: 1a (a) and 1b (b). Number indicated formed layers: 1 – outer, 2 – intermediate, 3 – inner, and 4 – sublayer joined with metal matrix.

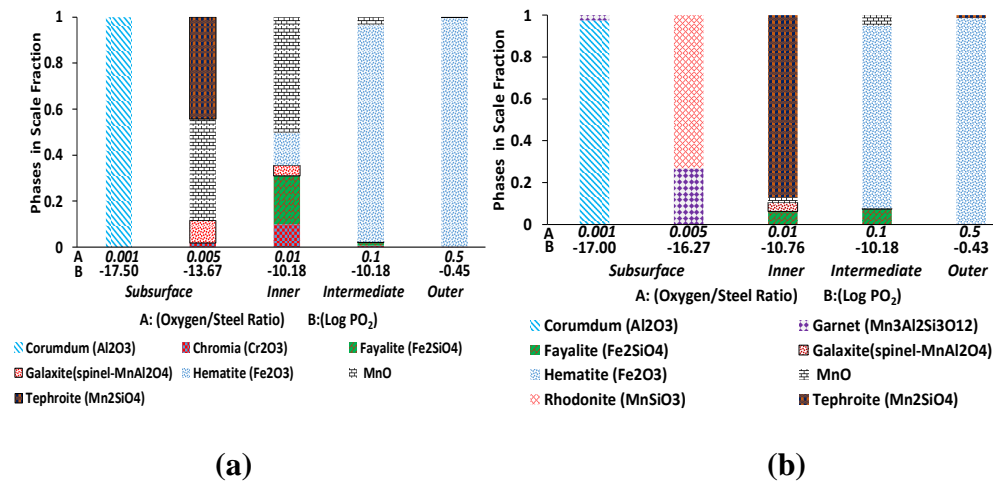


Figure 2. Thermodynamic prediction of oxide phases formed during reheating carbon steel at different oxygen/steel mass ratio: a) carbon steel 1a with low Mn and Si and elevated Cr and b) carbon steel 1b with elevated Si and Mn and low Cr .

Table 3. Characterization of scale chemistry and oxide phases: carbon steel.

Steel	Scale chemistry, wt. %								Oxide phases
	Layer	Fe	O	Si	Mn	Cr	Ni	Al	
1a	Outer (1)	49	50	-	1	-	-	-	Fe_2O_3, Fe_3O_4
	Intermediate (2)	54	45	-	1	-	-	-	Fe_2O_3, Fe_3O_4
	Inner (3)	55	44	-	1	-	-	-	Mn_2SiO_4, Fe_3O_4
		43	51	4	2	-	-	-	
	Subsurface (4)	38	54	5	2	-	-	-	Mn_2SiO_4
		53	46	-	1	-	-	-	
82		10	-	7	1	-	-		
1b	Outer (1)	45	52	-	3	-	-	-	$Fe_2O_3, Fe_3O_4,$
		41	57	-	2	-	-	-	
	Intermediate (2)	46	51	-	2	-	-	-	Fe_3O_4, Mn_2SiO_4
		59	38	-	3	-	-	-	
		31	60	6	3	-	-	-	
	Inner (3)	96	-	-	2	-	2	-	$Fe_3O_4, MnO,$ Mn_2SiO_4
		45	53	-	2	-	-	-	
		52	38	7	3	-	-	-	
	Subsurface (4)	46	36	4	13	-	-	1	$Fe_2SiO_4, MnO,$ Mn_2SiO_4
46		41	1	11	1	-	-		
69		20	1	9	1	-	-		
55		44	-	1	-	-	-		

3.2. ADVANCED HIGH STRENGTH STEELS (AHSS)

In the case of AHSS, the cross section of the scale layer revealed a dense continuous scale structure with partial detachment of outer and intermediate layers from inner and sublayer in steel 2a and complete detachment in higher alloyed by *Si* and *Mn* steel 2b. The average scale thickness on the AHSS after 60 minutes at 1230°C in the combustion atmosphere noted in Table 2 was between 870 – 950 µm with a thicker scale layer observed on high alloy steel 2b. The internal porosity observed in the scale layers formed on the carbon steels was not observed in the scale structure formed in AHSS and penetrating “root-like” dark oxide phases originating from the intermediate and outer layers into the inner and subsurface layers of the sample were observed. The round shape of subsurface oxides indicated possible liquefaction. The results from composition analysis and Raman spectroscopy on the various phases in scale layers are reported in Table 2. The dark continuous oxide phases present in the inner and subsurface layers were identified as fayalite (Fe_2SiO_4) and silica (SiO_2). The inner and subsurface layers contained thick continuous dark *Fe-Si* oxide phases of about 100 µm with embedded metal (*Fe-Ni-Mn*) entrapment and scattered precipitated gray *Fe-Mn* oxide phases was observed by adjusting contrast in SEM/BSE analysis. The subsurface structure contained a superimposed oxide scale in the metal substrate with strong adhesion to inner layer and minimal porosity, cracks, and voids. The oxide phases identified by Raman spectroscopy were similar in the two steels (2a and 2b) with the major difference being the presence of SiO_2 oxide in the inner layer of the high *Si* and *Mn* steel 2b, which was not observed in the medium *Si* and *Mn* steel 2a (Table 4). Both steels contained phases of *MnO* and Fe_2SiO_4 .

Figure 4 reports the thermodynamically predicted solid oxides and liquid oxide solutions (slags) at varying oxygen/steel mass ratio for the AHSS samples under the local equilibrium conditions at reheating temperature. The outer oxide phase in both AHSS grades were predicted to be pure iron oxide (about 95%) with traces of solid *Mn-Si* oxide-based phases. The phases predicted in the subsurface and the inner layer contained a mixture of solid oxides of alloying elements (*Si* and *Mn*) and liquid oxide phases. A greater amount of silicon-based solid oxide phases and liquid oxide solutions in the subsurface through to the intermediate layer were predicted in steel 2b which had higher *Si* and *Mn* concentrations in the steel. These liquid solutions had average compositions: Slag 1 (51 wt.% SiO_2 , 34 wt.% MnO , 15 wt.% Al_2O_3), Slag 2 (69 wt.% FeO , 15 wt.% SiO_2 , 11 wt.% MnO , 5 wt.% Fe_2O_3), and Slag 3 (33 wt.% Fe_2O_3 , 32 wt.% SiO_2 , 18 wt.% MnO , 13 wt.% Mn_2O_3 , 4 wt.% FeO).

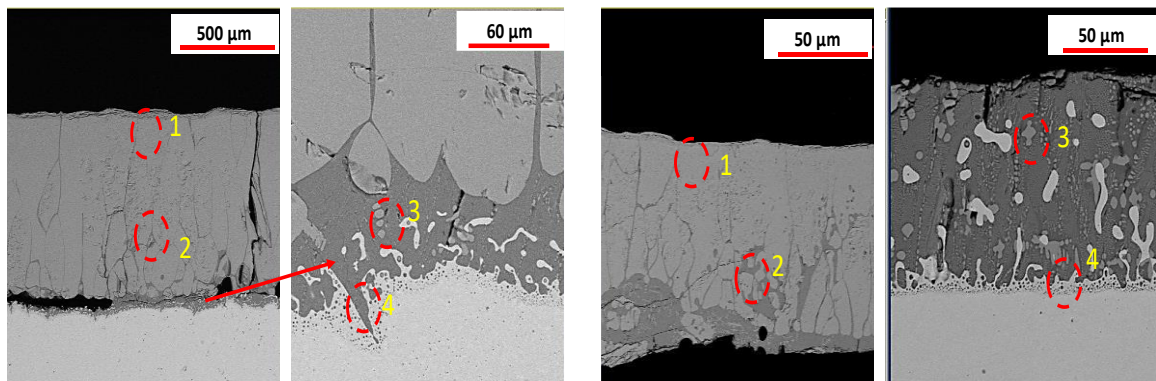


Figure 3. Low (left) and high (right) magnifications BSE image of cross-sectional scale structure in advanced high strength steels: 2a (a) and 2b (b). Number indicated formed layers: 1 – outer, 2 – intermediate, 3 – inner, and 4 – sublayer joined with metal matrix.

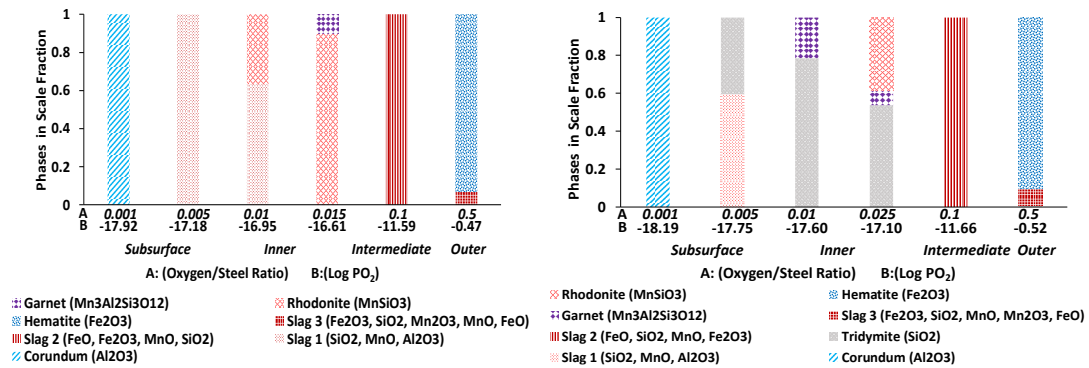


Figure 4. Thermodynamic prediction of oxide phases present during reheating AHSS at different oxygen/steel mass ratio left) steel 2a with medium *Mn* and *Si*, and right) steel 2b with high *Mn* and *Si*.

Table 4. Characterization of scale chemistry and oxide phases AHSS.

Steel	Layer	Scale chemistry, wt. %						Oxide phases
		<i>Fe</i>	<i>O</i>	<i>Si</i>	<i>Mn</i>	<i>Ni</i>	<i>Cr</i>	
2a	Outer (1)	42	55	-	3	-	-	Fe_2O_3, Fe_3O_4
	Intermediate (2)	39	53	5	3	-	-	$Fe_2O_3, Fe_3O_4, Fe_2SiO_4$
	Inner (3)	96	-	-	3	1	-	MnO, Fe_2O_3
		27	62	7	4	-	-	
	Subsurface (4)	33	59	5	3	-	-	MnO, SiO_2, Fe_2SiO_4
		45	53	-	2	-	-	
32	45	5	17	-	1			
2b	Outer (1)	45	52	-	3	-	-	Fe_2O_3, Fe_3O_4
	Intermediate (2)	40	52	5	3	-	-	$Fe_2O_3, Fe_3O_4, Fe_2SiO_4$
	Inner (3)	32	59	6	3	-	-	SiO_2, MnO
	Subsurface (4)	45	52	-	3	-	-	$Fe_2O_3, SiO_2, Fe_2SiO_4, MnO$
		31	59	6	4	-	-	
		37	48	5	10	-	-	

3.3. FERRITIC STAINLESS STEEL

Three stainless steels with low *Al* (steel 3a), high *Al* (steel 3b), and *Ti*-bearing (steel 3b) were studied. All these steels were highly alloyed with *Cr* in addition to *Mn*. Cross-section analysis of the oxidized steels revealed a complex scale structure that could best be classified into four layers: 1 – outer, 2 – intermediate, 3 – inner, and 4 –

subsurface (Figure 5). The average total scale thickness for these 3 stainless steels oxidized under the conditions noted in Table 2 was measured to be 1000, 900 and 600 μm for the steels 3a, 3b and 3c respectively. The wide variation in scale thickness was due to the different steel chemistry and the different applied industrial oxidation conditions (Table 1 and Table 2). In all cases, the outer, intermediate and inner layers represented nearly 95-96% of the total scale thickness and the subsurface layer made up of the remaining 4-5%. The typical structure of the outer scale layer on the ferritic stainless steels consisted of dense continuous layers containing iron oxide without any traces of alloying elements. However, the intermediate layer structure had porosity and voids coupled with microscopic and macroscopic transverse and lateral cracks.

The chemistry and oxide phases in the intermediate layer were predominantly hematite (Fe_2O_3) and chromia (Cr_2O_3), while the inner layer contained a mixture of chromite (FeCr_2O_4), hematite (Fe_2O_3), chromia (Cr_2O_3), and fayalite (Fe_2SiO_4) phases with impurities of *Ni* and *Cu* (Table 5). The subsurface scale layer was strongly attached to the metal substrate with heavily superimposed oxides in the metal matrix. In general, two *Cr* based phases were observed in the subsurface region, high *Cr* with traces of *Si* and low *Cr* with high *Si* content (Table 5). The stainless steel with *Al* (steel 3b) developed a subsurface scale layer with a significant presence of *Al* oxides. Titanium oxide was not detected in analysis of the scale chemistry in the *Ti* bearing steel 3c.

Thermodynamic simulations (Figure 6) of the oxidation sequence in these steels predicted the formation of specific oxides at the scale/metal boundary at low oxygen/metal ratios. In the case of the low *Al* steel 3a, the predicted subsurface oxides phases were predominantly *Cr* and *Si* based oxides with trace of *Al-Mn-Si* oxide phase.

Aluminum oxide (Al_2O_3) and other *Al*-based complex *Al-Mn-Si* oxide were formed in the subsurface layer of the high *Al* steel 3b. In the case of steel grade 3c having traces of *Ti*, thermodynamics predicted a complex multi-component subsurface scale formation, having evidence of *Ti*-based oxides mixed with *Al* and *Si* based oxide phases which extended to the inner scale layer. A mixture of *Cr*- and *Fe*-based oxide phases identified in the experimental investigation were predicted by thermodynamic for these steels in the intermediate to outer scale layer with traces of a *Si*-based phase mixture as described in Table 5

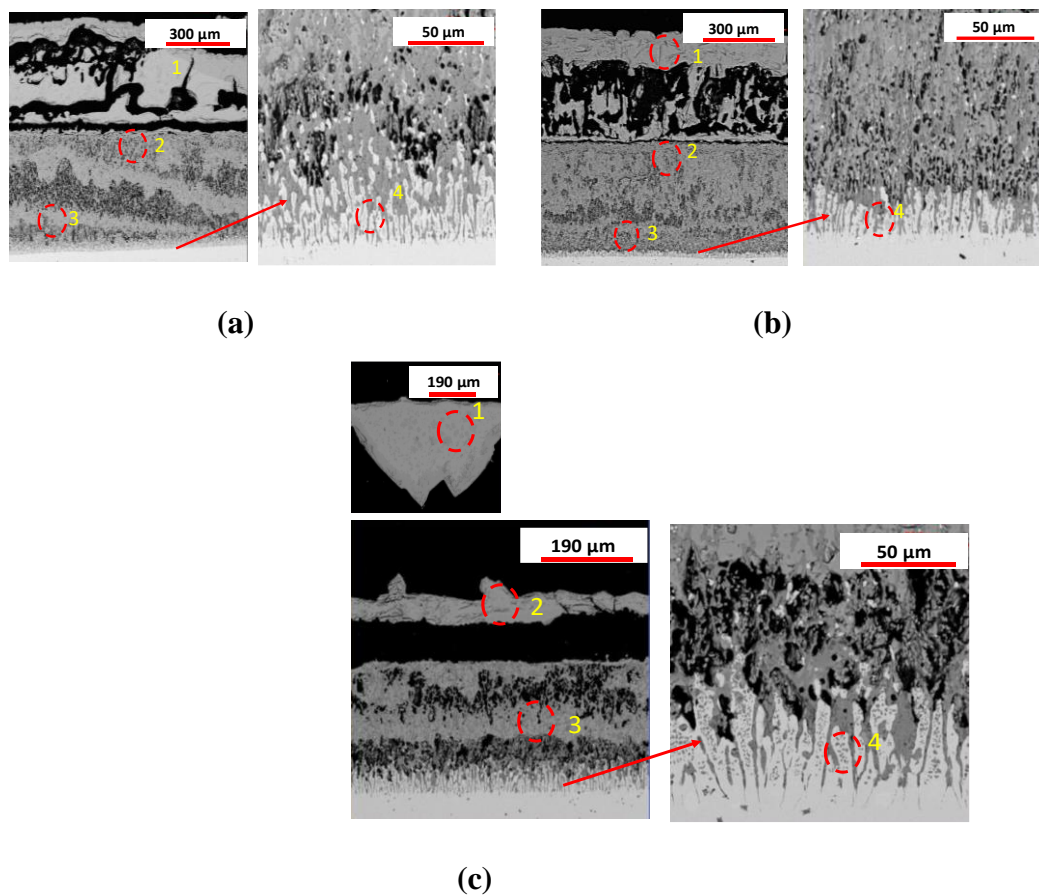


Figure 5. Low (left) and high (right) magnifications BSE image of cross-sectional scale structure in ferritic steels 3a (a), 3b (b), and 3c (c). Number indicated formed layers: 1 – outer, 2 – intermediate, 3 – inner, and 4 – sublayer joined with metal matrix.

Table 5. Characterization of scale chemistry and oxide phases in ferritic stainless steels.

Steel	Scale chemistry, wt. %										Oxide phases
	Layer	Fe	O	Si	Mn	Cr	Ni	Al	Ti	Cu	
3a	Outer (1)	43	57	-	-	-	-	-	-	-	Fe_2O_3
	Intermediate (2)	53	44	-	1	2	-	-	-	-	Fe_2O_3 , Cr_2O_3
		33	53	-	-	14	-	-	-	-	
	Inner (3)	46	49	-	1	4	-	-	-	-	Cr_2O_3 ,
		32	57	4	-	7	-	-	-	-	
	Subsurface (4)	16	60	-	-	24	-	-	-	-	Cr_2O_3 SiO_2 , $FeCr_2O_4$
32		57	5	-	6	-	-	-	-		
3b	Outer (1)	43	57	-	-	-	-	-	-	-	Fe_2O_3
	Intermediate (2)	54	43	-	1	2	-	-	-	-	Fe_2O_3 , Cr_2O_3
		31	54	-	-	15	-	-	-	-	
	Inner (3)	45	50	-	1	4	-	-	-	-	Fe_2O_3 , Cr_2O_3
		46	49	-	-	5	-	-	-	-	
	Subsurface (4)	29	57	5	-	9	-	-	-	-	$FeCr_2O_4$, Cr_2O_3 , Fe_2SiO_4
28		43	-	1	21	-	7	-	-		
17		58	1	-	24	-	-	-	-		
3c	Outer (1), Intermediate (2)	53	46	-	1	-	-	-	-	-	Fe_2O_3
	Inner (3)	26	52	-	-	22	-	-	-	-	Fe_2O_3 , Fe_2SiO_4 $FeCr_2O_4$
		50	45	-	1	4	-	-	-	-	
		36	51	5	1	8	-	-	-	-	
		81	1	-	1	5	10	-	-	2	
	Subsurface (4)	48	44	-	1	7	-	-	-	-	Fe_2SiO_4 $FeCr_2O_4$
		25	54	-	-	23	-	-	-	-	
		32	56	4	-	8	-	-	-	-	
50		46	-	1	3	-	-	-	-		

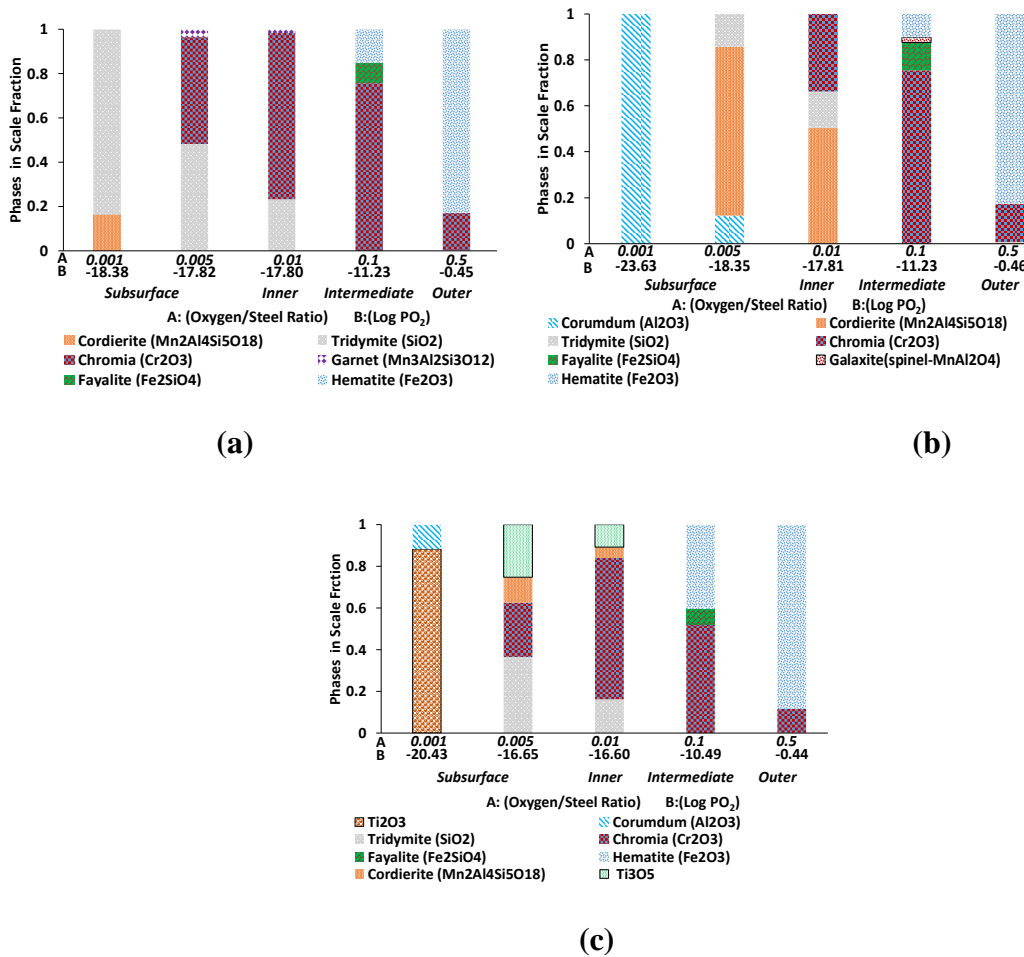


Figure 6. Thermodynamic prediction of oxide phases present during reheating *studied* ferritic steels at different oxygen/steel mass ratio: a) steel 3a with low Al, b) steel 3b with high Al, and c) steel 3c with Ti.

3.4. AUSTENITIC STEELS

Scale structures formed on the studied austenitic stainless-steel that was highly alloyed with *Cr*, *Ni* and *Mn* are shown in Figure 7. This scale at the outer and intermediate layers was completely separated from the inner and subsurface layers and high levels of porosity were observed in the intermediate scale layer. The inner-subsurface layer had a thickness of about 270 μm with a dense oxide structure superimposed in the metal matrix. The total scale thickness in this steel averaged about

900 μm . The composition and phases measured in these two layers consisted mainly of *Fe*- and *Mn*-based oxides (Table 6). The inner and subsurface layers were fused together and strongly attached to the base metal substrate, having a complex oxide chemistry comprising of different ratios of *Fe*, *Mn*, *Si* and *Cr* (Table 6).

Thermodynamic simulation of the oxidation of this stainless steel predicted the formation of several layers with different oxide phases (Table 4). A monoxide phase (Mn_2SiO_4) was predicted in the subsurface and through to the inner oxide layer. Multi phases having *Cr*, *Mn*, *Fe* and *Ni* based oxides were predicted in the intermediate and outer scale layer.

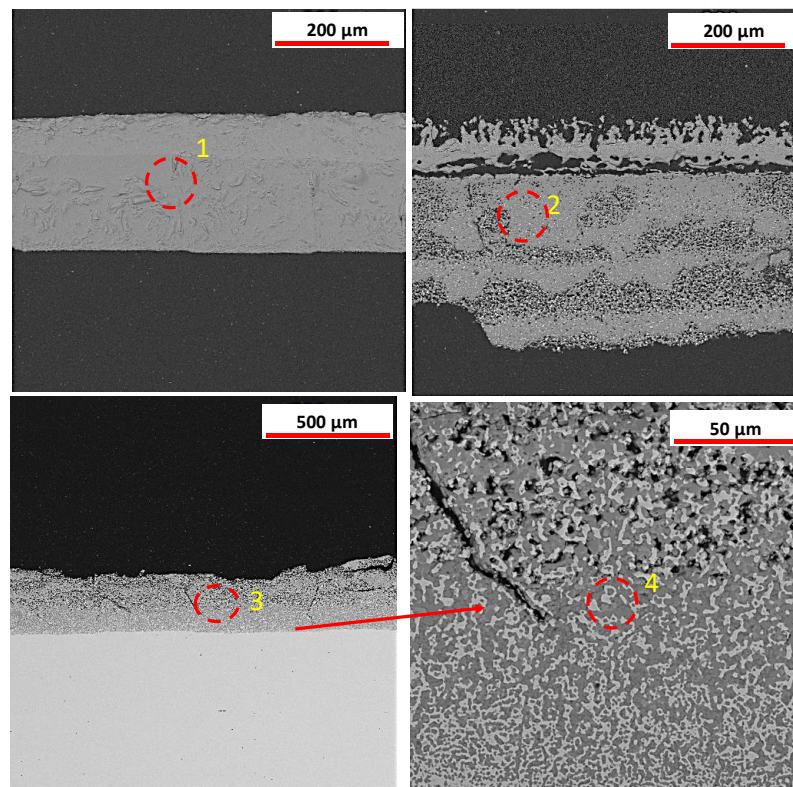


Figure 7. Low (left) and high (right) magnifications BSE image of cross-sectional scale structure in austenitic steel (4). Number indicated formed layers: 1 – outer, 2 – intermediate, 3 – inner, and 4 – sublayer joined with metal matrix

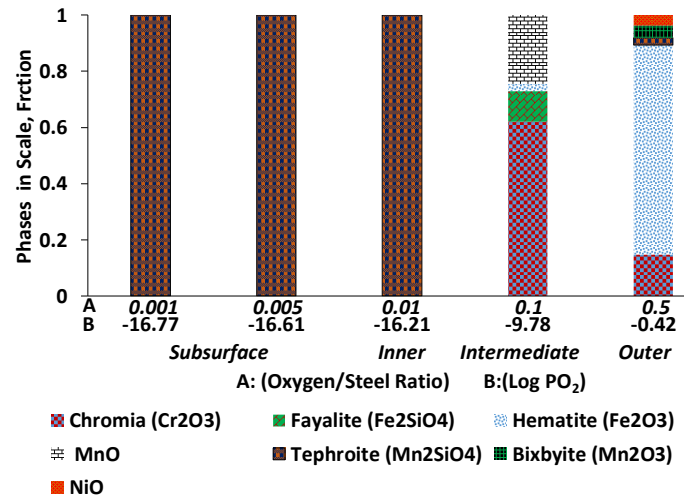


Figure 8. Thermodynamic prediction of oxide phases present during reheating austenitic steel 4 with high Ni and Cr at different oxygen/steel mass ratio.

Table 6. Characterization of scale chemistry and oxide phases in austenitic stainless steel (4).

Steel	Scale chemistry, wt. %							Oxide phases
	Layer	Fe	O	Si	Mn	Cr	Ni	
4	Outer	45	49	-	4	2	-	<i>MnO, Fe₂O₃, Fe₃O₄</i>
	Intermediate	28	52	-	3	15	2	<i>MnO, Fe₂O₃, Fe₃O₄</i>
	Inner	52	42	-	2	4	-	<i>MnO, Mn₂SiO₄, Fe₂O₃, Cr₂O₃,</i>
		16	57	-	2	25	-	
		8	57	-	5	30	-	
		28	47	4	7	14	-	
	Sub	29	53	5	6	7	-	<i>SiO₂, FeCr₂O₄, Cr₂O₃, MnSiO₃</i>
		14	52	-	8	26	-	
		44	47	-	4	5	-	
		37	51	-	2	10	-	
32		54	5	6	3	-		

4. DISCUSSION

The scale formed in the different steels had a multi-layered structure and complex phase compositions, as well as defects such as cracks, pores, and delamination from the

metal matrix. Formation of the different scale layers is governed by mixed thermodynamic and kinetic oxidation mechanisms. However, considering reheating process time and high temperature, local thermodynamic equilibrium can be used to predict multi-layered scale structure and characterize phase composition in the external, internal, and subsurface layers. The experimental work characterized the type of scale formed in different steel grades and identified structure, phases, and compositions of the different oxide layers formed in scale during reheating in a combustion furnace atmosphere. Thermodynamic simulations of the local equilibrium at different oxygen/steel ratios were used to predict the phases that formed at different distances from the sample surface.

These simulations showed strong similarities with experimentally observed phases in scale. However, there were also some differences between the actual scale structure and the theoretical thermodynamic predictions. These differences may be due to assumptions used in the simulation of the local equilibrium as well as limitations of the analytical method used in this study for the oxide phase identification. Additional methods such as electron diffraction and high-resolution TEM might be needed to explain these differences. Table 7 presents the details of these findings. One steel from each studied steel type was selected for this comparison. Steels 1b and 2b were selected for carbon steels and AHSS due to the presence of *Si* and *Mn* alloying element in these steels. For stainless steel, chemistry 3b was selected due to the high *Al* content in this steel.

In carbon steel 1b with elevated *Mn* and *Si*, thermodynamics predicted Fe_2O_3 , Mn_2SiO_4 , MnO and Fe_2SiO_4 oxide phases in the different scale layers. This layered

structure was also observed in the experimental scale and supported by EDX chemistry analysis and Raman spectroscopy phase identification. Thermodynamics predicted the formation of small amounts of phases such as Cr_2O_3 , Al_2O_3 , and $MnAl_2O_4$ at low oxygen/steel mass ratio. However, these phases were not detected in experimental scale using the Raman spectroscopy analysis. In contrast, trace levels of these elements were detected using EDX chemistry analysis of inner and subsurface of the oxide scale (Table 3)

For AHSS, thermodynamics predicted the formation of Fe_2O_3 , SiO_2 , and MnO solid oxide phases in the scale layers which were also identified in the experimental scale structure. Differences observed between thermodynamics predictions and experimental investigations where the predicted formation of predominant Mn_2O_3 and FeO in the external scale layers and $Mn_2Al_4Si_5O_{18}$, and mono Al_2O_3 in the internal layers. These phases were not identified in experimental Raman spectra, whereas EDX chemistry analysis of the external (outer and intermediate) scale layers did detect the presence Mn and Si (Table 4). Also, it was difficult to identify the complex phases which were present as complex liquid solutions.

Thermodynamics predicted the formation of Cr_2O_3 , Fe_2O_3 , Fe_2SiO_4 , Al_2O_3 , SiO_2 , $MnAl_2O_4$, $Mn_2Al_4Si_5O_{18}$ in the ferritic stainless. Similar oxides of (Cr_2O_3 , Fe_2O_3 and Fe_2SiO_4) phases were observed in experimental scale phase identification. At the same time, experimental investigations observed the presence of iron chromite $FeCr_2O_4$ occurring in the subsurface region. Thermodynamics predicted phases of SiO_2 , Al_2O_3 , $Mn_2Al_4Si_5O_{18}$ in the internal (subsurface and inner) scale layers at low oxygen/steel mass ratio. The space resolution (10x) of the Raman spectroscopy method did not allow

identification these phases, while elements forming these phase (*Mn, Si, Al*) were reported in the EDX scale chemistry analysis (Table 5). These results support the possibility of forming thermodynamic predicted oxide phases in the subsurface structure.

Table 7. Experimental vs. thermodynamic prediction of oxide phases in studied steel grades.

Steel	Phases Present in Various Oxide Scale Layers				
		Outer	Intermediate	Inner	Subsurface
1b	Experimental	Fe_2O_3 , Fe_3O_4	Fe_3O_4 , Mn_2SiO_4	MnO , Mn_2SiO_4 , Fe_3O_4	Fe_2SiO_4 , MnO , Mn_2SiO_4
	Simulated	Fe_2O_3 , Mn_2SiO_4	Fe_2O_3 , Fe_2SiO_4 , MnO	MnO , Fe_2O_3 , $MnAl_2O_4$, Cr_2O_3 , Fe_2SiO_4	Mn_2SiO_4 , MnO , $MnAl_2O_4$, Cr_2O_3 , Al_2O_3
2b	Experimental	Fe_2O_3 , Fe_3O_4	Fe_2O_3 , Fe_3O_4 , Fe_2SiO_4	SiO_2 , MnO	MnO , Fe_2O_3 , SiO_2 , Fe_2SiO_4
	Simulated	Fe_2O_3 , Slag 3 (Fe_2O_3 , SiO_2 , MnO , Mn_2O_3FeO .)	Slag 2 (FeO , SiO_2 , MnO , Fe_2O_3)	SiO_2 , $MnSiO_3$, $Mn_3Al_2Si_3O_{12}$	Al_2O_3 , SiO_2 , Slag 1 (SiO_2 , MnO Al_2O_3)
3b	Experimental	Fe_2O_3	Fe_2O_3 , Cr_2O_3	Fe_2O_3 , Cr_2O_3	Fe_2SiO_4 , $FeCr_2O_4$, Cr_2O_3
	Simulated	Cr_2O_3 , Fe_2O_3	Cr_2O_3 , Fe_2O_3 , Fe_2SiO_4 , $MnAl_2O_4$	Cr_2O_3 , SiO_2 , $Mn_2Al_4Si_5O_{18}$	Al_2O_3 , SiO_2 , $Mn_2Al_4Si_5O_{18}$
4	Experimental	Fe_2O_3 , Fe_3O_4 , MnO	MnO , Fe_2O_3 , Fe_3O_4	Mn_2SiO_4 , Cr_2O_3 , $MnSiO_3$, Fe_3O_4	SiO_2 , $FeCr_2O_4$, Cr_2O_3 , $MnSiO_3$
	Simulated	Cr_2O_3 , Fe_2O_3 , Mn_2SiO_4 , NiO , Mn_2O_3	Cr_2O_3 , Fe_2SiO_4 , Fe_2O_3 , MnO	Mn_2SiO_4	Mn_2SiO_4 ,

In austenitic stainless steels with high *Mn*, *Cr* and *Ni*, thermodynamics predicted the formation of (Fe_2O_3 , MnO , Cr_2O_3 , Mn_2SiO_4) phases in the scale layers were also identified in experimental investigations. Thermodynamics predicted the formation of a mono oxide phase in the inner and subsurface layers (Mn_2SiO_4), while experimental scale phase identification reported the formation of a multi-phase composition (Mn_2SiO_4 , Cr_2O_3 , $MnSiO_3$, Fe_3O_4 , $FeCr_2O_4$) with elements making up these phases, in good agreement with EDX chemistry analysis of this scale layers (Table 6). The external (outer and intermediate) scale layers predicted by thermodynamics indicated the formation of NiO and Cr_2O_3 . These oxides were not identified in the experimental scale by Raman spectroscopy, possibly due to the small amounts present. However, EDX analysis did show evidence of *Ni*, *Cr* and *O* in the collected spectra. (Table 6).

The experimental and simulation results presented in this article are limited to oxidation during re-heating of a clean milled surface. However, our research has shown that mold flux residues and the roughness of the as-cast surface can have a significant impact on scale formation and scale morphology. The effects of slab surface quality on oxidation will be presented in a future publication.

5. CONCLUSION

Oxide scale structures, phases and compositions that formed during the reheating of four classes of low alloyed carbon, AHSS, ferritic stainless, and austenitic stainless steels were investigated experimentally and using thermodynamic simulations applying the local equilibrium approach by varying oxygen/steel ratio. The experimentally

observed scale structures were documented and the oxide phases formed in the various steels during oxidation were in good agreement with thermodynamic predictions. At the same time, experimental results showed that the formation of multi-layered scale structures on the different steel grades is associated with unique structural characteristics such as crack, void, porosity, and detachment, which cannot be revealed by thermodynamics because mostly depend on the physical properties of formed oxides and reaction kinetics. The current study demonstrates the potential of using a thermodynamic simulation methodology to predict multi-phase oxide scale composition in alloys steels to provide reasonable guidance for subsequent technological processes such as descaling and hot rolling.

ACKNOWLEDGEMENTS

This study is supported by Kent Peaslee Steel Manufacturing Research Center, and the authors express their appreciation to partner industrial members of this project for supplying material for this study.

REFERENCES

- [1] J.S. Sheasby, W.E. Boggs and E.T. Turkdogan: *Met. Sci.*, 1984 Vol. 18, pp. 127-136.
- [2] W. Sun: *PhD thesis*, 2005, School of Mechanical, Materials and Mechatronic Engineering, University of Wollongong.
- [3] O. A. Zambrano, , J.J. Coronado, and S. A. Rodriguez: *Surface and coating technology*, 2015, Vol. 282, pp. 155-162.

- [4] H.T. Abuluwefa, R.I.L. Guthrie and F. Ajersch: *Oxidation of Metals*, 1996, Vol. 46, pp. 423-440.
- [5] W. E. Boggs: *Metallurgical society of AIME*, 1973, pp. 84-128.
- [6] H.T. Abuluwefa, R.I.L Guthrie and F Ajersch: *Met Trans A*, 1997, Vol. 28A, pp. 1633-164.1
- [7] M.P. Brady, Y. Yamamoto, M. L. Santella and B.A. Pint: *Scripta Materialia*, 2007, Vol. 57, pp. 1117-1120.
- [8] J. C. Bavay and P. Bourgain: *Materials Science and Engineering*, 1987, Vol, 87, pp. 137-143.
- [9] E. W. Grandmaison, H. A Becker, W. R. C. Ormerod, A. Pollard and A. Sobiesiak: *Canadian Journal of Chemical Engineering*, 1997, Vol. 75, pp. 402–413.
- [10]. N. Thanasak, N. K Nisachon and Y Sirilak: *Materials Today*, 2018, Proceedings 5, pp. 9359-9367
- [11] S. R. W. Shatynski and Sherwood: *Surface Technology*, 1984, Vol 21, pp. 39-51.
- [12] M. Raudensky and M. Hnizdil: *Metal*, 2010, Vol. 5, 6 pp.
- [13] J. Horsky, M. Raudenky and L. Bendig: *ILASS-Europe*, 2001, 6 pp.
- [14] Nakakubo S., Onishi T., Takeda M and Fujumato S: *Materials Transactions*, 2009, Vol. 50, No. 9, pp. 2242-2246
- [15] V. Lee, B. Gleeson, and D. Young: *Oxidation of Metals*, 2005, Vol. 63, pp.15–31.
- [16] R. Chen and W. Yeun: *Oxidation of Metals*, 2003, Vol. 59, pp. 433–468
- [17] R. Y. Chen. and W. Y. D Yuen: *Oxidation of Metals*, 2010, Vol. 73, pp. 353-373.
- [18] R. Y. Chen. and W. Y. D Yuen: *Oxidation of Metals*, 2010, Vol. 59, No.5/6, pp. 433-468.
- [19] Y. Zhang, A. Shi, P. Liang, J. Wang, H. Meng, C. Zhang, Z. Zhang, and P. Han: *Steel Research Int*, 2018, Vol. 89, 7pp.
- [20] X. Cheng, Z Jiang, D. Wei, J. Zhao, B. J. Monaghan, R. J. Longbottom, and L. Jiang: *Surface and Coatings Technology*, 2014, Vol. 258 pp. 257-267.

- [21] J. C. Bavay and P. Bourgain: *Materials Science and Engineering*, 1987, Vol. 87, pp. 137-143.
- [22] M.P. Brady, Y. Yamamoto, M. L. Santella and B.A. Pint: *Scripta Materialia*, 2007, Vol. 57, pp. 1117-1120.
- [23] M.P. Brady, Y. Yamamoto, Z.P. Lu, C.T. Liu, P.J. Maziasz and B.A. Pint: *United States Patent Disclosure*, 2007.
- [24] N. Otsuka, Y. Nishiyama and T. Kudo: *Oxidation of Metals*, 2004, Vol. 62, No. 1-2, pp. 121–139.
- [25] H. Asteman, J.-E. Svensson and L.-G. Johansson: *Oxidation of Metals*, 2002, Vol. 57, No. 3-4, pp. 193–216.
- [26] A. Laukka, E-P. Heikkinen and T. Fabritius: *Steel Research Int*, 2018, Vol. 90, 11 pp.
- [27] W. W. Smeltzer: *Acta Metallurgica*, 1960, Vo. 8, pp. 377-383.
- [28] H. T. Abuluwefa: *Lecture Notes in Engineering and Computer Science*, 2012, Vol. 2196, pp. 1664-1668.
- [29] S. K. Dutta and A. B. Lele: *Metallurgical Thermodynamics Kinetics and Numericals*, 1st ed, S. Chand & Company Limited, Ram Nagar, New Delhi, 2012, 188 pp.
- [30] J. M. Alinger, H. Cao and S. V. Dheeradhada: *Journal of Power Sources*, 2011, Vol. 196, pp. 1975-1982.
- [31] I.-H Jung: Overview of the applications of thermodynamic databases to steelmaking processes: *Calphad*, Vol. 34, is. 3, pg. 332-362, 2010.
- [32] S. N. Lekakh, J. Ge, V. Richards, R. O'Malley, and R. J. Terbush: *Met Trans B*, 2017, Vol. 48B, pp. 406-417.
- [33] C.W. Bale, E. BÉlisle, P. Chartrand, S.A. Degterov, G. Eriksson, A.E. Gheribi, K. Hack, I.-H. Jung, Y.-B. Kang, J. Melançon, A.D. Pelton, S. Petersen, C. Robelin, J. Sangster, P. Spencer, and M.-A. Van Ende: *Calphad*, 2016, Vol. 54, pp. 35-53.
- [34] K. Young-Bae, D.K Sazol, H. Taekwon and J In-Ho: *Acta Materialia*: 2014, Vol. 71, pp. 164-175.
- [35] L. Holappa, H. Hamalainen, N, Liukkonen and M. Lind: *Iron and Steelmaking*: 2003, Vol. 30, pp. 111-115.

- [36] P. Joo-Hyun, L. Sang-Beom and R.G Henri: *Met Trans B*, 2008, Vol. 39B, pp. 853-861.
- [37] P.C Pistorius, Y. Ren, and L. Zhang: *Met Trans B*, 2017, Vol. 48B, pp. 2281-2292.
- [38] H Davies and A Dinsdale: *Materials at High Temperatures*, 2005, Vol. 22, No. 1-2, pp. 15-25.
- [39] C.W. Bale, R. Chartrand, S.A. Degterov, G. Eriksson, K. Hack, R. Ben Mahfoud, J. Melancon, A.D. Pelton and S. Petersen: *Calphad*, 2002, Vol. 26, pp. 189-228
- [40] RRUFF spectral database, <https://rruff.info/>

IV. DESCALING OF MEDIUM C AND HIGH SI, MN STEELS

Richard Osei¹, Simon Lekakh¹, Ronald O'Malley¹, Lesli Peterson², Oldair Sasso²

¹Peaslee Steel Manufacturing Research Center, Department of Materials Science and Engineering, Missouri University of Science and Technology, Rolla, MO, USA, 65409

²Spraying Systems Co. Wheaton, IL, USA, 60187

ABSTRACT

Descaling of slabs exiting reheat furnaces prior to hot rolling is an important step to improve surface quality in the steelmaking process. An induction heating system with a controlled atmosphere that replicates the combustion atmosphere in a commercial slab reheat furnace was used to oxidize high-Si, Mn, and medium-C steels. High-pressure water jet descaling was performed following scale formation using a laboratory setup that mimicked the industrial descaling process. Effects of nozzle impact factor (N/mm²) on scale removability for the different steels were investigated. The critical values of impact factor required for scale removal are discussed.

Keywords: oxidation, reheating, descaling, scale structure, water jet impact factor

1. INTRODUCTION

Reheating of an as-cast slab to its deformation temperature prior to hot rolling is a common step in steel processing to facilitate thickness reduction and shaping to form a hot rolled product. During reheating, cast slabs are exposed to a combustion atmosphere

containing oxidizing components such as residual oxygen, CO_2 , and water vapor, leading to the formation of unwanted oxide scale up to several millimeters thick which affect surface quality of the hot rolled strip [1]. The scale that forms need to be removed prior to hot rolling deformation due to adverse effect it has on the hot rolled surface quality, the roll-strip interfacial behavior, and other undesired effects [2,3]. Scale removal is normally achieved by high pressure (up to about 4000 psi) hydraulic water jet descaling and this process can be further classified into primary and secondary descaling steps.

The primary descaling process is generally performed right after slab reheating prior to entrance into the first roughing hot rolling stand. This descaling process may be repeated, in some cases 3 times, in conjunction with each hot rolling reduction step with the goal of removing the primary scale that formed during continuous casting and reheating. In some cases, an additional primary descaling step may be incorporated between casting and reheating of slab to reduce effect of scale formed during continuous casting. The secondary descaling step is performed between the roughing and finishing mill to remove secondary scale which forms during the rolling process when hot strip is exposed to air. If these two steps do not produce the required surface quality, surface grinding of the cast slab is also sometimes performed to further assist descaling, particularly for steel grades which are susceptible to forming highly adhesive and tough to remove scale on the hot rolled product and also to remove defects from the casting process.

The efficiency of descaling is strongly influenced by the complex structure of the formed oxide scale [1, 4-8], as well as descaling process parameters including nozzle design [9-11], hydraulic parameters [12,13] and process mechanical design. The

characteristics of the formed oxide scale is highly influenced by steel chemistry, temperature, and furnace atmosphere conditions. Because these multiple factors can interact with each other, comprehensive analysis of descaling process in industrial practice is urgently needed. Steel chemistry and minor element impurity levels have both been reported to affect unevenness of scale/steel interface in steels. For example, high residual *Ni* has been reported to hinder scale removability [14]. Difficulties with descaling *Si*-containing steels have been linked to formation of *FeO* - *SiO₂* oxide eutectic (Fayalite) at higher temperatures (1200⁰C and above) [15]. This liquid scale is highly wettable to the steel interface, promoting strong adhesion at the boundary, thereby hindering scale removal.

Hydraulic parameters for descaling are often characterized numerically using a so-called impact factor (IF) which is described as the ratio of the total impact force (I_T) from a spray nozzle to its total coverage area (I_T/A) [10]. Hydraulic parameters such as nozzle height, which affects the impact factor, [10] have been shown to have a strong effect on descaling efficiency [16]. However, there are few studies published that analyze the effect of alloying elements in steels on scale *removability*, and also only limited information on the critical value of impact factor needed to remove scale efficiently.

Inefficiencies during descaling has adverse effects on hot rolling process, with the formation of defects [1] resulting from unremoved residual scale during descaling which affects the final surface quality of the rolled product. A critical look into how specific elements such as *C*, *Mn* and *Si* in steels affects descaling efficiency and how hydraulic parameters can be manipulated to improve scale removability is of much interest to the steel industry.

In this article, a set of experimental laboratory cast steels that included a base medium *C* steel and several steels alloyed by *Si* and *Mn* were examined. The combustion gas atmosphere in industrial reheating furnace was simulated in laboratory reheating tests and a special descaling device based on a CNC controlled mechanism was used to control slab and nozzle displacement to perform hot descaling tests.

2. EXPERIMENTAL PROCEDURES

The composition of the steels used in this study are presented in Table 1. This set of laboratory cast steels included: a base composition with low levels of *C*, *Mn*, and *Si*, a medium *C*, a high *Mn*, and a high *Si* composition. The cast plates were carefully machined to 165 mm x 110 mm x 20 mm to remove the cast surface for this study. Machined samples were finished using wet grinding with 60 grit silicon carbide, the surface quality of the ground sample was measured to have Ra of 0.271 μm using 3D optical profiler (Nanovea, Model PS50 Micro Photonic Inc.). To prevent rusting prior to testing, sample surfaces were preserved by cleaning with ethanol and air drying.

Table 1. Lab Cast steels used in this work (wt. %).

	<i>C</i>	<i>Si</i>	<i>Mn</i>	<i>Al</i>
Base	0.10	0.40	0.45	0.03
<i>Medium C</i>	0.42	0.42	0.43	0.05
<i>High Mn</i>	0.11	0.39	2.00	0.03
<i>High Si</i>	1.12	1.70	0.45	0.05

To simulate industrial scale formation during reheating, the samples were reheated in a 35kw LSZ induction melting furnace (Model LSZ-35), having a 200 mm x 130mm x 25 mm induction chamber which was embedded in an enclosure to allow for control of the furnace atmosphere (Figure 1). The top of the furnace chamber was covered with kaowool during reheating. The furnace was equipped with a multichannel gas mixing system and the gas was delivered to the chamber using a ceramic tube. The atmosphere of the industrial reheating furnace was simulated by mixing gases in proportions that reproduced the natural gas combustion atmosphere in an industrial furnace (Table 2). The composition of gas mixture was controlled using a multi-channel mass flow control system and a controlled temperature water saturation system. An excess oxygen level of 2% was chosen for this study based on observed industrial reheat furnace operating conditions. The gas flow rate supplied to the heating chamber was 6000 ml/min, which provided a 2 cm/sec gas velocity in reaction zone. Calculations confirmed the absence of gas starvation in the reaction zone at this flowrate. The temperature during reheating was controlled by a K-type thermocouple inserted into the slab. The thermocouple enabled adjustment of the furnace power to control the reheating temperature within +/- 10⁰C. The reheating temperature and time employed for the test was 1200⁰C for 90 minutes, which is typical for soak zones temperatures and residence times of industrial reheat furnaces.

At the end of the oxidation period, the sample was carefully removed from the furnace chamber and quickly transported into a descaling chamber to avoid cooling prior to descaling. The hot sample was subjected to hydraulic descaling using high pressurized water. A CNC stage setup was used for descaling (Figure 2) that allowed the standoff

distance from the sample surface to the nozzle to be varied during the descaling process. This approach allowed descaling to be conducted at different spray heights which corresponded to different Impact Factors (*IF*) (N/mm^2). The descaling was conducted at a spray and lead angle of 15° at a flowrate of 4 gpm at 4000 psi and a speed of 0.01 m/s. The standoff distance (*Z* distance of the CNC) was programmed to vary across the length of the sample by decreasing the height of the spray nozzle to cause a corresponding increase in *IF*. The experimental *IF* related to nozzle position was verified using pressure gauges in sponsor facility (Spray System Inc.) and designated in this article as “low *IF*” for $1 \text{ N}/\text{mm}^2$, “medium *IF*” for $1.4 \text{ N}/\text{mm}^2$, and “high *IF*” for $2.2 \text{ N}/\text{mm}^2$. After descaling, the plate was quenched with cold water to prevent the development of secondary scale. The three footprints formed during descaling with varying *IF* were coated with epoxy to preserve the surface for subsequent examination.

Table 2. Industrial reheating conditions simulated in laboratory oxidation.

Combustion gas, vol. %	Temperature, $^\circ\text{C}$	Time, min
8.5 CO_2 , 17 H_2O , 2 O_2 , N_2 bal.	1200	90

A water jet was used to extract rectangular 10 mm x 15 mm x 20 mm samples from the different footprint zones along the length of the sample. A sample with the original formed scale was also extracted from the non-descaled part of the sample for analysis. All extracted samples were cross-sectioned, mounted in epoxy, ground using silicon carbide abrasive papers to 1200 grit and mechanically polished with $0.1 \mu\text{m}$ diamond paste using low polishing pressure to minimize scale breakage. The morphology, thickness, microstructure, and chemistry of the original and residual oxide

layers were analyzed with a scanning electron microscope (SEM) using an TESCAN-ASCAT system equipped with Bruker energy dispersive spectroscopy (EDX).

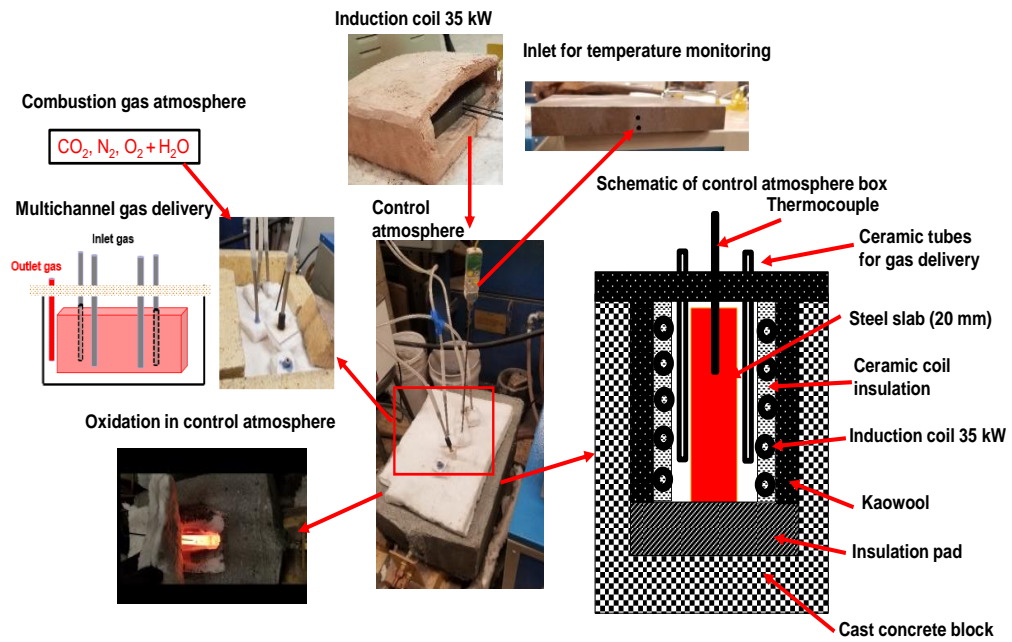


Figure 1. Induction furnace reheating in control atmosphere setup.

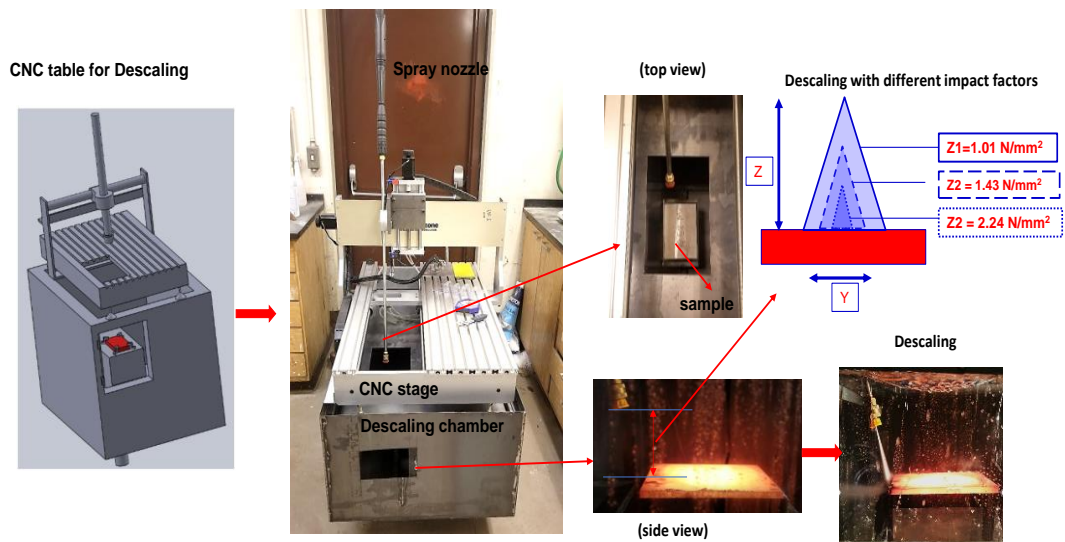


Figure 2. Descaling setup using a CNC stage

A quantitative approach was used to evaluate the descaling efficiency by classifying the descaled surface into 3 structures and measuring the percentage of each structure on cross-sectional samples extracted from the descaled surface. The quantification was done for the entire width of the extracted descaled area (15 mm) by taking SEM images of 20 or more frames at different magnifications between 20 – 100 μm . ImageJ software was used as a measuring tool to quantify the 3 different surface classes.

3. RESULTS

3.1. SCALE FORMED DURING REHEATING

The top row of Figure 3 shows the cross-sectional microstructure of the scale that formed on the base steel having low levels of *C*, *Mn* and *Si* oxidized at 1200⁰C for 90 minutes in a combustion gas atmosphere. The scale structure consisted of an *external layer* (outer and intermediate) growing outward and *internal layer* (inner merged with subsurface) growing inward. The external scale thickness measured between 850 – 1000 μm and the internal scale measure between 45 – 90 μm . The external scale layer was characterized by a continuous dense structure while the internal scale layer saw high levels of porosity between the scale/steel boundary with metal-oxide entanglement. The scale structure in the internal layer was nonuniform and discontinuous in different sections and also showed adhesion to the substrate in some section while other sections showed complete separation from the substrate. EDX chemistry analysis of the oxide scale revealed the external scale layer to contain *Fe*-based oxide and phase identification

with Raman spectroscopy revealed the presence of Fe_2O_3 and Fe_3O_4 phases in this layer. The internal layer contained a mixed chemistry of pure Fe with trace of Cu , Fe -based oxides and $Fe-Si$ based oxides. Phase identification revealed this layer to be a mixed phase of Fe_2SiO_4 and Fe_3O_4 . A randomly scattered dotted layer containing pockets of oxides was also seen to have formed internally and was superimposed on the metal substrate and extended about $30\ \mu m$ deep into the substrate from the scale/steel boundary. The chemistry of that layer showed presence of a mixed $Fe-Si-Mn$ based oxides.

Cross-sectional microstructure of the medium carbon steel (Figure 3 second row) revealed a significantly different structure than that formed on the base steel. The external scale layer measured between $600 - 700\ \mu m$ and the internal scale measured between $25 - 70\ \mu m$. The external layer was a dense scale structure, having transverse cracks running through it. The external layer was partially separated from the internal scale layer. The bottom part of internal scale layer exhibited significant root-like penetration into the metal substrate. Some penetration of the metal substrate by a root-like subsurface layer were as deep as $100\ \mu m$ and appeared to have strong adhesion to the metal substrate. Fe metal was also seen in the internal layer and was randomly distributed across the inner and subsurface layer. Chemistry analysis on the different scale layers revealed similar Fe -based oxide and $Fe-Si$ based oxides in the external and internal scale layers respectively. Raman spectroscopy revealed the external layer to be mostly Fe_2O_3 and Fe_3O_4 phases and the internal layer to be a mixture of Fe_2SiO_4 and Fe_3O_4 phases. This suggested that carbon in steel changed scale morphology (structure and thickness) but did not have an effect on the scale layer chemistry and phases present.

In the case of the high *Si* steel (Figure 3 third row), the scale structure was characterized by randomly distributed voids in the external outer layer through to the internal subsurface scale layer. The external scale layer measured between $1000 - 1200 \mu\text{m}$ in thickness and the internal scale thickness measure between $80 - 190 \mu\text{m}$. The internal layer structure merged with the inner and subsurface oxide structure, with a significant amount of metal entrainment. The internal scale layer was well bonded to the metal substrate and was disconnected from the external layer in some sections, with nonuniformity in that layer. Elemental mapping showed the internal layer to be a *Si*-based oxide layer with some *Fe*-based oxides in it. The internal scale layer was connected to the substrate at the scale/steel boundary. This structure could have resulted from the formation of a low melting temperature (1180°C) fayalite eutectic. Phase identification supported the presence of this phase which can melt during reheating at 1200°C , within a mixture of Fe_2SiO_4 and Fe_3O_4 phases in the inner scale layer.

The high *Mn* steel was characterized (Figure 3, bottom row) by uneven thickness in the external scale layer, which measured between $900 - 1100 \mu\text{m}$. Transverse cracks running from the external layer through to the internal scale layer as well as voids at the external/internal oxide layer boundary were observed. The internal scale layer, which measured between $50 - 80 \mu\text{m}$, was characterized by a multiphase oxide mixture that penetrated into the metal substrate. Metal entrapment in this layer was massive with metal particle sizes of up to $50 \mu\text{m}$. Internally formed oxide pockets below this layer on the substrate was extensive for the high *Mn* steel. The internal scale layer had a coherent structure at the scale/steel boundary. Chemistry analysis of the external scale layer was observed to be pure *Fe* oxide with trace amounts of *Mn*. The internal layer consisted of a

mixed chemistry with the presence of Mn increasing in concentration from the external to the internal interface. Phase analysis of the internal layer (inner and subsurface) identified the presence of Fe_2SiO_4 and Fe_3O_4 phases, while Mn bearing oxides were detected in pockets formed in the subsurface layers. We were not able to identify phases in these small pockets, however thermodynamic simulations predicted the formation of $MnSiO_3$ and Mn_2SiO_4 phases in this subsurface region [6].

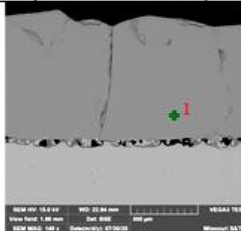
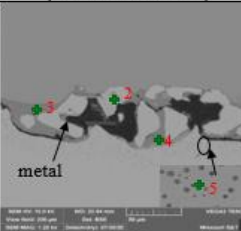
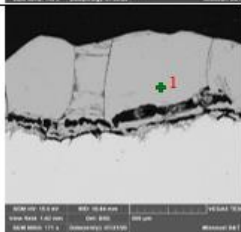
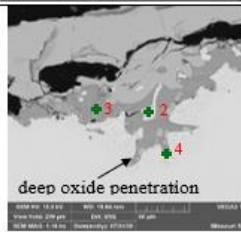
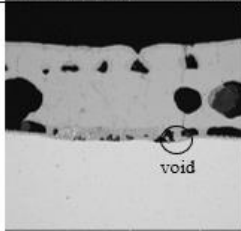
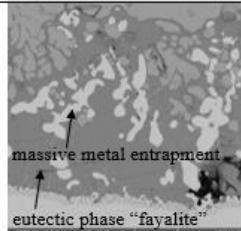
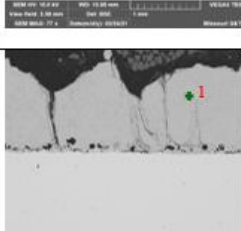

Steel	External layer (outer & intermediate)	Internal layer (inner & subsurface)	Chemistry wt. %																																				
Base			<table border="1"> <thead> <tr> <th></th> <th>Fe</th> <th>O</th> <th>Si</th> <th>Cu</th> <th>Mn</th> </tr> </thead> <tbody> <tr> <td>1:</td> <td>83</td> <td>17</td> <td>-</td> <td>-</td> <td>-</td> </tr> <tr> <td>2:</td> <td>99</td> <td>-</td> <td>-</td> <td>1</td> <td>-</td> </tr> <tr> <td>3:</td> <td>63</td> <td>23</td> <td>13</td> <td>-</td> <td>-</td> </tr> <tr> <td>4:</td> <td>82</td> <td>18</td> <td>-</td> <td>-</td> <td>-</td> </tr> <tr> <td>5:</td> <td>60</td> <td>22</td> <td>10</td> <td>-</td> <td>8</td> </tr> </tbody> </table> <p>Thickness (μm) External: 850 – 1000 Internal: 45 – 90</p>		Fe	O	Si	Cu	Mn	1:	83	17	-	-	-	2:	99	-	-	1	-	3:	63	23	13	-	-	4:	82	18	-	-	-	5:	60	22	10	-	8
	Fe	O	Si	Cu	Mn																																		
1:	83	17	-	-	-																																		
2:	99	-	-	1	-																																		
3:	63	23	13	-	-																																		
4:	82	18	-	-	-																																		
5:	60	22	10	-	8																																		
Medium, C			<table border="1"> <thead> <tr> <th></th> <th>Fe</th> <th>O</th> <th>Si</th> <th>Cu</th> <th>Mn</th> </tr> </thead> <tbody> <tr> <td>1:</td> <td>83</td> <td>18</td> <td>-</td> <td>-</td> <td>-</td> </tr> <tr> <td>2:</td> <td>98</td> <td>-</td> <td>-</td> <td>2</td> <td>-</td> </tr> <tr> <td>3:</td> <td>64</td> <td>24</td> <td>12</td> <td>-</td> <td>-</td> </tr> <tr> <td>4:</td> <td>60</td> <td>25</td> <td>15</td> <td>-</td> <td>-</td> </tr> </tbody> </table> <p>Thickness (μm) External: 600 – 700 Internal: 25 – 70</p>		Fe	O	Si	Cu	Mn	1:	83	18	-	-	-	2:	98	-	-	2	-	3:	64	24	12	-	-	4:	60	25	15	-	-						
	Fe	O	Si	Cu	Mn																																		
1:	83	18	-	-	-																																		
2:	98	-	-	2	-																																		
3:	64	24	12	-	-																																		
4:	60	25	15	-	-																																		
High, Si			<table border="1"> <thead> <tr> <th></th> <th>Fe</th> <th>O</th> <th>Si</th> <th>Cu</th> <th>Mn</th> </tr> </thead> <tbody> <tr> <td>1:</td> <td>81</td> <td>18</td> <td>-</td> <td>-</td> <td>1</td> </tr> <tr> <td>2:</td> <td>100</td> <td>-</td> <td>-</td> <td>-</td> <td>-</td> </tr> <tr> <td>3:</td> <td>61</td> <td>22</td> <td>13</td> <td>-</td> <td>4</td> </tr> <tr> <td>4:</td> <td>81</td> <td>17</td> <td>-</td> <td>-</td> <td>-</td> </tr> <tr> <td>5:</td> <td>58</td> <td>7</td> <td>5</td> <td>-</td> <td>30</td> </tr> </tbody> </table> <p>Thickness (μm) External: 1000 – 1200 Internal: 80 – 190</p>		Fe	O	Si	Cu	Mn	1:	81	18	-	-	1	2:	100	-	-	-	-	3:	61	22	13	-	4	4:	81	17	-	-	-	5:	58	7	5	-	30
	Fe	O	Si	Cu	Mn																																		
1:	81	18	-	-	1																																		
2:	100	-	-	-	-																																		
3:	61	22	13	-	4																																		
4:	81	17	-	-	-																																		
5:	58	7	5	-	30																																		
High, Mn			<table border="1"> <thead> <tr> <th></th> <th>Fe</th> <th>O</th> <th>Si</th> <th>Cu</th> <th>Mn</th> </tr> </thead> <tbody> <tr> <td>1:</td> <td>81</td> <td>18</td> <td>-</td> <td>-</td> <td>1</td> </tr> <tr> <td>2:</td> <td>100</td> <td>-</td> <td>-</td> <td>-</td> <td>-</td> </tr> <tr> <td>3:</td> <td>61</td> <td>22</td> <td>13</td> <td>-</td> <td>4</td> </tr> <tr> <td>4:</td> <td>81</td> <td>17</td> <td>-</td> <td>-</td> <td>-</td> </tr> <tr> <td>5:</td> <td>58</td> <td>7</td> <td>5</td> <td>-</td> <td>30</td> </tr> </tbody> </table> <p>Thickness (μm) External: 900 – 1100 Internal: 50 – 80</p>		Fe	O	Si	Cu	Mn	1:	81	18	-	-	1	2:	100	-	-	-	-	3:	61	22	13	-	4	4:	81	17	-	-	-	5:	58	7	5	-	30
	Fe	O	Si	Cu	Mn																																		
1:	81	18	-	-	1																																		
2:	100	-	-	-	-																																		
3:	61	22	13	-	4																																		
4:	81	17	-	-	-																																		
5:	58	7	5	-	30																																		

Figure 3. Cross-sectional BSE image and chemistry of scale structures present in steels reheated at 12000C before descaling.

3.2. CLASSIFICATION OF DESCALED SURFACE QUALITY

Reheated steels were subjected to water jet descaling with variations in the *IF*. To obtain quantitative data from these experiments, the quality of the descaled surfaces was grouped into three surfaces classes (Figure 4):

- class A had a completely removed external, complex internal and subsurface oxide.
- class B had a completely removed external layer and partially removed internal (inner and subsurface) scale layer, particularly, with presence of the Fe_2SiO_4 phase, and
- class C had complete removal of the external and internal (inner scale) layers but contained penetrating subsurface oxide with root-like scale structure having metal entrainment.

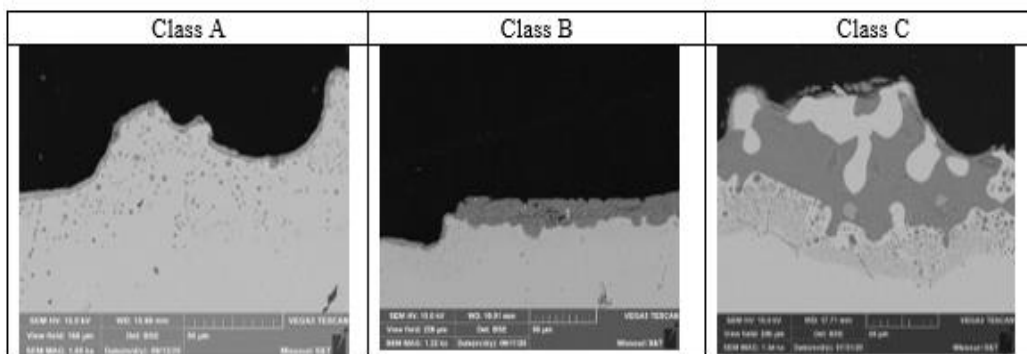


Figure 4. Descaled surface classification.

3.3. DESCALING EFFICIENCY

Analysis and quantification of the surface quality of the descaled base steel composition showed significant difference in efficiency with varying *IF* (Figure 5). It was observed that the low *IF* condition demonstrated complete removal of the external (*Fe*-oxides) and partial removal of the internal (mixed *Fe-Si* based oxides) scale layers,

making up 70% of clean surface quality class A and 30% class B plus C. The residual scale (class B and C) contained partially removed internal oxide layer (inner and subsurface). Increasing *IF* to the medium condition showed a decrease in the residual scale from 30% to 12% particularly for class B, with a corresponding increase in the clean surface (Class A). The residual scale thickness also decreased from 5-12 μm range to 3-5 μm . The residual scale, particularly for the remained class C, consisted of consolidated oxides between entrapped metal particles in the subsurface layer. At the highest *IF condition*, a significant amount of the residual scale was removed and replaced by secondary iron oxide scale that formed after the descaling process. Some of the scale formed within metal crevices where removed and secondary oxides formed in its place. The clean surface quality was quantified to be 94% with the residual scale making up the remaining 6% of which was class C type scale structures. The thickness of the residual scale was less than 5 μm .

The medium carbon steel was characterized by deep penetration of internal scale layers (inner and subsurface) into the metal matrix (Figure 3). Descaling at the low *IF* condition exhibited complete removal of the external and partial removal of both classes of internal scale layers (class B and penetrated subsurface class C) (Figure 6). Residual scale thickness after descaling measured up to 20 μm in thickness. Quantification of the surface quality revealed that almost 50% of the residual scale (class B and C), which consisted of Fe_2SiO_4 and Fe_3O_4 oxide phases, remained on the surface at the low *IF condition*. These residual oxides were well connected to the substrate due to the massive root-like oxide penetration seen in the subsurface for this steel chemistry.

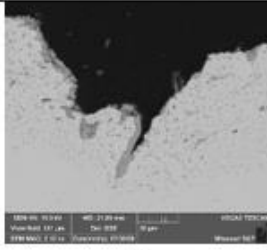


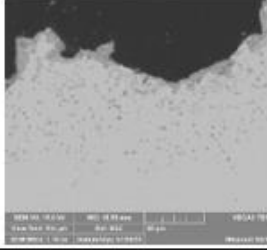
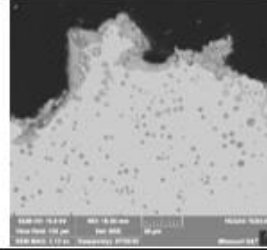

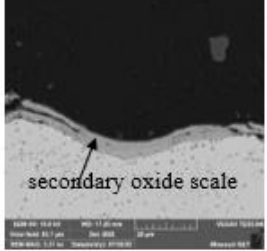
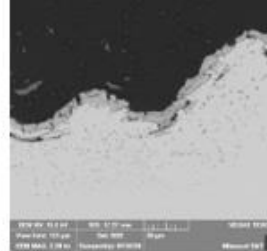

<i>IF</i>	Class A	Class B	Class C
Low		 partially removed internal	 adherent residual
%	70	14	16
Medium			 oxide beneath entrapped
%	88	5	7
High	 secondary oxide scale		 removed oxide in
%	94	2	4

Figure 5. Surface quality of base steel after descaling at different *IF*.

At the medium *IF condition*, there was a significant decrease in the amount of residual scale, particularly for surface class B which did not contain deep penetration and a less complex structure than that of surface class C. The thickness of the residual scale for this *IF* decreased to about 13 μm and accounted for 25% of the quantified surface coverage, while the clean surface Class A accounted for 75% of the coverage. It was observed that most of the oxide penetration (class C) had different orientations: vertical, horizontal, and twisted geometry with different angles of penetration. The majority of the residual scale class C consisted of complex oxides. At the high *IF condition*, it was

observed that the complex oxides with penetration were partially removed. Oxide penetration with a vertical orientation was removed while with the twisted and slanted orientations were only partially removed. At this *IF condition*, the residual scale consisted predominantly of surface class C (12%) with the scale thickness measuring up to about 10 μm . Near 85% of the surface was quantified as clean (class A).

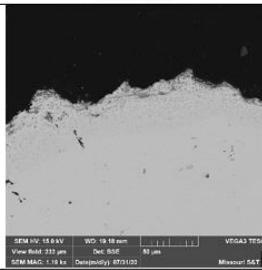
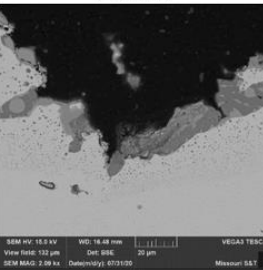
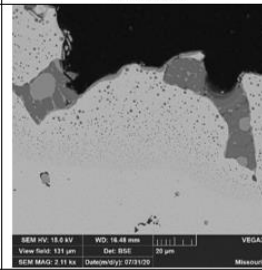
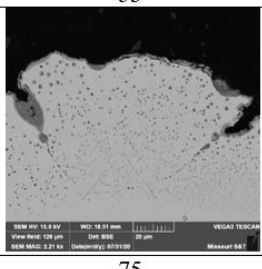
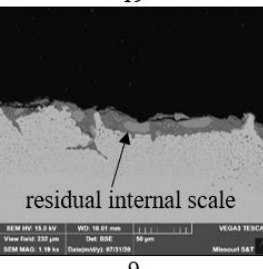
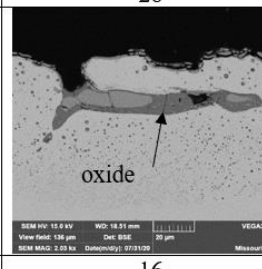
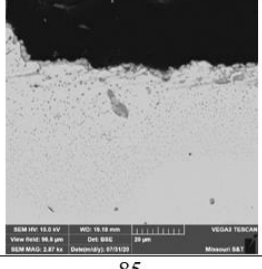
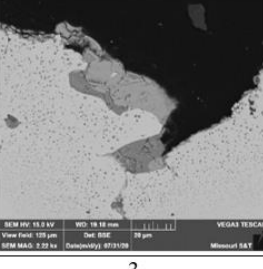
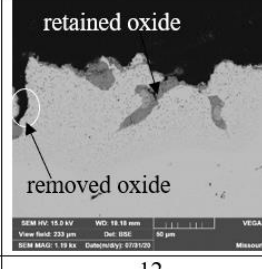
<i>IF</i>	Class A	Class B	Class C
Low			
%	53	19	28
Medium			
%	75	9	16
High			
%	85	3	12

Figure 6. Surface quality of medium *C* steel after descaling at different *IF*.

Characterization of the original scale structure prior to descaling demonstrated a complex mechanism of internal scale formation including possible liquid fayalite

formation (Figure 3) in the high *Si* steel. The internal layer was also uneven due to a significant amount of porosity and voids in the internal scale layers and had scale thickness measurements as high as 190 μm and as low as 80 μm . At the low *IF condition*, only 34% of the quantified surface quality was completely removed (class A) (Figure 7). The remaining scale was a mixture of surface class B (27%) and C (39%). The residual scale measured up to 85 μm in thickness, which was about half of the original internal scale layer thickness. At the medium *IF condition*, there was no significant change in the percentage of clean surface class A as was seen in the base and medium *C* steel. The residual scale measured up to about 50% with a 9% decrease in class B scale residue (from 27 to 18%) and 5% decrease in class C (from 39 to 34%). The residual scale was characterized by a mixed fayalite and entrained metal layers showing strong attachment to the substrate. At the highest *IF condition*, the quantified surface quality did not show any significant improvement from the previous medium *IF*. The total clean surface at this point was 53% and the residual scale 47% (17% class B and 30% class C).

The majority of the residual scale was made up of class C which was almost twice of the amount observed in class B. Observations of the residual scale revealed that some residual scales were strongly attached to the underside of the entrained layer of metal, making it difficult to remove since direct contact with the impinging water pressure during descaling was blocked. The residual scale measured up to about 60 μm in thickness, which was a 15 μm decrease from the first *IF* condition of 1.0 N/mm^2 . Overall, the high *Si* steel showed significant resistance to descaling, as evident from its high levels of quantified residual scale percentages and this can be attributed to the complexity of the formed oxide in the internal scale layers of this steel.

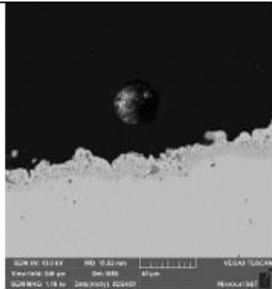
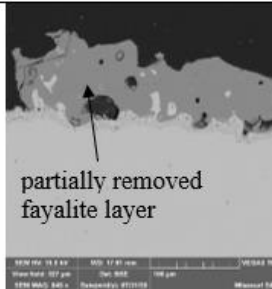
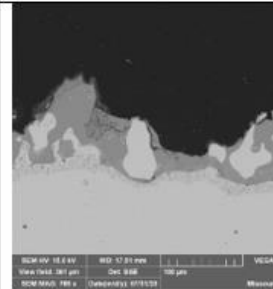
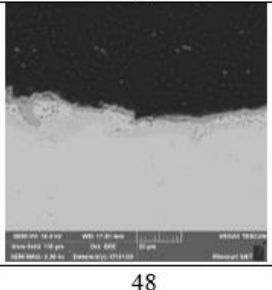
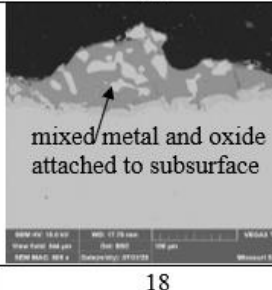
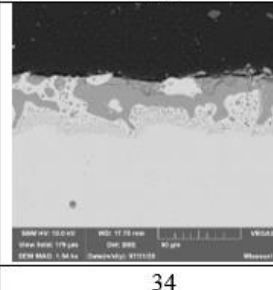
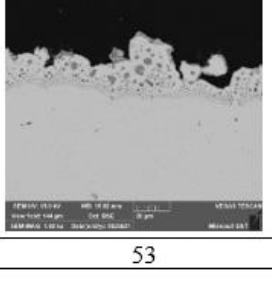
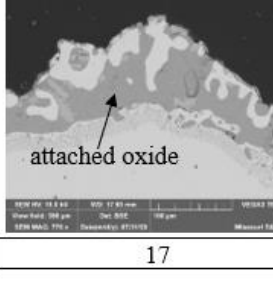
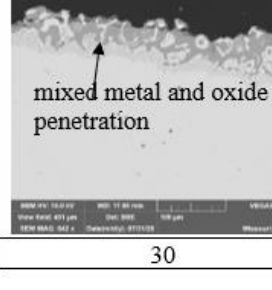
IF	Class A	Class B	Class C
Low			
%	34	27	39
Medium			
%	48	18	34
High			
%	53	17	30

Figure 7. Surface quality of high *Si* steel after descaling at different *IF*.

Similar to the high *Si* steels, the high *Mn* steel showed a lower descaling efficiency (Figure 8). The original scale structure of the high *Mn* steel was characterized by large amount of metal entrapment and penetration of the subsurface internal oxide layer into the matrix (Figure 3). The residual scale measured at low *IF* decreased from 70% to 40% at the highest *IF*. There was a gradual improvement in the residual class A quantified surface percentage as it increased from 30% to 60% at the highest *IF*. The residual scale (class B and C) was characterized by oxide penetration into the metal matrix as well as an adherent Fe_2SiO_4 oxide phase which exhibited a strong connection at

the scale/steel boundary in the internal scale layer. The residual scale thickness measured after descaling with the low IF condition decreased from about 40 μm to about 20 μm when the highest IF condition was applied. Surface class C was the predominant residual scale type, having penetration extending 50 μm into the substrate from the oxide/steel interfacial boundary.

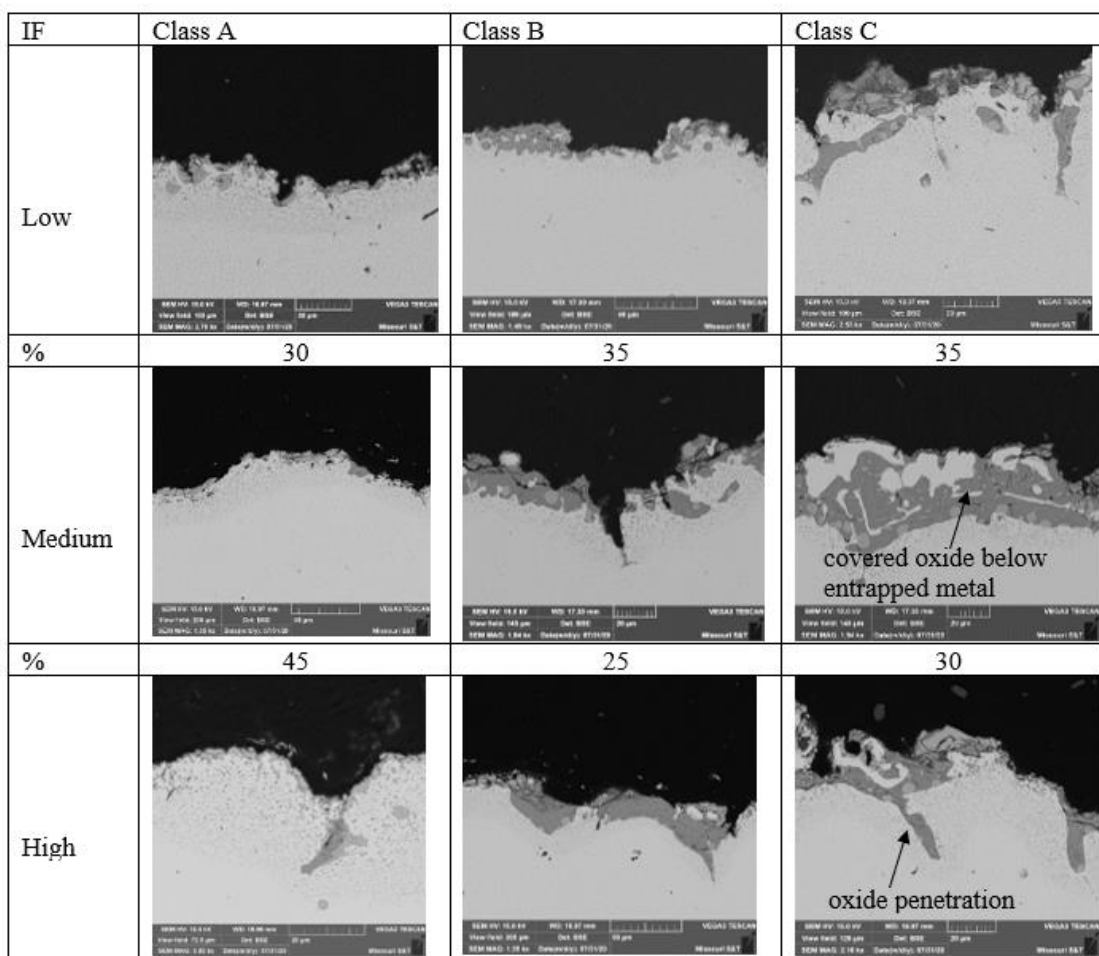


Figure 8. Surface quality of High Mn steel after descaling at different IF .

4. DISCUSSION

The testing methodology based on our CNC controlled descaling process allowed us to change the *IF* testing conditions on a single test sample and to obtain descaling test results, while minimizing possible errors associated with using multiple test samples. The effect of impact factor on descaling efficiency for the different steel grades tested is presented in Figure 9. It was observed that a critical *IF* condition between medium (1.4 N/mm²) and high (2.2 N/mm²) was enough to descale the baseline steel sample and that the residual remaining scale coverage was about 6% for surface classes B and C, with the clean surface class A percentage measuring 94%. In the case of the medium *C* steel, the critical high *IF* condition was just enough to remove close to 90% of formed scale. However, residual scale class C with metal substrate oxide penetration was the predominant residual scale type and other scale removal approaches, such, repeated descaling may be needed for its removal. For the high alloy steels (*Mn* and *Si*), it was observed that, the critical *IF* condition required for greater than 90% efficiency was above studied 2.2 N/mm², as the residuals in these steels contained high percentages of both surface class B and C and had significant remaining oxide thickness (Figure 10).

Comparison of the residual scale (class B and C) remaining after descaling indicated a decrease in thickness with increasing *IF* (Figure 10). The high *Si* steel retained the highest residual scale thickness (60 μm) after descaling for the highest studied *IF* condition of 2.2 N/mm², followed by the high *Mn* steel (18 μm), while the medium *C* and base steels were both below 10 μm in thickness. This result indicates that major alloying elements (*Mn* and *Si*) play a strong role in decreasing descaling

efficiency and this role can be attributed to the complexity of oxide scale interface structures formed on these steels when reheated in a combustion gas atmosphere.

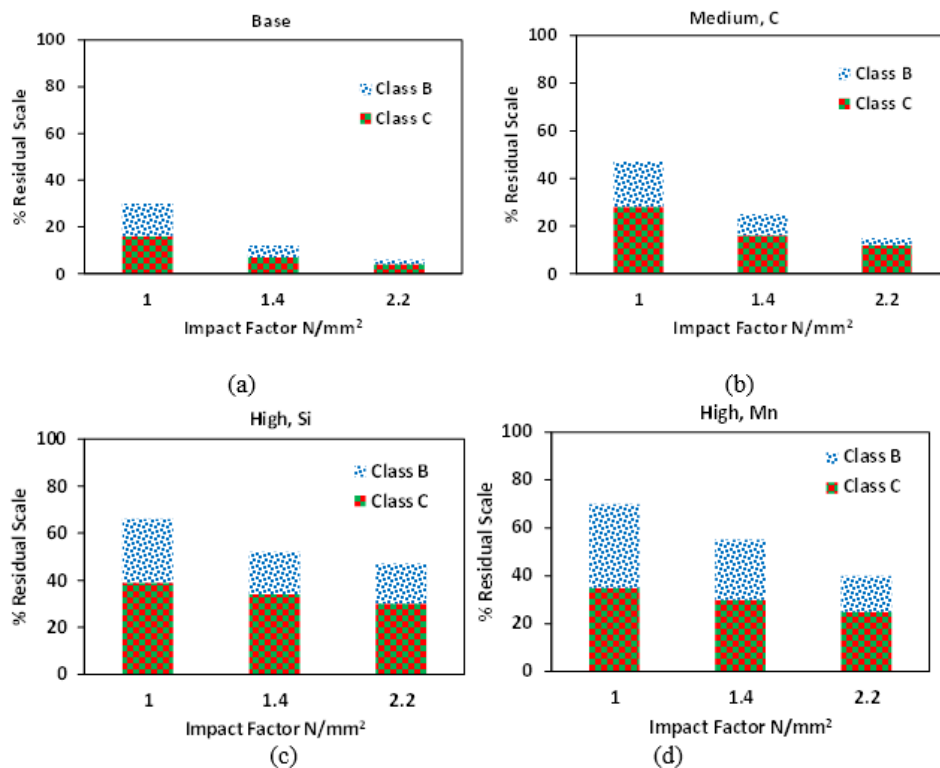


Figure 9. Effect of IF on descaling efficiency of: (a) base, (b) medium C , (c) high Si , and (d) high Mn steels.

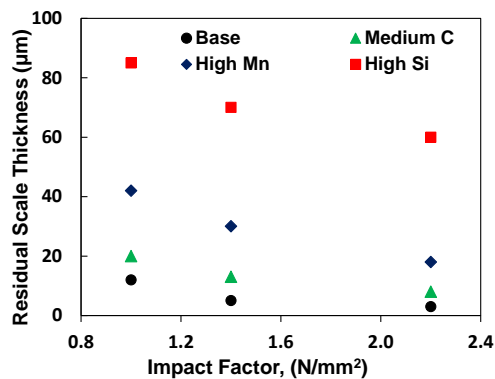


Figure 10. Effect of IF on residual scale thickness after descaling for the different steel grades.

5. CONCLUSIONS

Scale formation during reheating in combustion atmosphere followed by descaling was studied using four laboratory cast steel grades, including a low and medium *C steel with low residuals* and two highly alloyed *Si* and *Mn steels*. The sample descaling efficiencies were assessed using three water jet descaling impact factors (low, medium, and high IF). The scale structures formed on these steels during reheating exhibited distinctly different chemistries and morphologies (thicknesses, topology, and uniformity) in their internal and external layers. The methodology to quantify descaling efficiency based on percent coverage for three defined categories of residual scale structure was proposed. Descaling tests showed that the structure of internal layer and deeply penetrated oxide features into metal matrix sublayer are the most important factors influencing scale removability. Scale formed on the medium *C* steels had oxide penetration which affected its descaling efficiency. Residual scale structures observed after descaling contained root-like penetrating oxides. For the case of alloyed steels, the high *Si* steel was characterized by an adherent fayalite phase with significant metal entrainment and this layer showed a high resistance to descaling. The *Mn* steel also contained root-like penetrating oxides and entrained metal that was strongly attached to the subsurface scale which hindered direct contact with the impinging water pressure during descaling and hence resulted in a lower efficiency.

Other factors such as internal scale thickness and defect formation in the scale structure accounted for the lower descaling efficiency in the alloyed steels. The critical *IF* conditions required for the efficient scale removal for the alloyed steels were determined

to be above 2.2 N/mm², while between 1.4 to 2.2 N/mm² was enough to achieve efficient scale removal for the base and medium *C* steels.

ACKNOWLEDGEMENTS

This study is supported by Kent Peaslee Steel Manufacturing Research Center, and the authors gratefully acknowledges the support and guidance from the industry advisory committee of Peaslee Steel Manufacturing Research Center.

REFERENCES

- [1] S. Lechwar, L. Rauch and M. Pietrzyk, “Use of Artificial Intelligence in Classification of Mill Scale Defects”, *Steel Research Int.*, 2015, Vol. 86, No. 3, pp. 266-277
- [2] Y. Yu and J.G. Lenard, “Estimating the Resistance to Deformation of the Layer of Scale during Hot Rolling of Carbons Steel Strips”, *Journal of Materials Processing Technology*, 2002, Vol. 121, pp. 60-68
- [3]. D.B Wei, J.X. Haung, A.w. Zhang, Z.Y. Jiang, A.K. Tieu, X. Shi, and S.H. Jiao, “The Effect of Oxide Scale of Stainless Steels on Friction and Surface Roughness in Hot Rolling”, *Wear*, 2011, Vol. 271, pp. 2417-2425
- [4]. O. A. Zambrano, J.J. Coronado, and S. A. Rodriguez, “Mechanical Properties and Phases Determination of Low Carbon Steel Oxide Scales formed at 1200 °C in Air”, *Surface and Coating Technology* 2015, Vol. 282, pp. 155-162
- [5]. R. Osei, S. N. Lekakh, and R. J. O’Malley, “Scale Formation on 430 Stainless Steel in a Simulated Slab Combustion Reheat Furnace Atmosphere” *AISTech Proceedings*, 2020, pp. 1126-1137
- [6]. R. Osei, S. N. Lekakh, and R. J. O’Malley, “Thermodynamic Prediction and Experimental Verification of Multiphase Composition of Scale Formed on Reheated Alloy Steels”, *Met Trans B*, 2021, Vol. 52, pp. 393-404

- [7]. W. Sun, "A study on the Characteristics of Oxide Scale in Hot Rolling of Steel", PhD Thesis, School of Mechanical, Materials and Mechatronic Engineering, University of Wollongong, 2005
- [8]. J.S. Sheasby, W.E. Boggs, and E.T. Turkdogan, "Scale Growth on Steel at 1200°C: Rationale of Rate and Morphology", *Met. Sci.* 1984, Vol.18, pp. 127-136
- [9]. J. Frick, "Optimization of Nozzle Arrangements on Descaling Headers", 4th International Conference on Hydraulic Descaling, London UK, 2003
- [10]. R. Lesli, "Effect of Spray Height, Lead Angle and Offset Angle on Impact" AISTech, 2005
- [11]. J.W. Frick, "More Efficient Hydraulic Descaling Header Designs", *Metallurgical Plant and Technology International*, 2004, Vol. 27, No. 2, pp. 90-92
- [12]. M. Hnizdil, and M. Raudensky, "Descaling by Pulsating Water Jet", *Metals*, 2010, Vol. 5, 6 pp.
- [13]. H. Votavova, and M. Pohanka, "Study of Water Collision of High-Pressure Flat Jet Nozzles for Hydraulic Descaling" *Applied Mechanics and Materials*, 2015, Vol. 821, pp. 152-158
- [14]. T. Asai, T. Soshiroda and M. Miyahara, "Influence of Ni Impurity in Steel on the Removability of Primary Scale in Hydraulic Descaling", *ISIJ International*, 1997, Vol. 37, No. 3, pp. 272-277
- [15]. P.C. Pistorius, N.-A. Quagraine, and C. Coetzee, "Descaling Behaviors of Stainless Steel following Simulated Reheating", *The Journal of The South African Institute of Mining and Metallurgy*, 2003, pp. 607-615
- [16]. P. Kotrbacek, J. Horsky, M. Raudensky and M. Pohanka, "Influence of Parameters of Hydraulic Descaling on Temperature Losses and Surface Quality of Rolled Material", *Suppl. Metal Forming*, 2004, pp. 367-370

V. EFFECT OF *CU* ADDITIONS ON SCALE STRUCTURE AND DESCALING EFFICIENCY OF LOW *C* STEEL REHEATED IN A COMBUSTION GAS ATMOSPHERE

Richard Osei¹, Simon Lekakh¹, Ronald O'Malley¹,

¹Peaslee Steel Manufacturing Research Center, Department of Materials Science and Engineering, Missouri University of Science and Technology, Rolla, MO, USA, 65409

ABSTRACT

Modern EAF steelmaking employs scrap as its primary source of raw material. Different sources of scrap have varying levels of residuals, which can negatively influence product properties, performance, and surface quality. The presence of some residuals, such as *Cu* and *Ni* in controlled quantities, can also positively impact steel performance for some applications. It is also well known that interactions between residuals and alloying elements in steel can modify the structure of scale formed during slab reheating prior to hot rolling. These changes in the scale structure can influence scale removability. In this study, the effect of varying *Cu* concentrations in a low alloyed *Mn* and *Si* containing steel was examined to investigate its impact on scale removability. Laboratory studies were performed with simulated reheating and descaling conditions that mimic the conditions used in industrial practices. The scale structure that formed during reheating in the combustion atmosphere was investigated using SEM/EDX analysis. A special laboratory water jet descaling device was used to evaluate scale removability at three different hydraulic impact factors. The results showed that *Cu* at different levels significantly modified scale structure that formed, particularly the internal

scale layers, which affected scale removability at different applied descaling impact factors. The effects of *Cu* level and descaling impact factor on scale removability is discussed.

Keywords: reheating, *Cu*-enrichment, descaling, scale structure, impact factor

1. INTRODUCTION

Steel production has evolved through the 19th century to the 21st century with raw materials increasingly switching from primarily pig iron to scrap [1-3]. Today in the US, over 70% of the steel is produced in electric arc furnaces (EAF) using large proportions of recycled steel scrap as the primary charge material due to its economic advantages and environmental friendliness [4,5]. However, scrap melting to produce steel has a major challenge due to the accumulation of high levels of residuals in the continually recycled scrap stream [6,7]. These residuals in scrap (*Cu*, *Ni*, *Sn*, *Sb*, *Pb*, *As*) remain in the steel during the steelmaking process because they cannot be preferentially oxidized and captured in the slag phase during melting[8]. The presence of these residual cause challenges in the downstream processing of the steel. A commonly known residual is *Cu*, which has been reported to be present in the highest amounts and poses significant challenge in steel manufacture [6, 7,9]. Even though some studies have shown that *Cu* can improves the corrosion resistance and increase the strength of steel [10-13], its presence often causes problems during mechanical working at high temperatures, a phenomena know as *Cu* surface hot shortness in steels [14-17].

The surface hot shortness phenomena have been examined intensively in various studies to explain the mechanisms of damage [18-22]. Cu hot short defects are mostly commonly observed in processes downstream of reheating during the hot roll of slabs or the forming of steel products. During reheating, the cast slab surfaces is exposed to a complex, oxidizing combustion gas atmospheres (CO_2 , O_2 , H_2O , N_2) at temperatures above $1100^{\circ}C$. During such reheating, iron readily oxidized to form scale. *Cu* having a limited solubility in solid iron and a low affinity for oxide formation gets enriched at the oxide/metal interface as the Fe oxidizes. The enrichment of *Cu* at the oxide/metal interface rapidly reaches saturation and forms a liquid phase due its low melting point at $1085^{\circ}C$. the *Cu-liquid* phase then wets and penetrates the austenite grain boundaries, leading to liquid embrittlement and providing a path for oxygen penetration which causes cracking during hot rolling [15]. The presence of surface cracks is undesirable in steel making.

Different approaches have been adopted to suppress this defects in steel. Most steel produces resort metallic charge management to control *Cu* levels in steel by using low residual scrap and blending with virgin iron units such as direct reduced iron (DRI) or pig iron to dilute *Cu* levels in liquid steel. Another suggested approach is the addition of *Ni* to increase the melting point of the precipitated Cu-Ni phase so that it exceeds the reheating temperature and liquid is avoided. In addition, Ni also increases the solubility of *Cu* in austenite [23,24]. Other studies have reported that, reheating of slabs at extreme temperatures above $1200^{\circ}C$ decreased surface hot shortness [22]. However, it has been reported that the presence of tramp elements like *Sn* in low amounts up to 0.04 wt.% increases the severity of surface hot shortness by decreasing solubility of *Cu* at reheating

temperatures in austenite and by lowering the melting temperature of the precipitated Cu-Sn phase [22, 24], thereby decreasing temperature at which liquid can form and austenite grain boundary wetting can occur.

Most studies on residual *Cu* in steel have been focused on reheating, and mechanical deformation by hot rolling to report the mechanisms and effects associated with *Cu* residuals in steels. However, a critical intermediate descaling step between reheating and hot rolling has not been fully investigated. This descaling step involves the removal of the scale that forms on slabs during reheating, generally by hydraulic decaling means using water pressures as high as 4000 psi. This process is a critical step which helps to improve surface quality of rolled steel and reduce defect formation associated with rolled on scale. The descaling step may be carried out in different stages: primary and secondary with 3 or more descaling steps in extreme cases for certain steels. The major challenge associated with scale removal by descaling can be grouped into three groups of factors: (i) oxide structure, (ii) nozzle design, and (iii) hydraulic parameters [25-29]. In the cases of steel chemistry, reports [30] have shown how different elements present in steel (*C*, *Mn*, *Si*) influence the structure of the oxide scale, particularly in the subsurface region, and its corresponding effect on scale removability. Residual elements like *Ni* have also been reported to modify the structure of the oxide/steel interface, increasing unevenness, and decreasing scale removability [7, 31]. However, *Cu* residuals, known to cause surface hot shortness in steel, has not been investigated in relation to its effect on scale removability and this knowledge could be important to steel producers.

The objective of this study was to evaluate of effect of different levels of *Cu* in a low carbon steel on the scale structure that forms during reheating and its effect on scale

removal efficiency. Industrial reheating conditions with a combustion gas atmosphere were simulated in the laboratory and scale formation was followed by descaling using a specially designed high precision CNC descaling device that allows descaling with varied impact factor to be performed

2. EXPERIMENTAL

The composition of the steels used in this study are presented in Table 1. This set of laboratory cast low carbon steels varied in *Cu* content, which were labeled as low, medium, and high *Cu*. The cast plates were carefully machined to 165 mm x 110 mm x 20 mm rectangular samples to remove the cast surface. Machined samples were finished using wet grinding with 60 grit silicon carbide and the surface quality of the ground sample was measured to have Ra of 0.271 μm using 3D optical profiler (Nanovea, Model PS50 Micro Photonic Inc.). To prevent rusting prior to testing, sample surfaces were preserved by cleaning with ethanol and air drying.

Table 1. Lab cast steels used in this work (wt. %).

Steel	<i>C</i>	<i>Si</i>	<i>Mn</i>	<i>Cu</i>
Low <i>Cu</i>	0.13	0.30	0.36	0.24
Medium <i>Cu</i>	0.11	0.28	0.34	0.54
High <i>Cu</i>	0.13	0.29	0.33	0.80

To simulate industrial scale formation during reheating, the samples were reheated in a 35kw induction melting furnace (Model LSZ-35), having a 200 mm x 130mm x 25 mm induction chamber, which was embedded in an enclosure to allow for

control of the furnace atmosphere (Figure 1). The atmosphere of the industrial reheating furnace was simulated by mixing gases in proportions that reproduced the natural gas combustion atmosphere in an industrial furnace (Table 2). An excess oxygen level of 2% was chosen for this study based on observed industrial reheat furnace operating conditions. The gas flow rate supplied to the heating chamber was 6000 ml/min, which provided approximately a 2 cm/sec gas velocity in the reaction zone. Calculations confirmed the absence of gas starvation in the reaction zone at this flowrate. The temperature during reheating was controlled by a K-type thermocouple inserted into the slab. The thermocouple enabled adjustment of the furnace power to control the reheating temperature within $\pm 10^{\circ}\text{C}$. The reheating temperature and time employed for the test was 1200°C for 90 minutes, which is typical for soak zones temperatures and residence times of industrial reheat furnaces.

Table 2. Reheating industrial conditions, which were simulated in laboratory tests.

Combustion gas, vol. %	Temperature, $^{\circ}\text{C}$	Time, min
8.5 CO_2 , 17 H_2O , 2 O_2 , N_2 bal.	1200	90

At the end of the reheating period, the sample was carefully removed from the furnace chamber and quickly transported into a descaling chamber to minimize cooling prior to descaling. The hot sample was subjected to hydraulic descaling using high pressurized water. A CNC stage setup was used for descaling (Figure 2) that allowed the standoff distance from the sample surface to the nozzle to be varied during the descaling process. A detailed description of used setup was provided in a previously published article [30]. This approach allowed descaling to be conducted at different spray heights

which corresponded to different Impact Factors (IF) (N/mm^2). The descaling was conducted at a spray lead angle of 15° at a flowrate of 4 gpm at 4000 psi and a steel speed of 0.01 m/s. The standoff distance Z distance between spray nozzle and slab surface was programmed to vary across the slab length by decreasing the height of the spray nozzle to cause a corresponding increase in IF . The experimental IF related to nozzle position was verified using pressure gauges in a sponsor facility (Spray System Inc.) [30] and designated in this article as “low IF ” for $1 N/mm^2$, “medium IF ” for $1.4 N/mm^2$, and “high IF ” for $2.2 N/mm^2$. After descaling, the plate was quenched with cold water to prevent the development of secondary scale. The three footprint areas formed during descaling with varying IF (Figure 2c) were coated with epoxy to preserve the surface for subsequent examination.

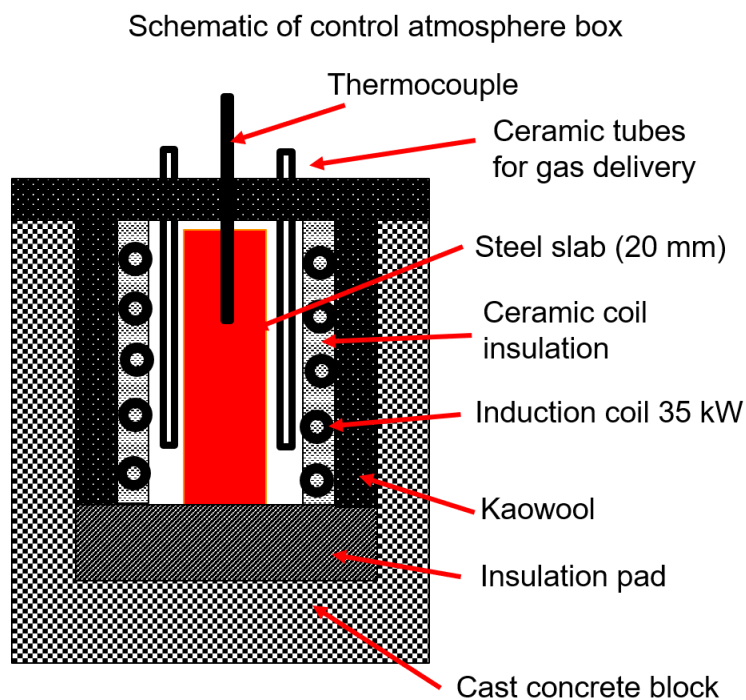


Figure 1. Induction furnace reheating steel slab in control atmosphere.

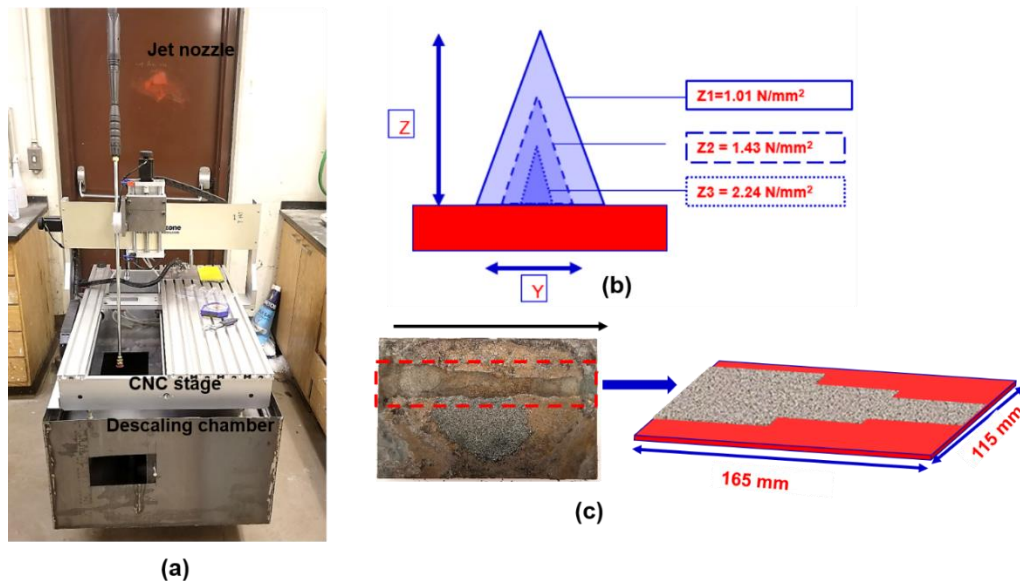


Figure 2. Descaling setup using a CNC stage: (a) CNC stage with jet nozzle, (b) variation in impact factor, and (c) footprint of descaled slab

After the descaling experiment, a Maxiém CNC waterjet with fine abrasive (Model OMAX 0707) was used to extract rectangular 10 mm x 15 mm x 20 mm samples from the different footprint zones along the length of the sample. A sample with the original formed scale was also extracted from the non-descaled part of the reheated slab for analysis. All extracted samples were cross sectioned with high precision wet abrasive cutting slow speed saw, mounted in epoxy, ground using silicon carbide abrasive papers to 1200 grit and mechanically polished with 0.1 μm diamond paste using low polishing pressure to minimize scale breakage. The morphology, thickness, microstructure, and chemistry of the original and residual oxide layers were analyzed with a scanning electron microscope (SEM TESCAN-ASCAT system equipped with Bruker energy dispersive spectroscopy (EDX). HORIBA Jobin-Yvon Raman spectroscopy (LabRam

ARAMIS) was also used to identify the oxide phases that were present and compared to reported phases in RRUFF database [32].

A quantitative approach was used to evaluate the descaling efficiency by classifying the descaled surface into 3 categories of residual scale structures and measuring the percentage of each structure on cross-sectional samples extracted from the descaled footprint. The quantification was done for the entire width of the extracted descaled area (15 mm) by taking SEM images between 20 – 40 frames at a magnification of 100 μm . ImageJ software was used as a measuring tool to quantify the 3 different surface classes.

3. RESULTS AND DISCUSSION

3.1. CHARACTERIZATION OF SCALE FORMED DURING REHEATING

Figure 3 shows the cross-sectional microstructure of the scale that formed on the low *Cu* steel (Table 1) oxidized at 1200⁰C for 90 minutes in a combustion gas atmosphere. The scale structure consisted of several distinguishing layers. A dense *external layer* with thickness between 600 – 970 μm . This external layer had random long transverse cracks running on the middle of this layer and also lateral cracks running through the whole thickness of this layer. Void formation was observed to be predominant at the bottom of the external scale layer, close to what can be described as complex internal/subsurface layer, which will be referred in this article as the *subsurface layer*. The complex subsurface layer was measured at between 35 – 75 μm in thickness. There was significant detachment, separating the external scale layer from the complex

subsurface layer visible in many sections. However, the strong attachment of these two layers also was observed in some sections. The interface between external scale and subsurface structure contained pores and was structurally uneven.

The subsurface structure contained scattered entrainment of metal having different sizes and orientations. EDX mapping of the scale structure showed the distribution of elements making up the different oxide phases in the scale structure. EDX chemistry analysis of the oxide scale (Table 3) revealed that the external scale layer contained iron oxide with trace presence of *Mn* and *Ni*. The complex subsurface contained a mixed chemistry of metallic *Fe* with trace of *Cu* in entrained islands, *Fe*-based oxides and *Fe-Si* based oxides with trace presence of *Mn*. Actually, in reheated low *Cu* steel, *Cu* seems to stay in solid solution in different oxide phases rather than to be presented as separate high concentration precipitate. A randomly scattered dotted layer in the steel matrix beneath subsurface layer contained micro diameter pockets of oxides. These tiny precipitates were formed internally and were superimposed on the metal substrate, extended about 40 μm deep from the oxide/metal interface. The chemistry of that near spherical precipitates showed a presence of a mixed *Fe-Si-Mn* based oxides with a range of *Si* presence. Phase identification using Raman spectroscopy revealed the external scale to contain Fe_2O_3 and Fe_3O_4 phases, with the Fe_2O_3 located at the outer part of the external scale (about 5 μm) and the Fe_3O_4 located just below that layer through to the mid external scale (Figure 4). The complex subsurface layer contained mainly a mixture of two phases: Fe_2SiO_4 and Fe_3O_4 .

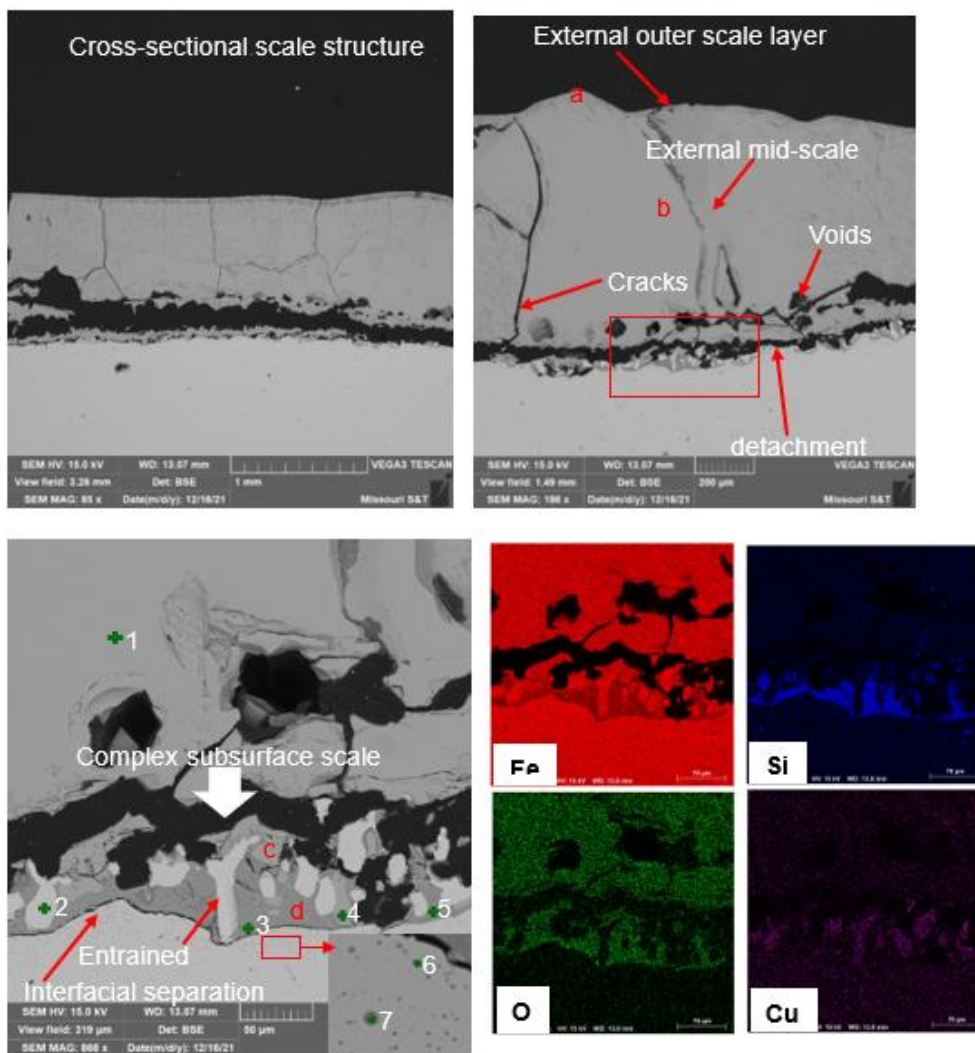


Figure 3. Cross-sectional BSE image of scale structure for low Cu steel: top-left (low magnification), top-right (medium magnification), bottom-left (high-magnification), and bottom-right (EDX elemental map).

Table 3. Oxide scale composition of low Cu steel (wt. %). Points are from Figure 3).

Point	Fe	O	Si	Mn		Cr	Ni	Cu
1	77.0	22.2	-	0.4		-	0.4	-
2	93.6	-	-	-		-	-	6.4
3	63.2	27.5	7.9	1.0		-	0.4	-
4	77.2	22.3	-	0.5		-	-	-
5	59.9	27.2	8.4	1.0		-	0.5	3.0
6	56.5	26.0	5.4	11.3		0.8	-	-
7	29.6	29.2	10.3	30.0		0.5	0.4	-

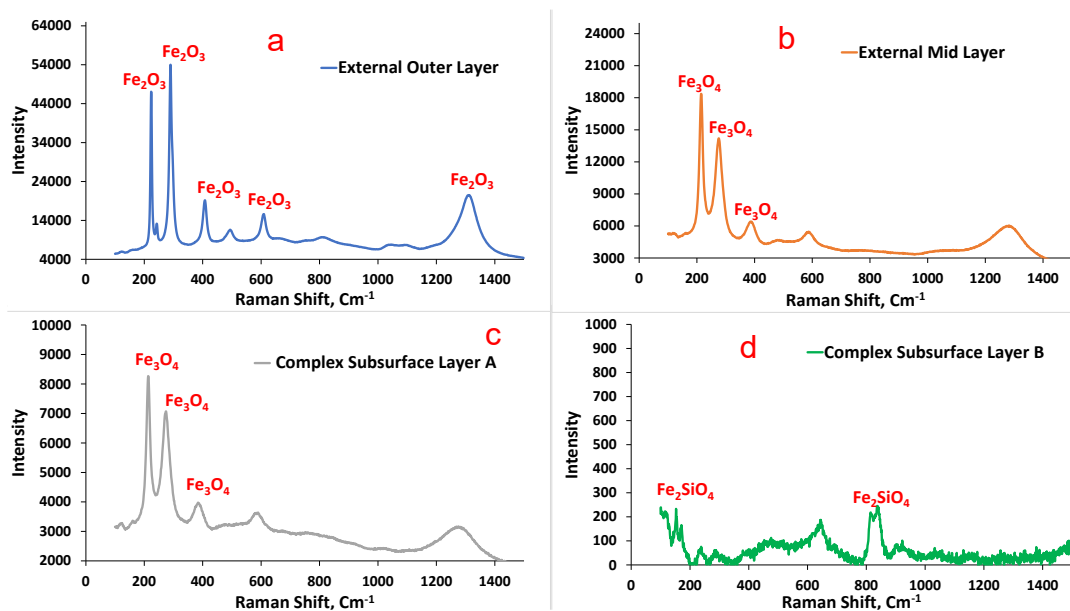


Figure 4. Phases identified in scale using Raman spectroscopy: (a) phases in external outer layer, (b) phases in external mid-scale layer, and phases in complex subsurface layer: (c) in point #4, Figure 3, and (d) in point #5, Figure 3.

The cross-sectional investigation of the reheated medium *Cu* steel (Figure. 5) revealed some similarity to, and also some detectable differences in, scale structure when compared to low *Cu* steel. In both cases, scale consisted of external layer and a merged external/complex subsurface layer. The external scale layer with thickness measured between $320 - 520 \mu\text{m}$ was dense with few internal defects and had vertical cracks. Also, a lateral crack separated portion of the external layer from the merged external/complex subsurface scale layer. In many spots, a lower portion of external layer was merged with subsurface layer forming complex external/subsurface scale layer measured between $65 - 100 \mu\text{m}$ in thickness. A few defects in this complex scale structure contained pores with randomly scattered metal entrainment. The merged external/complex subsurface scale structure appeared to be adherent to the metal substrate with few sections showing partial detachments.

Analysis of the merged external/complex subsurface layer revealed two different types of oxide formations close to the substrate. The first type of oxide formation exhibited 3 layered phases: the first was an iron oxide layer followed by a fayalite layer, and finally by another iron oxide layer. This last bottom iron oxide layer exhibited interfacial separation from the steel matrix in some sections and was bonded to the steel matrix by an enriched liquid *Cu* layer in other sections. The second oxide formation also revealed 3 layered phases: a continuous iron oxide layer about 80 μm in thickness (stemming from the external layer), followed by a eutectic fayalite oxide phase with precipitates of iron oxide (complex subsurface), and finally an enriched liquid *Cu* phase beneath it just on metal matrix boundary. This structure appeared to be strongly adhered to the metal substrate due to the presence of two possible liquid phases (eutectic fayalite and liquid *Cu*) at reheating temperature.

EDX chemistry analysis of the oxide scale (Table 4 in points shown in Figure 5) revealed that the external scale layer contained iron oxide with trace presence of *Mn*. Phase identification revealed the external scale to contain Fe_2O_3 and Fe_3O_4 phases. The merged external/complex subsurface layer contained a mixed chemistry of *Cu-Fe* metal entrainment in the scale structure, *Fe*-based oxides and *Fe-Si* based oxides with trace presence of *Mn*. Phase identification revealed this layer to be a mixed phase of Fe_2SiO_4 and Fe_3O_4 . Possible mechanisms responsible for such complex oxide structural variations and formations are unknown at this point. Further studies are required to fully understand the mechanisms responsible for this type of formation. These structural differences in the low and medium *Cu* alloyed steels could affect descaling efficiency which will be discussed in the next section of this paper.

Table 4. Oxide scale composition of medium *Cu* steel (wt. %). Points are from Figure 5.

Point	<i>Fe</i>	<i>O</i>	<i>Si</i>	<i>Mn</i>	<i>Cr</i>	<i>Ni</i>	<i>Cu</i>
1	77.2	22.3	-	0.4	-	-	-
2	13.9	-	-	-	-	-	85.1
3	61.3	28.2	9.0	1.0	-	-	-
4	6.4	-	-	-	-	0.7	92.4
5	76.4	22.3	-	0.5	0.3	0.3	-
6	6.2	-	-	-	-	0.8	92.7
7	55.8	27.2	7.7	6.6	-	0.4	1.7

The scale formed in reheated high *Cu* steel (Figure 6) was characterized by larger defects in the external scale layers (gaps and voids), transverse cracks and metallic precipitation in the scale structure. The external scale measured between $640 - 920 \mu\text{m}$ in thickness. The defects were non-uniform throughout the scale structure, with some sections showing consistent dense morphology. The external scale layer was laterally separated from the complex subsurface scale layer. The voids in the external scale layer increased inward the external scale structure, close to the external/complex subsurface layer boundary. The complex subsurface scale layer was significantly different compared to the other lower *Cu* steel samples. It had a lower scale thickness ($20 - 40 \mu\text{m}$). The complex subsurface layer was characterized by massive *Cu* precipitation and enrichment at the oxide/metal interface with high unevenness. Few sections were observed to have complex oxides formations. The massive liquid *Cu* phase might have restricted the rapid formation of the complex subsurface oxides when compared to the low and medium *Cu* steels, leading to its lower thickness at the metal interface. However, a much deeper penetration of pure *Cu*-phase, up to about $100 \mu\text{m}$ along the austenite grains boundaries, was observed in the high *Cu* steel. EDX chemistry analysis (Table 5) of the oxide scale revealed the external scale layer to contain iron oxide with trace presence of *Mn* and

entrainment of *Cu* metal having trace presence of *Fe*. The complex subsurface oxide layer contained a mixed chemistry of *Cu-Fe* metal entrainment in the scale structure, *Fe*-based oxides, and *Fe-Si* based oxides (fayalite) with trace presence of *Mn* and *Al*. Elemental mapping showed the distribution of elements in the scale structure at the boundary between the external and complex subsurface (Figure 6).

Table 5. Oxide scale composition of high *Cu* steel (wt. %). Points are from Figure 6.

Point	<i>Fe</i>	<i>O</i>	<i>Si</i>	<i>Mn</i>	<i>Cr</i>	<i>Al</i>	<i>Ni</i>	<i>Cu</i>
1	76.6	22.3	-	0.5	-	-	-	-
2	4.3	-	-	-	-	-	-	95.7
3	61.7	28.0	8.7	1.0	-	-	-	0.6
4	76.8	22.3	-	0.3	-	-	-	-
5	5.9	-	-	-	-	-	-	94.1
6	34.4	32.2	14.3	17.8	-	0.9	-	-

Table 6 summarized findings of the thicknesses of the scale layers formed during reheating of different *Cu*-alloyed steels. There was no general trend, which indicated that multiple mechanisms were at play that are affected by *Cu* addition. Liquid *Cu* films at scale/matrix interface appeared to promote the formation of a thicker and more complex merged internal/subsurface layer in the medium *Cu* steel. However, continued, and deep penetration into austenite grain boundary by the liquid *Cu* film could possibly have suppressed diffusion limited oxidation processes and decreased the thickness of subsurface layer. More importantly, from standpoint of descaling efficiency, a dominated factor could be changes in adhesion between oxide and metal matrix, which will be investigated by varying water jet impact factor.

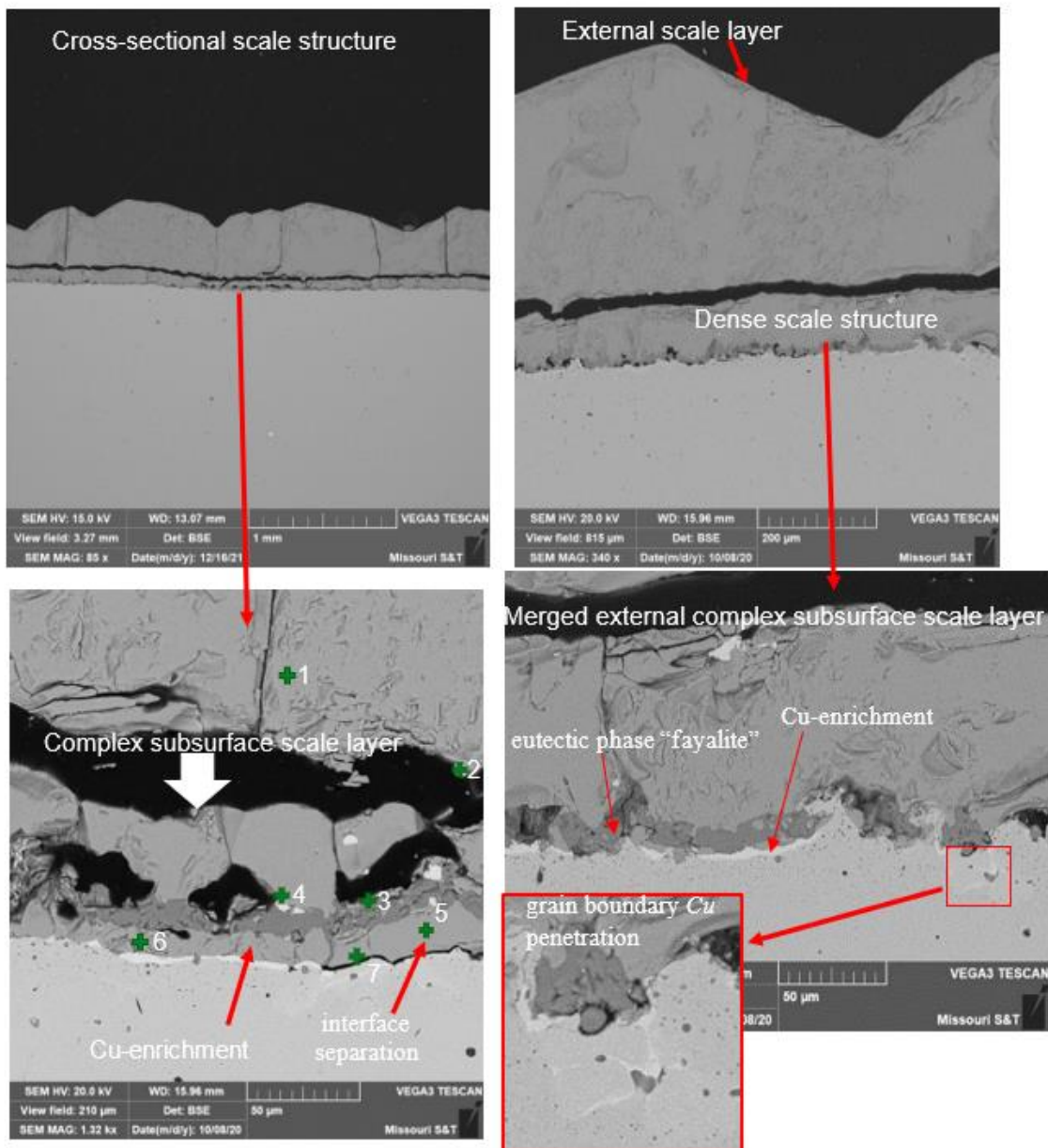


Figure 5. Cross-sectional BSE image of scale structure for medium Cu steel: top-left (low magnification), top-right (medium magnification). Bottom-left and right (high-magnifications) illustrated bonded to the matrix second oxide structure.

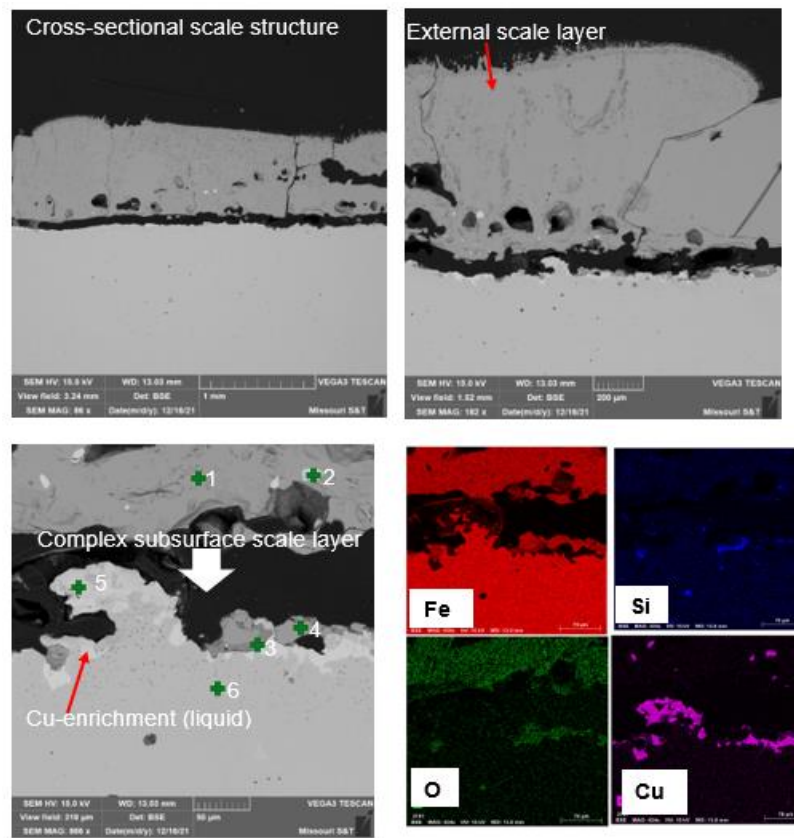


Figure 6. Cross-sectional BSE image of scale structure for high Cu steel: top-left (low magnification), top-right (medium magnification), bottom-left (high-magnification), and bottom-right (elemental map).

Table 6. Comparison of scale thickness (μm) and structure of complex internal/subsurface layer.

Steel	<i>External</i>	<i>Complex Subsurface</i>	<i>Structure Description</i>
Low Cu	600 – 970	35 – 75	scattered metals entrainment in mixed iron oxide/fayalite phase
Medium Cu	320 – 520	66 – 100	two layered oxide formations: (i) iron oxide/fayalite/iron oxide (interfacial separation), and (ii), iron oxide/fayalite/Cu-enrichment (strong adherence to substrate)
High Cu	640 – 920	20 – 40	massive Cu-enrichment with deep grain boundaries penetration, restricted complex oxide formation

3.2. DESCALING EFFICIENCY

Reheated steels were subjected to water jet descaling with variations in the impact factor (IF). To obtain quantitative data from these experiments, the quality of the descaled surfaces was grouped into three surfaces classes (Figure 7):

- class A had a completely removed external and complex subsurface oxides.
- class B had a completely removed external layer and partially removed complex subsurface scale layer, (with presence of the residual Fe_2SiO_4 phase); and
- class C had complete removal of the external layer and some complex subsurface (Fe_2SiO_4) but contained penetrating oxide with root-like scale structure having metal entrainment.

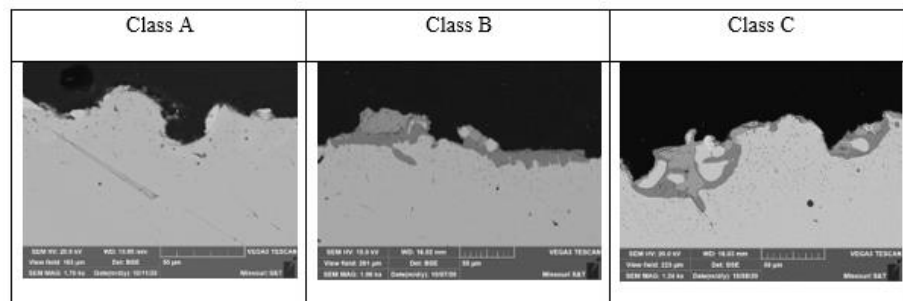


Figure 7. Descaled surface quality classification

After reheating of the low Cu steel, the oxidized sample followed a hot charge descaling schedule on a CNC stage that was programmed to produce three varied standoff distances to cause a corresponding change in applied nozzle impact factor (IF). After descaling, samples were extracted from the regions with different nozzle footprints and analyzed to quantify descaling efficiency. Analysis and quantification of the surface

quality using the criteria described above showed significant difference in descaling efficiency when the impact factor (*IF*) was varied from low to high. Figure 8 illustrates a typical residual scale condition after descaling with different *IF* and the actual averaged percentage each of the three categories (A, B, and C) of surface quality. The quantified results showed that, the low *IF* condition resulted in complete removal of the external scale (*Fe*-oxides) and partial removal of the internal scale (mixed *Fe-Si* based oxides), accounting for up to 61% clean surface for class A and 39% residual scale (23% class B and 16% C). The residual scale thickness at the first stage measured between 10 – 25 μm and 10 – 15 μm for surface class B and C respectively.

The residual scales were characterized by deep penetrating oxide roots up to about 40 μm into the metal matrix from the oxide/metal boundary as well as complex orientations for these oxide, particularly for that of surface class C. When *IF* was increased to the medium condition, there was a corresponding increasing in the clean surface class A from initial 61% to 76%, which reflected a decrease in the overall residual scale (class B plus C) from 39% to 24%. The residual scale class B reported the highest reduction, from 23% to 6%. The residual scale thickness in class B decreased to 5 – 10 μm while class C measured between 30 – 60 μm . The residual class C scale was characterized as oxides with entrained metal as well as oxide formation beneath the cluster of entrained metal which appeared to be occluded. The original scale analysis reported higher scale thicknesses in the subsurface sections having higher metal entrainment due to their larger size. This resulted in the decreasing class B and some redistribution of residual scale between, classes B and C.

At the highest IF condition, there was no significant effect in total descaling efficiency (class A), while some reversal in different surface classes with residual scale were observed. At high IF , residual scale totaled 30%, having 18% class B and 12% class C respectively. These results once again highlight the non-uniformity in the formed original scale which likely resulted from complex mixed controlled oxidation mechanisms during the reheating process [33- 36]. The residual class C scale was characterized by oxide buried beneath metal that stretched greater than 100 μm in length. Such scale structural formations may impede descaling since the formed oxides may not be in direct contact with the impinging water pressure from the nozzles during descaling. The residual scale thickness measured between 5 – 15 μm for class B and 30 – 45 μm for class C.

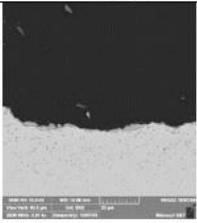
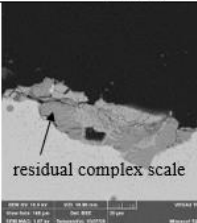
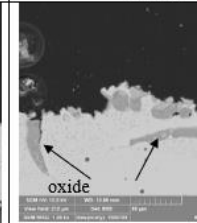
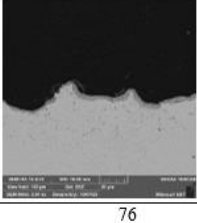
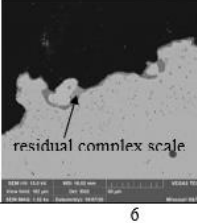
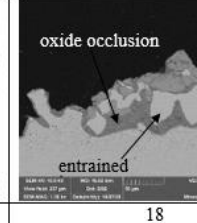
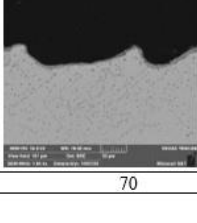
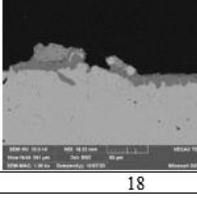
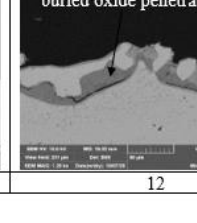
IF	Class A	Class B	Class C
Low			
%	61	23	16
Medium			
%	76	6	18
High			
%	70	18	12

Figure 8. Quantified surface quality of low Cu steel after descaling at different IF .

Interestingly, there were no significant changes in descaling efficiency at the lower applied *IF* in medium *Cu* steel when compared to low *Cu* steel. However, significant effect was observed at high *IF*. In this case, a higher descaling efficiency, above 90% was achieved for the medium and high *IF* (Fig. 9). Specifically, at the low *IF*, only 52% of clean surface quality class A was quantified with 48% residual scale of both class B and C combined. The predominant residual scale was that of class B, accounting for 28% with what appeared to be residuals from the first type of oxide formation in the merged external/complex subsurface layer.

The residual scale measured between 10 – 25 μm for class B and 15 – 30 μm for class C which made up 20% of the total residual. At the medium applied *IF*, there was a significant increase in clean surface class A from initial 52% to 94%, with a rapid decrease in residual scale class B and C. Residual scale observed at the medium *IF* were mostly oxide penetration into the matrix from the interface with curved geometry bending down into the substrate. The measured residual scale exhibited a significant reduction in its thickness (5 – 15 μm). Similar results were achieved at the highest applied *IF* condition: the quantified clean surface class A was near the same as for medium *IF* or about 90%. The residual scale at this conditions was 5% each for both class B and C surface quantifications. Strong evidence of *Cu-enrichment* was observed at this condition. The measured residual scale thickness was similar to that of the medium *IF* condition. The residual scale (class B and C) contained mixed phases of iron oxide, fayalite and iron oxide embedded in fayalite phase.

<i>IF</i>	Class A	Class B	Class C
Low		 iron oxide adherent eutectic fayalite to iron oxide	 adherent eutectic fayalite to substrate
%	52	28	20
Medium		 <i>Cu</i> precipitates residual complex scale	 complex oxide penetration with curved
%	94	1	5
High			 Cu-enrichment adherent fayalite
%	90	5	5

Figure 9. Quantified surface quality of medium *Cu* steel after descaling at different *IF*

In the high *Cu* steel, initial characterization of original scale structure prior to descaling saw a completely different internal scale layer structure, having liquid *Cu*-enrichment at the metal boundaries with complex oxide formation occurring randomly in few spots and sections (Figure 6). The range of original complex subsurface oxide thickness ranged between 20 – 40 μm . At the low *IF* condition, the descaling was highly efficient, with class A accounting for 98% (Figure 10). The residual scale was less than 5%, having a thickness between 1 – 10 μm . The residual scale was observed to penetrate roots at the interface where complex oxides had formed. The clean surface class A showed a strong presence of *Cu*-enrichment at the metal boundary. At the medium *IF* condition, there was no significant change in descaling efficiency quantified, the clean surface class A measured 97%.

The residual scale class B which measured 1% was seen as complex oxide formations at sections with no *Cu*-enrichment (5 – 10 μm) . The residual scale class C which measured 2% was observed as oxide formations in the *Cu*-enriched interface with penetration into the matrix. At the highest *IF*, the descaling efficiency was still above 90%. There was a small increase in residual scale (7%). The residual scale were formations of fayalite phases (class B) at sections of the complex subsurface scale layer with little or no *Cu*-enrichment. These formations were observed as penetrations or superimposed oxides below the substrate interface with complex orientations and classified as class C. Residual scale thickness measured 5 – 10 μm for class B and 5 – 15 μm for class C.

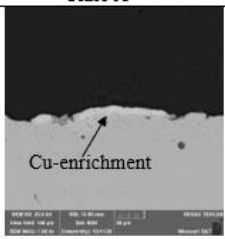
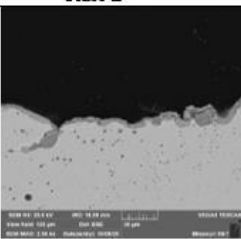
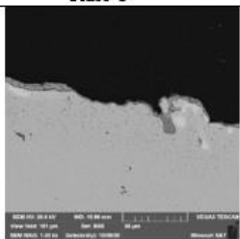
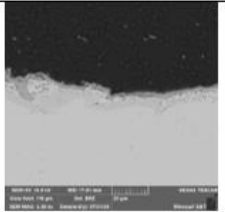
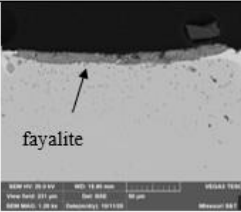
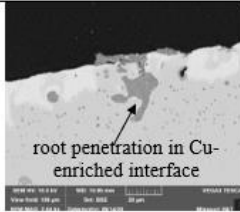
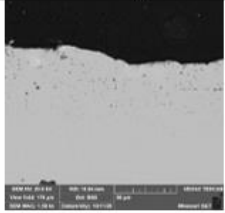
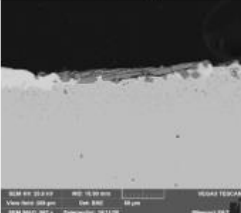
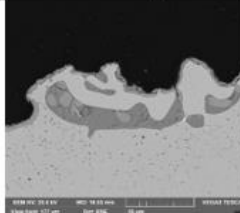
<i>IF</i>	Class A	Class B	Class C
Low	 <p>Cu-enrichment</p>		
%	98	1	1
Medium		 <p>fayalite</p>	 <p>root penetration in Cu-enriched interface</p>
%	97	1	2
High			
%	93	4	3

Figure 10. Quantified surface quality of high *Cu* steel after descaling at different *IF*

3.3. COMPARISON OF DESCALING EFFICIENCY IN THE DIFFERENT CU STEELS

Comparison of descaling efficiency at varying IF in the different Cu steels is shown in Figure 11. It was shown that the effective descaling of low Cu steel requires a higher IF than the maximum that was applied in this study ($2.2 \text{ N/mm}^2 IF$) because only 70% descaling efficiency was achieved. It was observed that the high IF was just enough to remove the external layer and some complex subsurface oxide formations, but a significant amount of the complex oxide remained attached to the matrix after descaling. The probable cause of this result is related to the high level of metal entrainment in the complex scale layers of the low Cu steel. The presence of some entrained metal in the complex subsurface region also served as occluded regions for oxides as they formed within the crevice of metal clusters, which impeded its removal during descaling.

In the case of the medium Cu steel, the critical IF condition was between the medium and high levels ($1.4 - 2.2 \text{ N/mm}^2$) and it was enough to get a removal efficiency of 90% and above. At this Cu level in the steel, differences in the complex subsurface scale layer were observed after reheating, as well as a formation of liquid Cu phase. Cu enrichment in sections of the oxide/metal interface was also predominant in the microstructure. The two types of oxide formations observed could effect on adhesion to the matrix differently. The first type of layered oxide formation contained iron oxide/fayalite/iron oxide which might affect scale removability positively, while the second layered formation (iron oxide/fayalite) might impact scale removability negatively since it has been reported that scale structures having higher levels of fayalite presence at the oxide/metal interface respond poorly to descaling [30]. The Cu enriched liquid layer formed in medium Cu steel at reheating temperature decreased impact energy

and promoted easier descaling at the medium IF . At the same time, from steel surface quality standpoint, deep Cu penetration into the austenite grain boundaries from the oxide/metal interface will lead to liquid embrittlement and cracking during hot rolling deformation [15].

The external/internal/subsurface modification in high Cu steel had dramatic effect on descaling efficiency. The results showed that the complex subsurface scale layer was completely modified at this high Cu level. The scale layer contained fewer complex oxides formation at the oxide/metal interface and was occupied by liquid phase Cu -enrichment which impeded the formation of complex internal oxides as seen in its scale thickness measurements. In the high Cu steel, only a low critical impact factor (IF) was needed to achieve above 90% of scale removal.

In general, it was observed that Cu levels of 0.5 wt.% and above, combined with medium IF conditions (1.4 N/mm^2) improved scale removal efficiency. Overall, the high Cu steel showed higher descaling efficiencies at all applied IF conditions. These results could be related to the decrease in complex subsurface oxide formation which might have been suppressed by liquefaction of Cu at the oxide/metal interface at reheating temperatures above the melting point of Cu ($1200^\circ\text{C} > 1085^\circ\text{C}$). Another possible explanation may be that the Cu phase was still liquid prior to descaling, hence enabling easy separation of the external and internal scale which was dominated by the presence of a Cu -enrichment layer at the matrix interface.

Finally, all observations seen in the scale structure and its effect on descaling of the low carbon steels with different Cu levels are depicted schematically in Figure 12. The phases present in the complex scale structure for each low carbon are identified in

top part of this figure. The schematic depicts the scale structure after reheating and its transformation during descaling at varying impact factors.

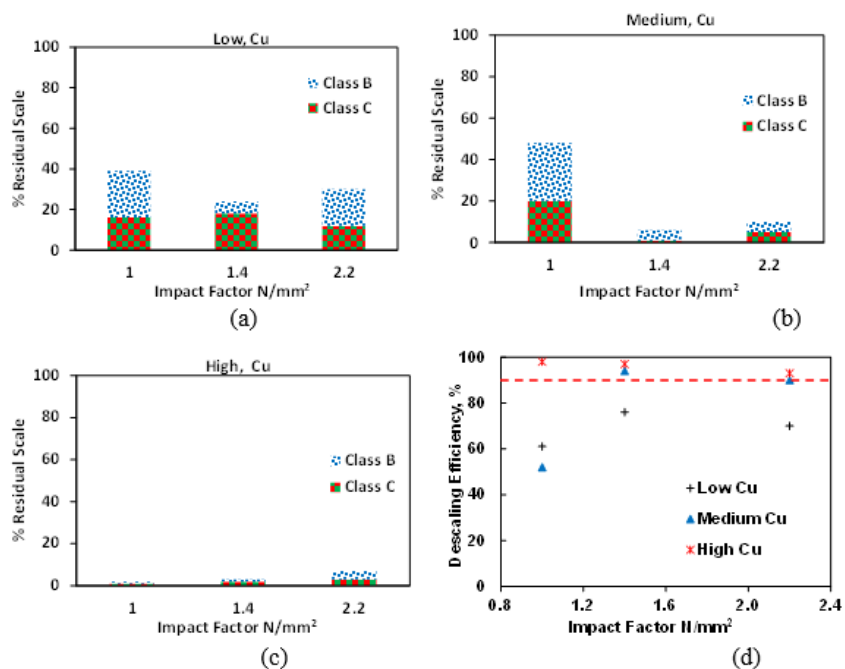


Figure 11. Effect of IF and Cu in steel chemistry on descaling efficiency.

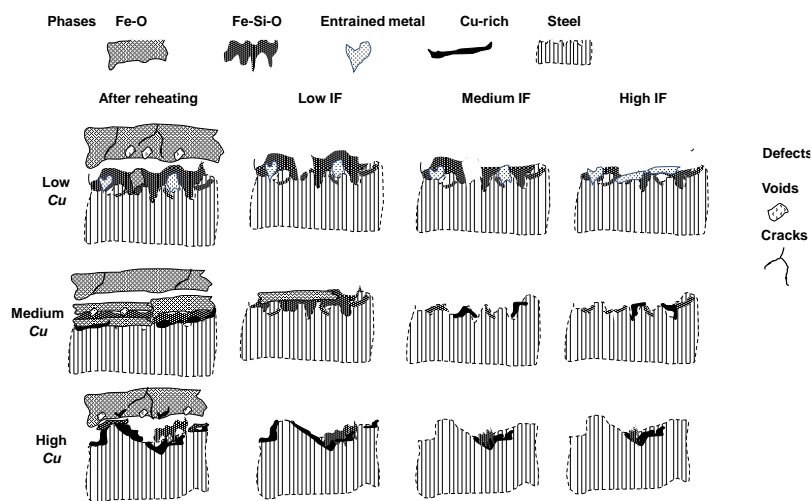


Figure 12. Schematic representation of reheated scale structure of different Cu additions and its structural change during descaling at different impact factors.

4. CONCLUSIONS

The effects of *Cu* additions in low carbon steel on scale formation during reheating and scale removal during descaling was investigated. The investigation was performed on 3 different *Cu* addition levels: low (0.2 wt.%) medium (0.5 wt.%) and high (0.8 wt.%). At these different *Cu* additions, the oxide scale that formed during reheating in an oxidizing combustion gas atmosphere exhibited different structural properties, chemistries, and characteristics in the different scale layers (external and internal/complex subsurface) that formed. Major differences in the internal/complex subsurface scale layers close to the metal substrates were observed, which is critical to scale removal. Low *Cu* levels (0.2 wt.%) exhibited a random distribution of metallic *Fe* entrainment fused into the subsurface oxide structure which increased its complexity and strengthened its adhesion to the substrate. For the medium (0.5% wt.%) and high (0.8 wt.%) *Cu* level steels, the subsurface oxide contained less complexity with high *Cu*-enrichment, particularly the 0.8 wt.% *Cu* steel, which exhibited a restricted complex subsurface development during reheating. The high *Cu* level steels (above 0.2 wt.%) exhibited classic *Cu* penetration into the austenite grain boundaries of the steel from the enriched *Cu* liquid at the oxide/metal interface. This deep penetration appeared to suppress diffusion oxidation kinetics at the metal/oxide interface causing a decrease in subsurface scale growth and development.

The effect of *Cu* additions on the scale structure (subsurface) was evident during scale removal (descaling). The low *Cu* steel exhibited the lowest efficiency 70%, at high impact factor (*IF*) with the residual scale characterized by complex oxides (metallic *Fe*

entrainment and oxide occlusions) that were strongly adherent to the metal substrate after descaling. The medium and high *Cu* steels exhibited improved descaling efficiency (above 90%) with less retained scale due to fewer complexities in the original subsurface oxides after reheating. The critical impact factor for efficient descaling of the low *Cu* addition was higher than the highest *IF* condition applied in this study ($>2.2 \text{ N/mm}^2$), while the medium and high *Cu* additions required between 1.0 to 1.4 N/mm^2 *IF* for efficient descaling. This study demonstrated that increasing *Cu* additions decreased the complexity of the subsurface scale formed in low carbon steels which is critical for efficient descaling.

ACKNOWLEDGEMENTS

This study is supported by Kent Peaslee Steel Manufacturing Research Center, and the authors gratefully acknowledges the support and guidance from the industry advisory committee of Peaslee Steel Manufacturing Research Center.

REFERENCES

- [1] R.J. Fruehan, Overview of Steelmaking Processes and their Development, *The Making, Shaping and Treating of Steel: Steelmaking and Refining volume*, 1998, pp.1-4.
- [2] T. Harada and H. Tanaka, Future Steelmaking Model by Direct Reduction Technologies, *ISIJ International*, Vol. 51. No. 8, 2011, pp. 1301-1307
- [3] M. Xylia, S. Silveira, J. Duerinck, and F. Meinke-Hubeny, Weighing Regional Scrap Availability in Global Pathways for Steel Production Processes, *Energy Efficiency* **11**, 2018, pp. 1135–1159

- [4] J.A.T. Jones, B. Bowman, and P.A. Lefrank: The making, shaping, and treating of steel, *Steelmaking and Refining Volume*, 11th ed., The AISE Steel Foundation, Pittsburgh, PA, 1998, pp. 525–660.
- [5] Energetics Inc.: Energy and Environmental Profile of the U.S. Iron and Steel Industry, DOE/EE-0229, United States Department of Energy, Office of Industrial Technologies, Washington, DC, 2000, pp. 10–26.
- [6] S.C. Marschman, On a Thermodynamic Approach to Material Selection for Service in Aggressive Multi-Component Gaseous and/or Vapor Environments, *Technical Report*, October 2015
- [7] D.A. Melford, The Influence of Residual and Trace Elements on Hot Shortness and High Temperature Embrittlement, *Phil. Trans. R. Soc. Lond.* **295(A)**, 1980, pp. 89-103
- [8] B. Webler, L. Yin, and S. Sridhar, Effects of Small Additions of Copper and Copper + Nickel on the Oxidation Behavior of Iron, *Met Trans B*, Vol. 39B, 2008, pp. 725-737
- [9] E.T. Stephenson, Effect of Recycling on Residuals, Processing, and Properties of Carbon and Low-Alloy Steels, *Metall. Trans. A*, **14A[3]**, 1983, 343-353
- [10] Y.W. Jang, J.H. Hong, and J.G. Kim, Effects of Copper on the Corrosion Properties of Low-Alloy Steel in an Acid-Chloride Environment, *Met. Mater. Int.* **15**, 2009, pp. 623–629
- [11] H.E. Townsend, Effects of Alloying Elements on the Corrosion of Steel in Industrial Atmospheres, *Corrosion*, Vol. 57, No. 6, 2001, pp. 497-501
- [12] Z.B. Jiao, J.H. Luan, Z.W. Zhang, M.K. Miller, W.B. Ma, and C.T. Liu, Synergistic Effects of Cu and Ni on Nanoscale Precipitation and Mechanical Properties of High-Strength Steels, *Acta Materialia*, Vol. 61, Issue 16, 2013, pp. 5996-6005
- [13] S-J. Kim, C.G. Lee, T-H. Lee, and C-S. Oh, Effect of Cu, Cr and Ni on Mechanical Properties of 0.15 wt.% C TRIP-Aided Cold Rolled Steels, *Scripta Materialia*, Vol. 48, Issue 5, 2003, pp. 539-544
- [14] M.I. Copeland, and J.E. Kelley, Reducing Surface Hot Shortness of Copper-bearing Steels, *Bureau of Mines Report of Investigations*, **7682** 1972, pp. 1-19
- [15] A. Nicholson and J.D. Murray, *J. Iron Steel Inst.*, vol. 203, 1965, pp. 1007–1018.

- [16] S. Koji, S. Soek-Jong, K. Masashi, U. Hiroshi, S. Akio, A. Kentaro and C. Nagasaki, Suppression of Surface Hot Shortness due to Cu in Recycled Steels, *Materials Transactions*, Vol. 43, No. 3, 2002, pp. 292-300
- [17] D.A. Melford, The Influence of Residual and Trace Elements on Hot Shortness and High Temperature Embrittlement, *Phil.Trans. R. Soc. Lond.* **295(A)**, 1980 pp. 89-103
- [18] G. Sahoo, M. Deepa, B. Singh and A. Saxena, Hot ductility of Hot-Shortness of Steel Measurement, *Journal of Metals, Materials and Minerals*, Vol. 26, No. 2, 2016, pp. 1-11
- [19] E. E. Glickman and M. Nathan: *J. Appl. Phys.*, **85**, 1999, pp. 3185-3131
- [20] M. G. Nicholas and C. F. Old, Liquid Metal Embrittlement, *J. Mater. Sci.*, **14** 1979 pp. 1-18
- [21] A.J. Hartley, P. Eastburn, and N. Leece, Steelworks Control of Residuals, *Phil. Trans. R. Soc. Lond. A* **295**, 1980 pp. 45-55
- [22] N. Imai, N. Komatsubara, and K. Kunishige, *ISIJ International*, Vol. 37, No. 3, 1997, pp. 217-223
- [23] D.A. Melford: *J. Iron Steel Inst.*, Vol. 200, 1962, pp. 290–99.
- [24] W.J.M. Salter, *J. Iron Steel Inst.*, Vol. 204, 1966, pp. 478–88.
- [25] J. Frick, Optimization of Nozzle Arrangements on Descaling Headers, *4th International Conference on Hydraulic Descaling*, London, U.K., 2003.
- [26] P. Lesli, Effect of Spray Height, Lead Angle and Offset Angle on Impact, *AISTech 2005 Conference Proceedings*, 2005.
- [27] J.W. Frick, More Efficient Hydraulic Descaling Header Designs, *Metallurgical Plant and Technology International*, Vol. 27, No. 2, 2004, pp. 90–92.
- [28] M. Hnizdil and M. Raudensky, Descaling by Pulsating Water Jet, *Metals*, Vol. 5, 2010.
- [29] H. Votavova and M. Pohanka, Study of Water Collision of High-Pressure Flat Jet Nozzles for Hydraulic Descaling, *Applied Mechanics and Materials*, Vol. 821, 2015, pp. 152–158.
- [30] R. Osei, S.N. Lekakh and R.J. O'Malley, P. Lesli, and S. Oldair, Descaling of Medium C and High Si, Mn Steels, *Iron and Steel Technology*, 2021, pp. 48–59.

- [31] T. Asai, T. Soshiroda and M. Miyahara, Influence of Ni Impurity in Steel on the Removability of Primary Scale in Hydraulic Descaling, *ISIJ International*, Vol. 37, No. 3, 1997, pp. 272-277
- [32] RRUFF spectral database, <https://rruff.info/>
- [33] W. Kast, and C.-R. Hohenthanner, *Int. J. Heat Mass Transfer*, Vol. 43. 2000, pp. 807-823
- [34] H. F. Marston, P. H Bolt, G. Leprince, M. Roder, R. Klima, J. Niska and M. Jarl, *Iron and steel making*, Vol. 31, No. 1, 2004, pp. 57-65
- [35] R. Osei, S.N. Lekakh and R.J. O'Malley, Scale Formation on 430 Stainless Steel in a Simulated Slab Combustion Reheat Furnace Atmosphere, *AISTech 2020 Conference Proceedings*, 2020, pp. 1126–1137.
- [36] R. Osei, S. Lekakh, and R. O'Malley, Effect of Al Additions on Scale Structure and Oxidation Kinetics of 430-Ferritic Stainless Steel Reheated in a Combustion Atmosphere, *Met Trans B* **52**, 2021, pp. 3423–3438

VI. EFFECT OF MOLD POWDER RESIDUE ON THIN CAST SLAB SCALE STRUCTURE EVOLUTION DURING REHEATING AND DESCALING

Richard Osei¹, Dmitry Tsvetkov², Tony Bader², Simon Lekakh¹, Ronald O'Malley¹

¹Peaslee Steel Manufacturing Research Center, Department of Materials Science and Engineering, Missouri University of Science and Technology, Rolla, MO, USA, 65409

²Steel Dynamics Flat Roll Group Columbus Division, Columbus, MS, USA, 39701

ABSTRACT

Mold powder is an essential part of the continuous casting process as it provides strand lubrication and controls mold heat transfer. Also, the chemical makeup of mold powder can modify the surface of a cast slab, forming complex scale structures during casting and reheating. Such surface scale modification can potentially affect descaling. In this study, two industrial steel grades samples were collected and characterized to report scale evolution. Industrial descaling practice was simulated in the laboratory. Effects of steel chemistry and surface condition on scale structure and descaling efficiency are discussed. The results prove useful information for improving steel quality.

Keywords: mold powder, descaling, scale structure, reheating, as-cast

1. INTRODUCTION

Mold powder plays a key role in steelmaking. During the continuous casting of steel, mold powder is applied to the surface of the liquid metal during the onset of

solidification. Application of the mold powder forms a slag bed of different layers on the liquid pool, including a sintered, liquid, and solid slag, and finally casting powder or granular layers which provides thermal insulation, prevent oxidation of the molten steel, absorb inclusions, lubricate strand, and regulate heat transfer [1-5]. After continuous casting and final solidification, there is significant amount of residual mold powder residing on the surface of the final cast slab. This residue on the slab can be a complex mixture of slag from mold powder and iron oxide formed during secondary cooling of slabs at high temperatures and in atmosphere containing a mixture of air and water vapor. Evidence of residuals mold powder have been reported on the as-cast surfaces of cast slabs in ferritic steels [6]. The extent and level of mold powder residue on cast slabs may interfere with subsequent processes, such as reheating, descaling, and hot rolling. In extremely severe cases of adhered scale and mold powder residue, cast slabs may need to undergo surface grinding, scarfing, or descaling prior to reheating. These steps can minimize surface imperfections on some cast slab; However, such treatments increase production cost and can reduce product yield.

Studies of slab surface condition prior to reheating have reported significant effects of mold powder residue on oxidation kinetics and scale structure transformation on as-cast slabs [6]. A previous study that characterized the as-cast surface of ferritic stainless steel revealed complex scale structures containing mold powder residue with different layers which promoted significant modification of subsurface scale topology and chemistry during reheating in a combustion gas atmosphere [6]. Another study on surface condition of high strength low alloy steel (HSLA) also showed significant modification of the scale structure, which included voids, cracks, entrapped steel

interlaced with residual mold powder [7]. In general, scale formed on as-cast carbon and ferritic stainless-steel surfaces with residual mold powder have been reported to have a complex subsurface structure [6, 7] when reheated in combustion gas atmosphere, which potentially affect its ease of removal. However, several studies have also suggested that the application of mold powder to type 304 austenitic stainless steels will promote the formation of a less complex subsurface structure due to the restriction of $CrO_2(OH)_2$ vaporization which disrupts the formation of a continuous Cr_2O_3 layer in the subsurface scale region during reheating in a combustion gas atmosphere containing water vapor [9, 10]. Research into efficiency of descaling has shown that the subsurface scale layer is critical for hydraulic scale removal prior to hot rolling [8].

Surface quality of hot roll coils is very critical when products are to be used in the automotive sector and the other applications with intensive welding. Due to the effect of residual mold powder on as-cast scale formation and surface modification during reheating, insight into these thermo-chemical processes for thin cast direct hot rolled slabs and effects on scale removal and product quality would be beneficial to the steel industry. In this article, a set of industrially cast thin steel slabs with different surface conditions were investigated to report the effect that mold powder residue plays on scale formation in a combustion gas atmosphere followed by scale removal using hydraulic descaling.

2. EXPERIMENTAL PROCEDURES

The composition of the thin slab steel used in this study is presented in Table 1. The samples were obtained after continuous casting prior to hot charge reheating. Initial

scale characterization was conducted on the samples to document structure and chemistry of as-cast scale formed during continuous casting. Specimens for the initial scale characterization were machined from the near-surface region of the as-cast slab (30x20x10 mm), with the original as-cast surface. For reheating and descaling studies, samples were carefully machined from the cast slabs, having 165 mm x 110 mm x 20 mm. Prepared samples contained two types of surfaces: as-cast with residual scale and cleaned by pre-machined. Pre-machining included surface milling followed by wet grinding with 60 grit silicon carbide. The surface of the ground sample was measured to have Ra of 0.271 μm using 3D optical profiler (Nanovea, Model PS50 Micro Photonic Inc.). To prevent rusting prior to testing, sample surfaces were preserved by cleaning with ethanol and air drying.

Table 1. Thin slab cast steel used in this work (wt. %).

<i>C</i>	<i>Si</i>	<i>Mn</i>	<i>Cr</i>	<i>Ni</i>	<i>Cu</i>
0.050	0.160	0.420	0.070	0.044	0.110

To simulate industrial scale formation during reheating, the samples were reheated in a 35kw induction melting furnace (Model LSZ-35), having a 200 mm x 130mm x 25 mm induction chamber, which was embedded in an enclosure to control the furnace atmosphere. A detailed description of the reheating methodology was provided in a previous article [8]. The atmosphere of the industrial reheating furnace was simulated by mixing gases in proportions that reproduced the natural gas combustion atmosphere in an industrial furnace (Table 2). An excess oxygen level of 1.5% was chosen for this study based on observed industrial reheat furnace operating conditions. The gas flow rate

supplied to the heating chamber was 6000 ml/min, which provided approximately a 2 cm/sec gas velocity in the reaction zone. Calculations confirmed the absence of gas starvation in the reaction zone at this flowrate. The temperature during reheating was controlled by a K-type thermocouple inserted into the slab. The thermocouple enabled adjustment of the furnace power to control the reheating temperature within $\pm 10^{\circ}\text{C}$. The reheating temperature and time employed for the test was 1060°C for 20 min soaking time after temperature equilibration, which mimicked an industrial hot charge reheating (Figure 1f).

At the end of the oxidation period, the sample was removed with care from the furnace chamber and quickly transported into a descaling chamber to avoid cooling prior to descaling. The hot sample was subjected to hydraulic descaling using high pressure water at a constant 1.4 N/mm^2 impact factor (*IF*), which is representative of descaling practices used by many industrial sites. The descaling was conducted at a spray lead angle of 25° at a flowrate of 4 gpm at 4000 psi. A detailed description of the CNC descaling process has been reported in a previous article [8]. After descaling, the sample was quenched with cold water to prevent the development of secondary scale. The footprints formed during descaling were coated with epoxy to preserve the surface.

After the descaling experiment, a Maxiém CNC waterjet with fine abrasive (Model OMAX 0707) was used to extract rectangular 10 mm x 15 mm x 20 mm samples from footprint zones along the length of the sample. Figure 1 shows the reheating, descaling and sample extraction stages used in this work. A section of the original scale formed during reheating was also extracted from the non-descaled part of the sample for analysis. All extracted samples were cross-sectioned, mounted in epoxy, ground using

silicon carbide abrasive papers to 1200 grit and mechanically polished with 0.1 μm diamond paste, applying a low controlled pressure to prevent scale breakage during sample preparation. The morphology, thickness, microstructure, and chemistry of the original and residual oxide layers were analyzed with a scanning electron microscope (SEM) using a TESCAN-ASCAT system equipped with Bruker energy dispersive spectroscopy (EDX). A quantitative approach was used to evaluate the descaling efficiency by classifying the descaled surface into 3 structure classes and measuring the percentage of each structure on the cross-sectioned samples extracted from the descaled surface. ImageJ software was used as a measuring tool to quantify the 3 different surface classes: A-clean surface, B with internal residual scale and C having complex subsurface scale. Details of the quantification approach and descaled surface classification have been explained in a previous publication [8]. Final descaling efficiency for different surface conditions was compared graphically to report the effect the initial surface condition on scale removability.

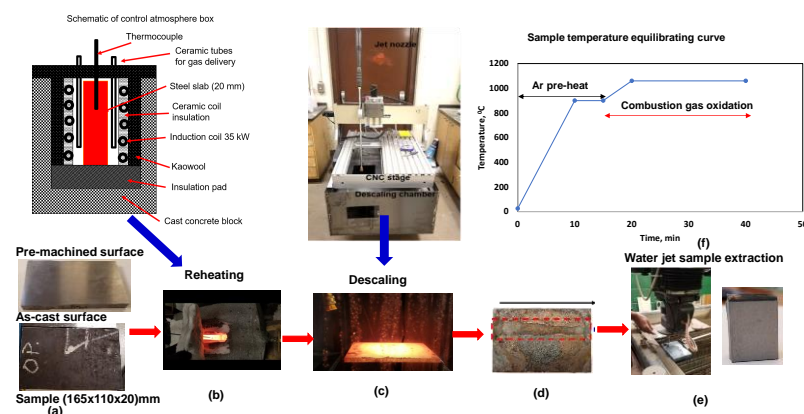


Figure 1. Reheating and descaling setup: (a) sample condition, (b) induction furnace, (c) CNC stage with jet nozzle, (d) footprint of descaled slab, (e) sample from water jet extraction, and (f) hot charge reheating schedule.

Table 2. Industrial reheating conditions simulated in laboratory tests.

Combustion gas, vol. %	Temperature, °C	Soaking time, min
8.9 CO_2 , 17.7 H_2O , 1.5 O_2 , N_2 bal.	1060	20

3. RESULTS

3.1. SCALE FORMED ON AS-CAST SLAB SURFACE

Initial characterization of the as-cast surface condition prior to reheating revealed a complex scale structure (Figure 2). The as-cast surface had: (i) random sections with voids and cracks composed predominantly mold flux residue (middle-left in Figure 2.) and (ii) a zones with a mixed iron oxide/mold powder structure (middle-right in Figure 2). Both scale structure types were well connected to the metal substrate. However, the mixed iron oxide/mold powder layer exhibited less defects (cracks, pores, and voids) in its structure and a smoother scale/matrix interface. The interface for the mold powder residue layer was uneven with some penetration at the interface. The measured thickness of the as-cast scale structure was in a range of 75 – 170 μm . Point EDX chemistry analysis (Table 3) of the as-cast surface structure revealed a strong presence *Ca*-oxide, an indication of mold powder residue (points #1, #2, #3, #4, and #6). The randomly distributed *Na*-residues were also detected.

Chemistry analysis form multiple points identified elements associated with typical mold powder chemistry (*Mg*, *Na* and *Al*). The presence of this complex *Ca-Na*-based oxide chemistry indicated presence of residual mold powder on the as-cast slab surface, which was introduced at the first stage of continuous casting. The mold powder residue (oxide jacket) on the as-cast slab surface was intertwined with iron oxide (point

#3 and #4) formed later during cooling solid slab. Iron oxide (point #5) on the as-cast surface forms due to the presence of air and water vapor that comes into contact with the cast slab during secondary cooling. The thin slab discharge temperature after casting was reported to be $\sim 900^{\circ}\text{C}$ from industry measurement. The presence of the complex mixture of mold powder residual and iron oxide on the as-cast slab surface was evident from the external scale layer through to the internal scale layer. In the region near interface between steel and scale, the scale layer structure had fine grains with a strong connection to the smooth oxide/metal interface. Such strong adhesion at the interface appears to be aided by the presence of *Ca-Si*-based oxide (point #6) in the scale chemistry. EDX mapping (bottom in Figure 2) revealed the distribution of elements in the as-cast surface scale structure.

Table 3. Oxide scale composition(wt.%) of as-cast surface scale formed prior to reheating (points from Figure 2).

Point	<i>Fe</i>	<i>O</i>	<i>Si</i>	<i>Mn</i>	<i>Mg</i>	<i>Na</i>	<i>Al</i>	<i>Ca</i>
1	8.9	26.0	19.0	-	-	2.1	2.0	42.0
2	20.3	38.8	23.9	1.0	0.8	3.1	6.3	5.8
3	53.4	28.0	10.8	1.3	1.0	-	-	5.5
4	66.4	20.3	0.9	0.9	-	-	-	11.6
5	72.3	22.1	0.5	2.9	1.3	-	-	0.9
6	58.0	26.0	8.0	1.0	-	-	1.0	6.0

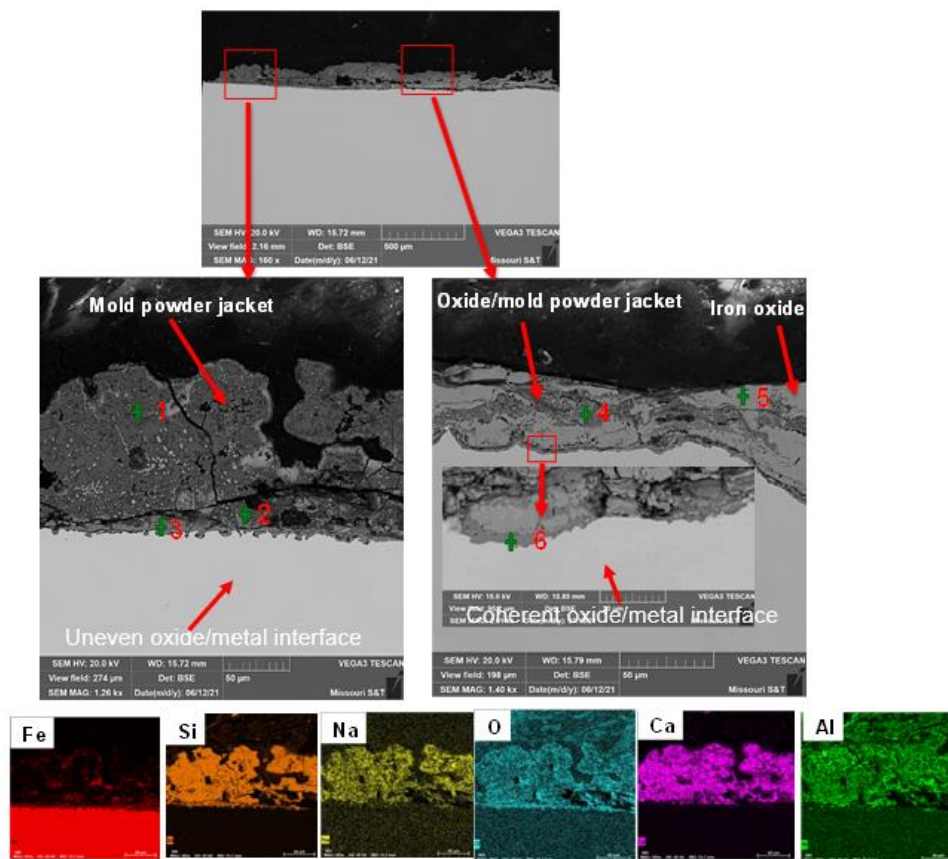


Figure 2. BSE images (top) and EDX elemental maps (bottom) of cross-section of scale structure formed on as-cast surface: top left section with mold powder inclusions, and top right section with mixed oxide/mold powder.

3.2. SCALE AFTER REHEATING

Reheated Pre-machined Surface. Figure 3 shows the cross-sectional microstructure of the scale that formed on the studied low carbon steel grade sample with a pre-machined surface after hot charge reheating in a combustion gas atmosphere. The external scale layer was lost during the reheating process and sample preparation due to extensive spalling. The structure presented in Figure 3 is the internal scale layer. This scale structure was characterized by a dense oxide layer with micro crack defects. It was also partially detached from the subsurface layer that formed directly on the metal

substrate. The thickness of the internal scale layer was measured between $15 - 50\mu\text{m}$. The oxide/metal interface was uneven, and the subsurface layer contained porosity and voids. Some sections on the subsurface appeared to be strongly attached to the metal substrate, while the other sections appeared to be weakly attached due to defect formation at the interface. Some minor metal entrainment was also observed in the subsurface scale layer. EDX chemistry analysis of the oxide scale (Table 4) reported the upper dense part of the internal scale layer to be *iron oxide* with and without traces of *Mn* (points #1 and #2). Just below this layer, a mixed chemistry phase of *iron oxide* and *Si-based oxides* with metal occlusion (point #3 to #6) were present. The *Si-based oxides* were distributed near steel/scale interface, which is typical for a low *Si* grade steel (0.16 wt.%). The elemental EDX map shows the distribution of phases in the internal scale layer (Figure 3).

Reheated As-cast Surface. A cross-section of scale formed after reheating the as-cast surface is shown in Figure 4. The scale structure which initially consisted of a mixture of mold powder residue and iron oxide on the as-cast surface (Figure 2) was significantly transformed. Particularly large changes were visible in the subsurface region. The external scale structure was dense with transverse crack running downward through the structure with some voids in the upper section of the scale layer. The external layer was separated from the internal/subsurface layer but did not spall off and had some connection to the underlying layer. The external scale layer measured between $295 - 330\mu\text{m}$ in thickness. The chemistry (Table 5) of the external scale layer was determined to be iron oxide (point #1). The internal/subsurface scale layer exhibited different structures with complex formation and chemistry (point #2 to #6).

The chemistry consisted of a mixture of *Fe/Si*-based oxide with traces of *Ca*, *Cu*, *Mn*, *P*, and *Zr*. Subsurface structure exhibited different characteristics. Pure *iron oxide* formed on the complex oxide layer. The complex layer showed strong adhesion to the metal substrate with no defects and consisted of *Fe-Si* based oxides. Similar complex mixed phase layer was seen in subsurface structure, with trace of residual *Ca* in the scale chemistry (point #3 and #6). The structure of subsurface layer was porous with voids in the mid-section but showed strong adhesion at the oxide/metal interface. The subsurface scale thickness measured between $30 - 75 \mu\text{m}$. This was much higher than for subsurface reported on the pre-machined sample. The presence of residual mold powder significantly modified formed scale during reheating. The presence of the mold powder residue residing on the slab during continuous casting appears to have promoted scale formation reactions during high temperature reheating, leading to a higher scale growth rate in the subsurface region and strong interface adhesion between the oxide and metal substrate [6, 7]. The subsurface scale structure also exhibited of metal entrapment (*Fe-Ni-Cu*) in the complex oxide mixture, which may reinforce the oxide adhesion to the metal substrate. This intensified grain boundary oxidation is observed when the mold powder contaminated as-cast surface undergoes reheating.

Table 4. Oxide scale formed on pre-machined surface during reheating (wt. %). Points are from Figure 3.

Point	<i>Fe</i>	<i>O</i>	<i>Si</i>	<i>Mn</i>	<i>Ca</i>	<i>Ni</i>	<i>Cu</i>
1	77.4	22.4	0.2	-	-	-	-
2	76.9	22.4	0.1	0.6	-	-	-
3	58.7	29.5	10.8	1.0	-	-	-
4	98.1	0.9	0.2	0.8	-	-	-
5	85.4	0.4	-	-	-	8.6	5.6
6	56.0	29.3	10.7	1.0	-	-	-

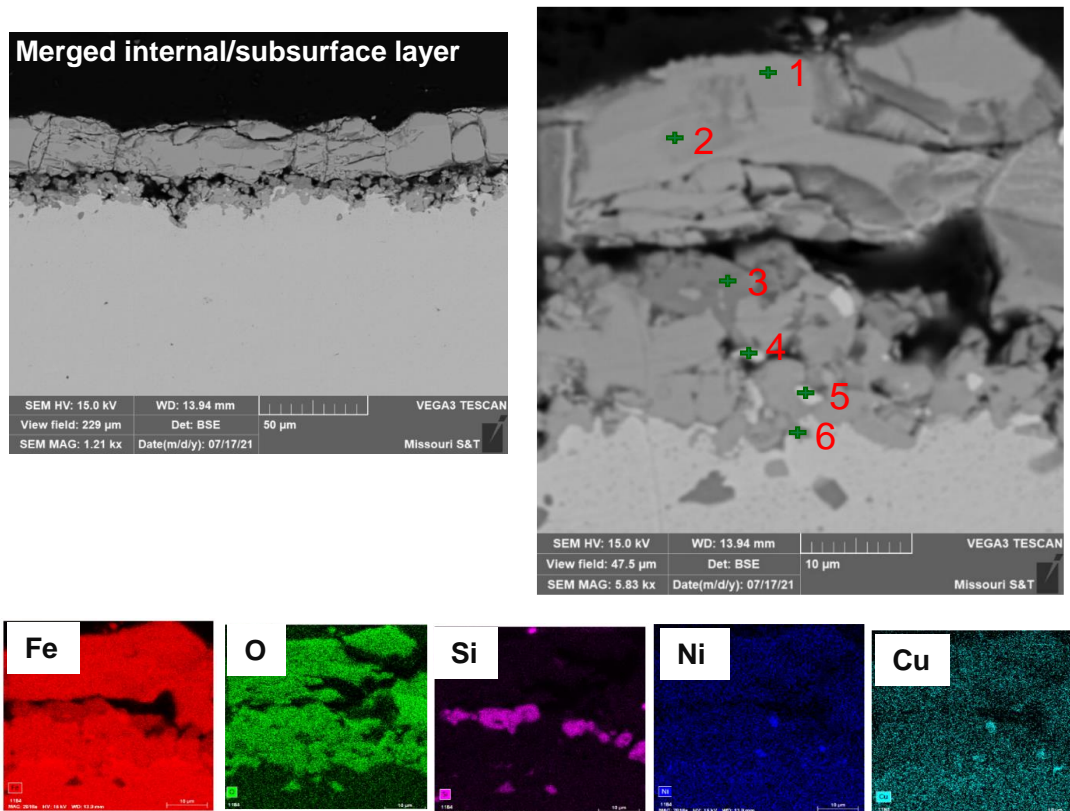


Figure 3. BSE images (top) and EDX elemental maps (bottom) of scale structure formed on pre-machined surface during reheating.

Table 5. Oxide scale composition (wt. %) in reheated steel with as-cast surface. Points are from Figure 4.

Point	<i>Fe</i>	<i>O</i>	<i>Si</i>	<i>Mn</i>	<i>Ca</i>	<i>Cr</i>	<i>Cu</i>	<i>Ni</i>	<i>Zr</i>	<i>P</i>
1	77.7	22.3	-	-	-	-	-	-	-	-
2	77.1	22.4	0.2	-	-	0.3	-	-	-	-
3	61.5	27.0	7.9	1.2	0.6	-	0.8	-	1.0	-
4	80.2	-	-	-	-	-	9.2	10.6	-	-
5	60.3	28.7	9.8	1.2	-	-	-	-	-	-
6	59.6	26.8	8.1	1.7	0.6	-	-	-	-	3.2

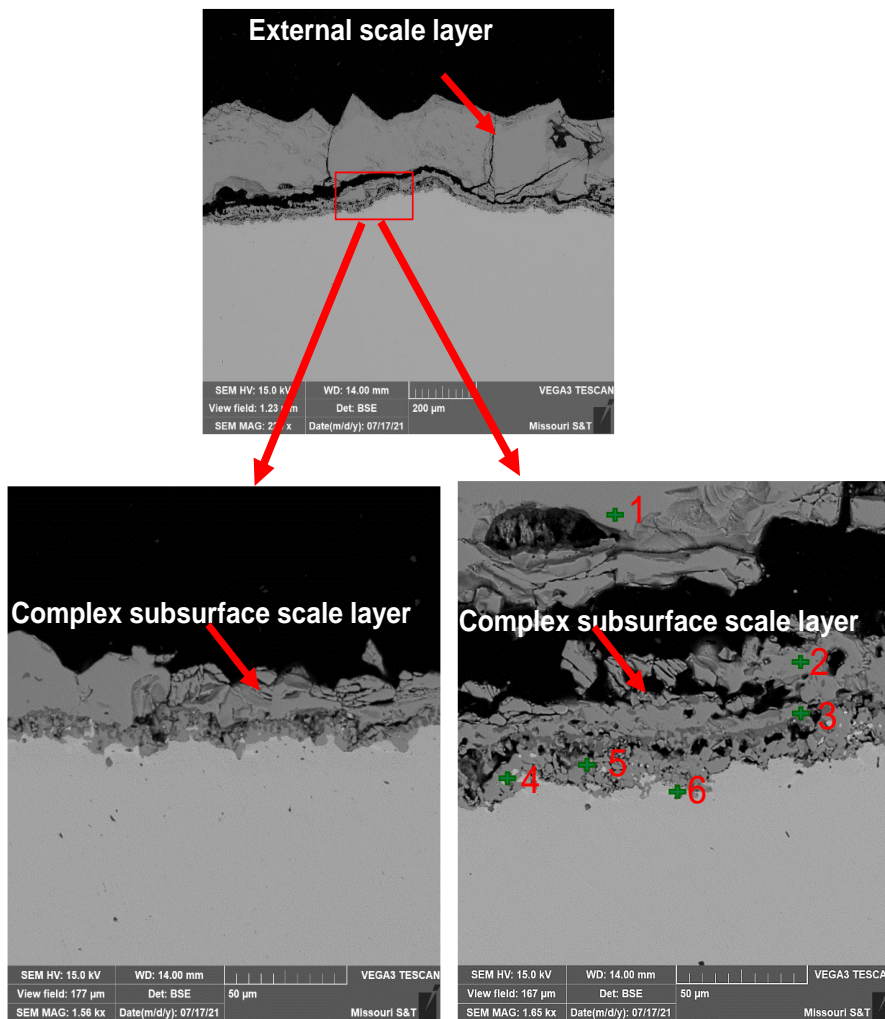


Figure 4. Cross-section BSE of scale structure formed on as-cast surface after reheating: top (low magnification), and bottom (high magnification)

4. DESCALING EFFICIENCY AND DISCUSSION

After reheating, samples were descaled using a CNC controlled stage. Descaled samples were analyzed to report scale removal efficiency (Figure 5). Residual scale was classified into class B and C based on its structure, using the classification method detailed in a previous article [8]. For the case of the pre-machined surface condition, 90%

efficiency (clean surface class A) was achieved at an applied impact factor of 1.4 N/mm^2 . The measured residual scale totaled 10% (8% class B and 2% class C) after descaling. An analysis of the residual scale structures revealed a lower residual scale thickness of between $5 - 10 \mu\text{m}$ and less complex oxide root penetration (class C residue) for the pre-machined surface condition (Figure 6 top-left) that for the as-cast slab condition with mold powder residue.

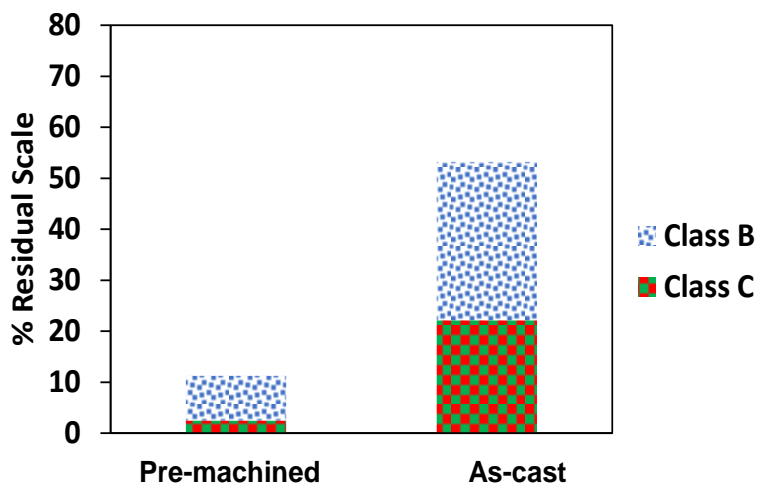


Figure 5. Effect of surface condition on descaling efficiency.

Descaling efficiency for the as-cast surface condition was 47%, with 53% residual scale remaining on the surface at the same impact factor. The residual scale was 5 times thicker than the residual scale on the pre-machined surface. Surface class C residual scale was classified as complex oxide scale formation (*Fe-Si*-based oxide) with intensive root penetration into the subsurface metal matrix. Analysis of residual scale after descaling of the reheated sample with the as-cast surface revealed high levels of complex oxide with deep root penetration and strong adhesion to the substrate (Figure 6 top-right). The

thickness of the residual scale measured between 15 – 30 μm . Higher SEM magnification images of the subsurface residual scale (Class C) revealed a much more complex oxide formation in the subsurface (Figure 6 bottom-left).

Elemental mapping revealed that the complex residual scale structure had *Fe-Si-Ca* oxide mixture. This oxide mixture was mostly adherent to the metal substrate and was woven into the *Fe* oxide phase. This type of structures formed in the subsurface of the reheated slab with the as-cast surface appears to decrease descaling efficiency due to the high adhesion of these complex oxide formations. In previous studies, steels with higher *Si* level (1.7 wt.%) responded poorly to descaling due to similar complex oxide structures found in the subsurface scale region. Current results show that, even at lower *Si* levels (0.16 wt.%) samples with an as-cast surface condition significantly decreased descaling efficiency when *residual mold powder* was present due to the modification of subsurface scale structure. However, this study also showed that cleaning as-cast surface prior to reheating will significantly improve descaling efficiency as observed in the case of the pre-machined surface condition.

Based on the SEM/EDX analysis presented in this study, the effect of mold powder on the evolution of the scale layer on an as-cast slab during reheating and descaling have been depicted schematically in Figure 7. Reheating clean pre-machined surface resulted in the formation of less complex scale structures in the subsurface with low thickness due to short reheating times typical for a hot charged thin slab. The fewer complexities lead to better descaling at an impact factor of 1.4 N/mm^2 . For the as-cast surface condition, mold powder deposited on the slab during continuous casting interacts with the slab to form a residual *Ca-Si-Na* oxide with an uneven interface. This residue is

transformed into a mixture of oxide/mold powder during secondary cooling in the presence of air and water vapor at high temperature (above 900°C). Further reheating of the as-cast surface with oxide/mold powder residue in a combustion gas atmosphere leads to significant transformation of the subsurface layer, characterized by strong adhesion of *Ca-Na-oxides* and root penetration by mixed *Fe-Si-oxides*. Complexities in the subsurface are promoted by flux reactions at the oxide/metal interface at high reheating temperature that promotes faster scale growth kinetics and defect formation. The external scale layer also experiences densification and detachment due to stress generation in the growing oxide layer.

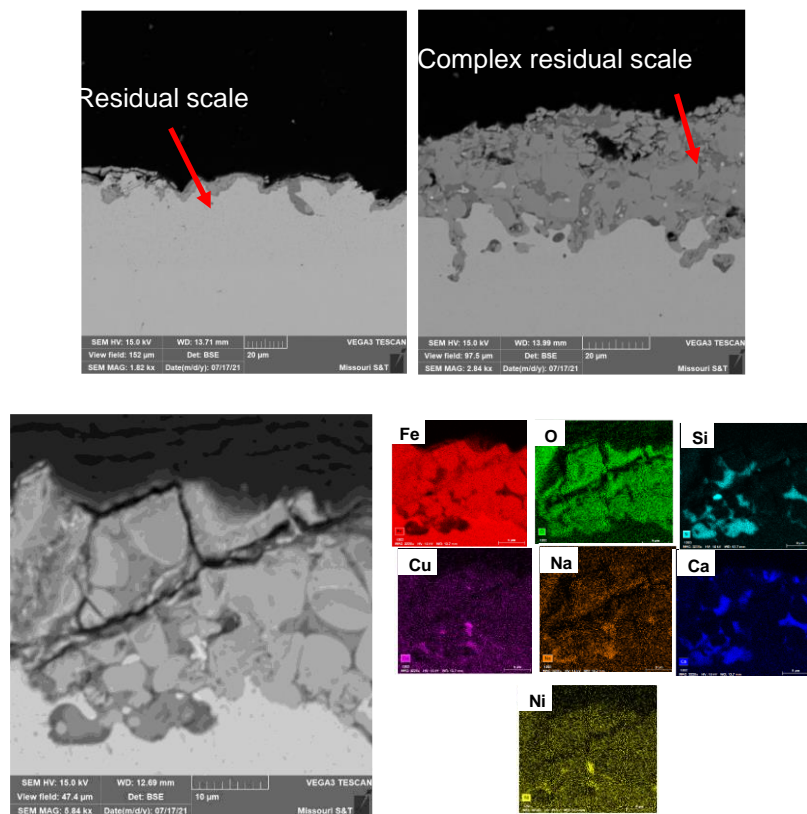


Figure 6. Cross-section BSE of residual scale structure after descaling: top-left (pre-machined surface), top-right (as-cast surface), bottom-left (as-cast surface with, higher magnification), and bottom-right (elemental map for as-cast surface).

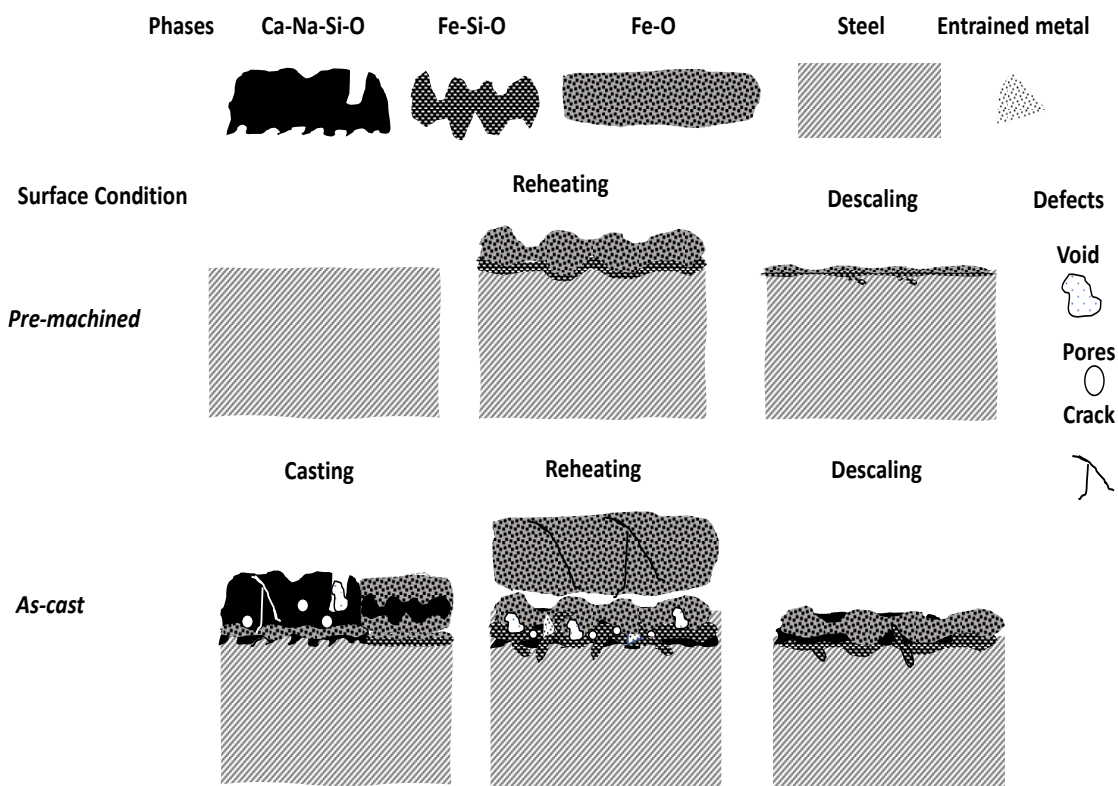


Figure 7. Schematic representation of scale structure evolution from casting to descaling on different surface conditions.

5. CONCLUSIONS

Scale formation during hot charge reheating in a combustion atmosphere followed by descaling was studied for a low carbon steel grade produced by thin slab casting with different surface conditions (as-cast and pre-machined). The impact of surface condition on scale structure evolution during reheating and descaling was investigated. Initial scale characterization of steel with the as-cast surface condition revealed high levels of mold powder residue on the as-cast surface scale structure with complex mixed chemistries of mold powder residues and oxide/mold powder.

Reheating the samples in the as-cast surface condition promoted the formation of complex scale structures, particularly in the subsurface region of the scale layer, which was observed to be strongly modified by the presence of mold powder residue when compared to pre-machined samples.

The complexity of scale formed on the as-cast surface containing mold powder residue was observed to decrease descaling efficiency. The pre-machined surface condition exhibited a higher descaling efficiency (90%) at a hydraulic descaler impact factor condition of 1.4 N/mm². The as-cast surface condition exhibited a lower descaling efficiency of 47% with 53% residual scale at the same descaling impact factor. The descaling efficiency quantification indicated that surface condition prior to slab reheating significantly influences scale removability. For the case of as-cast surface condition with mold powder residue, the subsurface scale layer was modified and transformed by presence of complex mold flux residues containing oxides of *Si*, *Ca*, *Na*, *Mg* and *Al* which appears to accelerate oxidation reactions during reheating to facilitate complex oxide formation with properties and characteristics that impede scale removability.

The studies suggest that cleaning as-cast surfaces prior to reheating is critical in improving descaling efficiency and overall product quality in thin slab casting. The result also gives insight into the effect of mold powder residue on cast slab surface modification and its impact on descaling efficiency and seeks to inform flux optimization studies to take into consideration the aggressiveness of mold powder on the slab surface during reheating.

ACKNOWLEDGEMENTS

This study is supported by Kent Peaslee Steel Manufacturing Research Center, and the authors gratefully acknowledges the support and guidance from the industry advisory committee of Peaslee Steel Manufacturing Research Center.

REFERENCES

- [1] Y. Sugitani, M. Nakamura and T. Watanabe: *Tetsu-to-Hagan*, 67 (1981), 1508.
- [2] K.C. Mills, A.B. Fox, Z. Li, and R.P. Thackray: *Ironmak. Steelmak.*, 2005, vol. 32 (1), pp. 26–34.
- [3] K.C. Mills and A.B. Fox: *ISIJ Int.*, 2003, vol. 43, pp. 1479–86.
- [4] W. Wang and A. Cramb: *ISIJ Int.*, 2005, vol. 45, pp. 1864–70.
- [5] H. Nakada, H. Fukuyama, and K. Nagata: *ISIJ Int.*, 2006, vol. 46, pp. 1660–67.
- [6] R. Osei, S. N. Lekakh, and R. J. O’Malley: *AISTech Proceedings*, 2020, pp. 1126-1137
- [7] R.M.P. Huitron, P.E.R. Lopez, E. Vuorinen, P.N. Jalali, L. Pelcastre, and M. Karkkainen: *Metals*, 2020, 10, 1243, 22 pp.
- [8] R. Osei, S.N. Lekakh and R.J. O’Malley, P. Lesli, and S. Oldair: *Iron and Steel Technology*, 2021, pp. 48–59
- [9] N.M. Jean-Jacques: *Masters Thesis*, 2008, University of Pretoria, South Africa, 106 pp.
- [10] K.H. Cheung: *Ph.D. Thesis*, 2012, Carnegie Mellon University, USA, 197 pp.

SECTION

2. CONCLUSIONS AND RECOMMENDATIONS

2.1. CONCLUSIONS

Scale formation, properties and descaling in steelmaking were intensively investigated and reported in this dissertation. The scale formation studies used different characterization techniques (Raman spectroscopy, SEM, optical profiling and TEM) to provide indepth analysis of formed scale structure. The effect of steel chemistry and atmospheric conditions on scale formation in different industrial steel grades were established when simulated in actual industrial combustion gas atmosphere. The studies established that major alloying elements (*Mn*, *Si*) and impurities (*Cu*) present in steel modifies the properties of formed scale particularly in the subsurface layer scale region.

Specific distinction of scale structures formed different steels reported low and medium carbon steels with low residuals to be characterized by layered iron oxide structures in the external and internal layers with significant detachment, and mixed phases of complex oxides (fayalite and iron oxide) in the subsurface scale layer region with high level of porosities, unevenness, and gaps formations. The advanced high strength steels (AHSS) were characterized by coherent external/internal scale layer and complex subsurface with strong adhesion in the subsurface. Stainless steel grades were characterized by mixed oxide phases in the external, internal, and subsurface scale layer with root penetrations weaving into the metal substrate for ferritic steels

and superimposed oxides on the metal matrix for austenitic steels.

Complex kinetics associated with scale formation in combustion gas atmosphere was modelled and the mechanism responsible was revealed for a ferritic stainless-steel in this study. The kinetic mechanisms and modelling of scale formation on the ferritic stainless-steel grade revealed how micro alloying elements in steel chemistry (*Al*) changed scale formation kinetics in the subsurface when high resolution characterization TEM was employed. The mechanism revealed that doping of amorphous silica core located in the subsurface scale layer region by *Al* decreased oxygen permeability and inhibited interstitial and network diffusion of oxygen, leading to a deceleration in growth kinetics for the *Al* micro alloyed ferritic steel.

This study has demonstrated the potential of using a thermodynamic simulation methodology under local equilibrium conditions to predict multi-phase oxide scale composition in alloy steels to provide reasonable guidance for subsequent technological processes such as descaling and hot rolling. This approach was verified in this study to have a good agreement between thermodynamically simulated phases and experimentally verified oxide phases.

For the first time, a comprehensive study has been performed on descaling technology with precise variation in impact factor (*IF*) using a special designed CNC stage nozzle displacement apparatus. The CNC descaling approach made it possible to conduct scale removal practices with minimum error and was used to simulate actual hot charge industrial scale removal practice in different steel grades. A quantification technique was adopted to assess scale removal efficiency. The quantification technique gave critical insight into how different types of scale structures in different steels grades

affected descaling efficiency. The descaling tests showed that structure of internal scale layers and deep subsurface scale structure with penetrations into the metal matrix are the most important factors affecting scale removability. Steel grades with high *Mn* and *Si* levels responded poorly to descaling even at higher impact factor (*IF*) applications due to complex subsurface structure formation during reheating. The effect of impurity (*Cu*) in steel grade on scale formation and its removal was analyzed. Steel grades with high *Cu* additions responded positively to descaling with higher efficiency even at low impact factor applications comparatively to low *Cu* steels. It was established that high *Cu* steels restricted the formation of complex subsurface oxide layer during scale formation and promoted easy scale removal. Hydraulic parameters were manipulated to improve descaling efficiency in different steel grades and the optimization techniques that improved descaling efficiency were established.

The major impact of industrial slab with as-cast surface condition on scale formation and descaling was determined. The studies revealed that residual mold powder from slab continuous casting significantly transformed subsurface scale layer properties during reheating and restricted easy scale removal by hydraulic descaling. The studies recommended cleaning as-cast slab surfaces prior to slab reheating to improve descaling efficiency. The studies gave insight into the effect of mold powder residue on scale formation during slab reheating and its removal. The knowledge from the slab surface conditions seeks to inform flux optimization studies to take into consideration the aggressiveness of mold powder on slab surfaces during reheating.

Finally, laboratory conducted investigations had direct implementation in the industry. Scale formations and removal studies were comparable to actual industrial

results and practices. Results from the scale formation studies has added new knowledge on how different industrial steels grades and their surface conditions affect scale formation and removal practices in complex atmospheres. Optimized descaling improvement parameters saw significant applications industrially.

2.2. RECOMMENDATIONS

In the current study, scale formation in combustion gas atmosphere in different steel grades were characterized and reported to have significant defect formations in the external and internal scale layers. Formation of defects influence scale formation mechanism particularly at high temperatures. Mixed control kinetic model for scale formation in this study did not incorporate the effect of defect on scale formation kinetics modelling. Future research can focus on developing a kinetic model that considers defects formation during reheating. Such a model will help explain complexities of reheating at higher temperatures and the impact of formed scale on its removal.

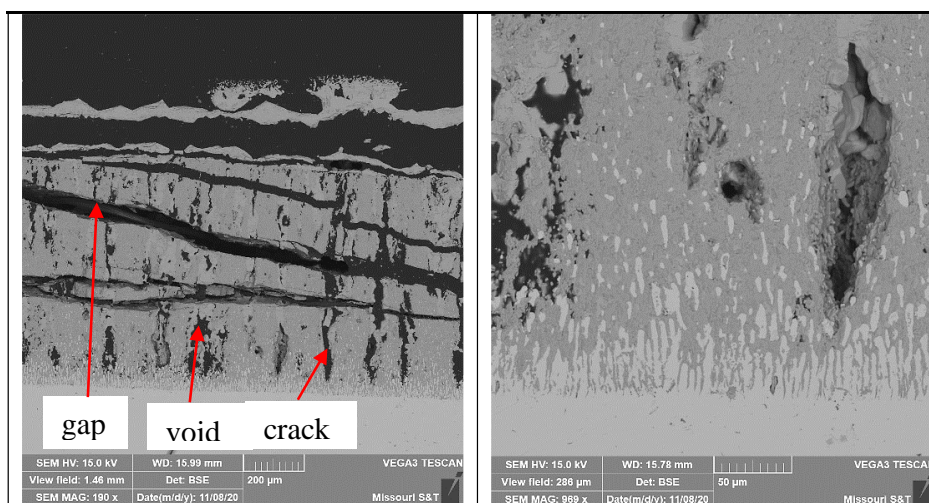


Figure 2.1. Defect formation during high temperature reheating

This study involved high temperature reheating (1200⁰C). At such high temperatures, the metal matrix may undergo phase transformation. The present study did not investigate into the effect of grain size and phase transformation of steel matrix during reheating of oxidation kinetics and mechanism. Future work could investigate into how in the underlying steel matrix beneath the subsurface scale layer affects oxidation kinetics.

Future scale formation and descaling studies could focus on detailed studies of as-cast surface conditions containing mold powder on scale formation and removal, investigate the kinetics and mechanisms associated with as-cast surface with mold powder in different combustion gas atmosphere, interaction of as-cast surface with different steel chemistries and how different mold powder compositions affects the as-cast surface scale structure development particularly the subsurface scale layer region.

BIBLIOGRAPHY

- [1] J.S. Sheasby, W.E. Boggs and E.T. Turkdogan: *Met. Sci.*, 1984 Vol. 18, pp. 127-136.
- [2,] W. Sun: *PhD thesis*, 2005, School of Mechanical, Materials and Mechatronic Engineering, University of Wollongong.
- [3] O. A. Zambrano, J.J. Coronado, and S. A. Rodriguez: *Surface and coating technology*, 2015, Vol. 282, pp. 155-162.
- [4] V. Lee, B. Gleeson, and D. Young: *Oxidation of Metals*, 2005, Vol. 63, pp.15–31.
- [5] R. Chen and W. Yeun: *Oxidation of Metals*, 2003, Vol. 59, pp. 433–468
- [6] R. Y. Chen. and W. Y. D Yuen: *Oxidation of Metals*, 2010, Vol. 73, pp. 353-373.
- [7] R. Y. Chen. and W. Y. D Yuen: *Oxidation of Metals*, 2010, Vol. 59, No.5/6, pp. 433-468.
- [8] H.T. Abuluwefa, R.I.L. Guthrie and F. Ajersch: *Oxidation of Metals*, 1996, Vol. 46, pp. 423-440.
- [9] W. E. Boggs: *Metallurgical society of AIME*, 1973, pp. 84-128.
- [10] H.T. Abuluwefa, R.I.L Guthrie and F Ajersch: *Met Trans A*, 1997, Vol. 28A, pp. 1633-1641
- [11] M.P. Brady, Y. Yamamoto, M. L. Santella and B.A. Pint: *Scripta Materialia*, 2007, Vol. 57, pp. 1117-1120.
- [12] J. C. Bavay and P. Bourgain: *Materials Science and Engineering*, 1987, Vol, 87, pp. 137-143.
- [13] E. W. Grandmaison, H. A Becker, W. R. C. Ormerod, A. Pollard and A. Sobiesiak: *Canadian Journal of Chemical Engineering*, 1997, Vol. 75, pp. 402–413.
- [14]. N. Thanasak, N. K Nisachon and Y Sirilak: *Materials Today*, 2018, Proceedings 5, pp. 9359-9367
- [15] S. R. W. Shatynski and Sherwood: *Surface Technology*, 1984, Vol 21, pp. 39-51.

- [16] N. Moore et al: Technical steel research, EUR 13961, European Commission, 1990
- [17] H. Okada: Nippon Steel Technical Report, UDS 621.771.23
- [18] V.V. Basabe and J.A. Szpunar: ISIJ International, 2004, Vol. 33, No. 9, pp. 1554-1559
- [19] R. Sohn, J-S. Kim, and S. Sridhar: ISIJ International, 2015, Vol. 55, No. 9, pp. 2008-2017
- [20] H. Asteman, J.-E Svensson and L.-G Johansson: Oxidation of Metals, 2002, Vol. 57, No. 3-4, pp. 193-216
- [21] D.J. Young, J. Zurek, L. Singheiser, and W.J. Quadackers: Corrosion Science, 2011, Vol. 53, Issue 6, pp. 2131-2141
- [22] E. Esuman, G.H. Meier, J. Zurek, M. Hansel, L. Singheiser and W. J. Quadackers, Scripta Materialia, Vol. 57, pp. 845-848
- [23] A. Laukka, E-P. Heikkinen and T. Fabritius, Steel Research Int., 2018, 11p.
- [24] N. Otsuka, Y. Nishiyama and T. Kudo, Oxidation of Metals, 2004, Vol. 62, No. 1-2, pp. 121-139
- [25] W.J. Quadackers, P.J. Ennis, J. Zurek, and M. Michalik: Materials at High Temperature, 2005, Vol. 22, Issue 1-2, pp. 47-60
- [26] G.H. Meier, K. Jung, N. Mu, et al: Oxide Met., 2012, Vol. 74, pp. 319-340
- [27] K. Kaya, S. Hayashi, and S. Ukai: ISIJ International, 2014, Vol. 54, No. 6, pp. 1379-1385
- [28] M. P. Brady, Y. Yamamoto, Z.P. Lu, C.T. Liu, P.J. Maziasz and B.A. Pint: United States Patent Disclosure, 2007, 12 pp.
- [29] R.K. Wild: *Corrosion Science*, 1977, Vol. 17, Issue 2, pp. 87-104
- [30] P. Jussila, K. Lahtonen, M. Lampimaki, M. Hirsimaki, and M. Valden: Surf. Interface Anal., 2008, Vol. 40, pp. 1149-1156
- [31] X. Xu, X. Zhang, X. Sun, and Z.P. Lu: Corrosion Science, 2012, Vol. 65, pp. 317-321

- [32] V.B. Trindade, U. Krupp, B.Z. Hanjari, S. Yang and H-J. Christ: *Materials Research*, 2005, Vol. 8, No. 4, pp. 371-375
- [33] Y. Zhang, A. Shi, P. Liang, J. Meng, H. Zhang, C. Zhang, Z. Zhang, and P. Han: *Steel Research Int.*, 2018, Vol. 89, 7 pp.
- [34] X. Cheng, Z. Jiang, D. Wei, J. Zhao, B.J. Monaghan, R.J. Longtottom and L. Jiang: *Surface and Coatings Technology*, 2014, Vol. 258, pp. 257-267
- [35] H. F. Marston, P. H Bolt, G. Leprince, M. Roder, R. Klima, J. Niska and M. Jarl: *Iron and steel making*, 2004, Vol. 31, No. 1, pp. 57-65
- [36]. P.C. Pistorius, N.-A. Quagraine, and C. Coetzee: *The Journal of The South African Institute of Mining and Metallurgy*, 2003, pp. 607-615
- [37] V.H.J. Lee, B. Gleeson, and D.J. Young: *Oxidation of Metals*, 2005, Vol. 63, pp. 15-31
- [38] H. T. Abuluwefa: *Lecture Notes in Engineering and Computer Science*, 2012, Vol. 2196, pp. 1664-1668.
- [39] W. W. Smeltzer: *Acta Metallurgica*, 1960, Vo. 8, pp. 377-383.
- [40] C. Xu and W. Gao: *Material Research Innovations*, 2000, Vol. 3, pp. 231-253
- [41] H. E. Evans, A. T. Donaldson, and T. C. Gilmour: *Oxid Met*, 1999, Vol. 52, No. 516, pp. 379-402
- [42] H. Asteman, J.-E. Svensson, L.-G. Johansson and M. Norell: *Oxide Met*, 1999, Vol. 52, No. ½, pp. 95-111
- [43] W. Kast, and C.-R. Hohenthanner: *Int. J. Heat Mass Transfer*, 2000, Vol. 43. Pp. 807-823
- [44] Y. Yu and J.G. Lenard: *Journal of Materials Processing Technology*, 2002, Vol. 121, pp. 60-68
- [45] D.B Wei, J.X. Haung, A.W. Zhang, Z.Y. Jiang, A.K. Tieu, X. Shi, and S.H. Jiao: *Wear*, 2011, Vol. 271, pp. 2417-2425
- [46] M. Hnizdil, and M. Raudensky: *Metals*, 2010, Vol. 5, 6 pp.

- [47] S. Lechwar, L. Rauch and M. Pietrzyk: *Steel Research Int.*, 2015, Vol. 86, No. 3, pp. 266-277
- [48] J. Frick: 4th International Conference on Hydraulic Descaling, 2003, London UK
- [49] R. Lesli: AISTech, 2005, The Iron and Steel Technology Conference and Exposition, Charlotte, NC, May, 8 pp.
- [50] J.W. Frick: *Metallurgical Plant and Technology International*, 2004, Vol. 27, No. t 2, pp. 90-92
- [51] H. Votavova, and M. Pohanka: *Applied Mechanics and Materials*, 2015, Vol. 821, pp. 152-158
- [52] P. Kotrbacek, J. Horsky, M. Raudensky and M. Pohanka; *Suppl. Metal Forming*, 2004, pp. 367-370
- [53] T. Asai, T. Soshiroda and M. Miyahara: *ISIJ International*, 1997, Vol. 37, No. 3, pp. 272-277

VITA

Richard Osei was born in Bibiani, in the Western Region of Ghana. He received his bachelor's degree in Minerals Engineering from the University of Mine and Technology Tarkwa, Ghana in the year 2015. After his graduation, he worked as a teaching and research assistant with the Minerals Engineering Department of the University of Mines and Technology for 1 year. He later served as a plant manager for Process Innovation Gold Recovery Processing Plant for a period of 2 years.

In August 2018, Richard started his doctoral study at Missouri University of Science and Technology, Rolla, USA. He joined the research team of Dr. Roald O'Malley in the Peaslee Steel Manufacturing Research Center (PSMRC). He performed research on scale formation, properties and descaling in steelmaking. He presented his work at 3 conferences held by AISTech. In May of 2022 he received his Ph.D. in Materials Science and Engineering from Missouri University of Science and Technology.

Richard was a member of the Materials Advantage, Society of Mining, Metallurgy and Exploration, and the African Students Association at Missouri S&T